BETA-DECAY SPECTROSCOPY OF NEUTRON RICH ISOTOPES USING A PLANAR GERMANIUM DOUBLE-SIDED STRIP DETECTOR

By

Nicole Larson

A DISSERTATION

Submitted
to Michigan State University
in partial fulfillment of the requirements
for the degree of

Chemistry – Doctor of Philosophy

2016

ABSTRACT

BETA-DECAY SPECTROSCOPY OF NEUTRON RICH ISOTOPES USING A PLANAR GERMANIUM DOUBLE-SIDED STRIP DETECTOR

By

Nicole Larson

One important overarching goal in nuclear science is the experimental investigation of nuclear structure. Understanding how the structure of the nucleus evolves as more neutrons (N) and protons (Z) are added is vital to probing the mechanisms that drive the evolution of shell structure. One tool to investigate the migration of energy levels along isotopic chains is through the characterization of isomeric states. Isomeric states can signal a transition between very different nuclear configurations and therefore can be an important test of the evolution of nuclear structure.

β-decay spectroscopy is used to provide a wealth of information on exotic isotopes including half-lives, branching ratios, and energy levels. The selectivity provided by decay spectroscopy places constraints on the spins and parities of nuclear levels. Recently a new planar Germanium Double-Sided Strip detector (GeDSSD) has been used in decay spectroscopy experiments at the National Superconducting Cyclotron Laboratory (NSCL). Exotic ions are produced, delivered to, and stopped within the GeDSSD, where the β-decay electrons, conversion electrons and γ rays are detected. In the present work, the electron and γ ray detection efficiencies of the GeDSSD were determined with source measurements and the performance of the GeDSSD with radioactive ions was characterized in multiple experiments and included β-decay correlation efficiencies, β-gamma summing corrections, and charge state separation through Total Kinetic Energy (TKE) measurements.

Following the development of the GeDSSD, it was applied here to the A$\sim$110 region to explore low-energy isomeric states. Nuclei in this region have had indications of changing nuclear shapes as a function of nucleon number for many years, and much theoretical work has been done in an attempt to explain the existing experimental data. The theoretical calculations predict a changes in structure as a function of nucleon number, and data is needed to clarify the understanding of

the region. The search for isomeric states is one method by which the nuclear structure of the region can be clarified. Measuring conversion coefficients of nuclear transitions can constrain the multipolarity of the isomeric transition, which in turn can constrain the spins and parities of the initial and final states. In order to address this need for data, a recent NSCL β-decay experiment focused on several A$\sim$110 nuclei with Z ranging from 41 to 46 and the results are presented here.

In particular, this work discusses an isomeric state in ^{115}Ru at 123.8 keV, which was previously placed at an unknown energy. This isomeric state is one of several isomers in the Ru and Pd isotopic chains, likely arising from the $h_{11/2}$ orbital. Additionally, several short-lived (less than 20 μs) isomeric states in ^{118}Ag, ^{107}Mo, and ^{109}Mo are discussed.

ACKNOWLEDGEMENTS

There are many individuals who have supported me while I have worked on my PhD. First, I would like to thank my adviser, Sean Liddick, for all his help and support. I would also like the thank the members of my committee, Dave Morrissey, Paul Mantica, and Hendrick Schatz, for their help. Additionally, I should thank the members of my group, all of whom have helped and supported me. Scott, you were always a big help, and I appreciate all you've done for me. Chris, your technical know-how was always a help. The two of you will always be what I think of as the "original" β group. I owe a big thanks to our postdoc Ben, who I think has been of great help to everyone in our group. And to the "new" β group members who have started working on the new direction of the group with the β-Oslo method, Becky and Katie, while we weren't working on the same topics, thank you for your moral support and your friendship.

There were many people at the lab who helped with making my thesis experiment run smoothly. Thank you to all the operators who made sure we had beam and to the A1900 group, in particular Tom Ginter, for their help with selecting the ions for us to study. Another large thank you goes to all of the people who helped with the setup and who sat shift. If there's anyone I forgot, I apologize profusely.

Finally, there are several other people who have supported me while I was in school. My family was always supportive. I made many great friends during grad school, without whom I couldn't have made it through. Aimee-thanks for being a great roommate for my first few years here, and then a great neighbor! It won't be the same without my weekly murder mystery fix with you and Bill. Thanks to Steve, Scott, Luke, Jayda, and Zach for being there from the beginning. It certainly helped to meet such great people so quickly. Thank you, Sasha, for our lunch dates and venting sessions about Chemistry grad school! It seems appropriate that we both started at the same time, and then defended within days of each other. Thank you Jenna, Ragnar, and Titus for always organizing fun events like happy hour, the progressive, and dance parties! Finally, thank you to Andrew, for becoming such a large part of my life in the last few months. You've been a great

source of support (and a great distraction when I needed it from thesis stuff). There are so many other people who have been a positive presence in my life during grad school, and while I don't have space to list everyone by name, I want to thank each and every one of you for your support.

TABLE OF CONTENTS

LIST OF TABLES

LIST OF FIGURES

CHAPTER 1

INTRODUCTION

1.1 Nuclear structure and isomer spectroscopy

The study of nuclear structure seeks to describe the most fundamental properties of nuclei. In a quantum mechanical picture, protons (Z) and neutrons (N) fill particular energy levels; the relative energies of these orbitals vary across the nuclear chart. Of particular interest is observing how an energy level of a given spin and parity shifts in energy as more protons or neutrons are added to the nucleus. The progression of energy levels with specific spins and parities can inform the understanding of how the structure of the nucleus evolves, how nucleons fill nuclear shells, and how nuclear orbitals shift as the nucleus changes with changes in neutron and proton numbers.

Excited states with a metastable, or long-lived, half-life are referred to as isomeric states (denoted as $^{Am}Z_N$). The half-lives of isomeric states spread a wide range, nanoseconds [1] to many thousands of years [2]. An excited state's transition can become delayed, and thus isomeric, if the two states have very different spins or different underlying nuclear structure [1, 2]. Therefore, the discovery and quantification of isomers is important for the study of nuclear structure. In particular, the study of isomeric states is important for investigating the spins and parities of nuclear states because the properties of isomeric transitions, such as the transition's multipolarity, can place constraints on the configuration of that state.

Isomeric states can decay in a variety of different ways. Some isomers decay via β decay [3,4], while others undergo internal transitions [3, 5]. Internal transitions may result in the emission of γ rays and conversion electrons. The relative intensities between the conversion electrons and γ rays place constraints on the change in spins and parities between the initial and final states. Therefore, spectroscopy of γ rays and conversion electrons is a powerful tool for exploring nuclear structure.

1.1.1 β-decay spectroscopy

One experimental probe that can be used to study isomeric states is β-decay spectroscopy. β decay can populate multiple excited states in the daughter nucleus, and γ-ray decay from those states can populate additional states. A recent β-decay experiment at the National Superconducting Cyclotron Laboratory (NSCL) is presented in this work and focuses on the neutron rich A$\sim$110 region of the nuclear chart.

1.1.2 Technique introduction

Recently, a Ge Double-Sided Strip Detector (GeDSSD) [6] was commissioned. While traditional DSSD's are made of Si, the use of Ge has a number of advantages, which arise from the greater available thicknesses and higher Z of Ge in comparison to Si. The GeDSSD offers an increased β-decay detection efficiency, and also offers a high efficiency for the detection of low-energy γ rays and conversion electrons, making this detector ideal for the observation of isomeric states. Lower energy transitions are expected to have a longer half-life, based upon the Weisskopf estimate of their decay constant (See Section 2.3.1). Therefore, the study of low energy γ rays is important.

1.2 Application of β-decay and isomer spectroscopy to A$\sim$110 nuclei

One region of the nuclear chart that has long been thought to exhibit signatures of changing nuclear shape [7] is the mass number A$\sim$110 neutron rich Zr, Nb, Mo, Ru, Rh, and Pd nuclei. While there are several interesting aspects of these nuclei, the search for isomeric states can address the effects of the $\nu h_{11/2}$ orbital on the structure in the region. With neutron numbers ranging between the N=50 and N=82 shell closures, many positive parity orbitals are available, with the possibility of excited, high-spin, negative parity states arising from the $h_{11/2}$ orbital. Several of the isotopes in this region have negative parity isomeric states [3–5, 8–13], with half-lives varying from 14 ns [10] up to 5.5 h [8].

1.2.1 Shell model introduction

Experimental efforts have been carried out into more and more neutron rich nuclei, and many research groups have put forth theoretical efforts to explain the observed phenomena (for example: the prevalence of isomeric states, signatures of large prolate deformations), and to predict whether additional changes in the shapes of the nuclei are expected at higher neutron numbers [14–22]. However, the experimental classification of the region is far from complete, and theoretical predictions vary for the nuclear deformations, as well as the location along isotopic chains where the changes in nuclear shape are expected.

The observed shape evolution of the A$\sim$110 nuclei arise from changes in the underlying nuclear structure. In the shell model description of the nucleus [1], protons and neutrons are arranged in a series of shells, and the spacing and filling of these shells determine the properties of a specific isotope. This is analogous to the behavior exhibited by electrons in atomic systems, where the periodic trends of the elements reflect an underlying shell structure. When an entire shell is filled, as is the case for the noble gases, the amount of energy to remove a single electron increases, and the system exhibits an increased stability. The ionization energy for atomic electrons is shown in Fig. 1.1.

In nuclei, similar peaks are seen in the neutron and proton separation energies, or the energy required to remove a neutron from the nucleus. The numbers of protons and neutrons resulting in relatively more stable nuclei than the neighboring nuclei are referred to as magic numbers. The number of nucleons that form closed shells for neutrons and protons are different from those of the electron shells due to a different underlying interaction potential. Known magic numbers for both neutrons and protons are 2, 8, 20, 28, 50, 82, and for neutrons, an additional magic number of 126 is known. The spherical shell model [24] describes the nucleus as a set of finite energy levels existing as orbitals within a nuclear potential. As more protons and neutrons are added to a nucleus, higher energy orbitals become filled.

The evolution of nuclear structure can also be studied from the standpoint of collective exci-

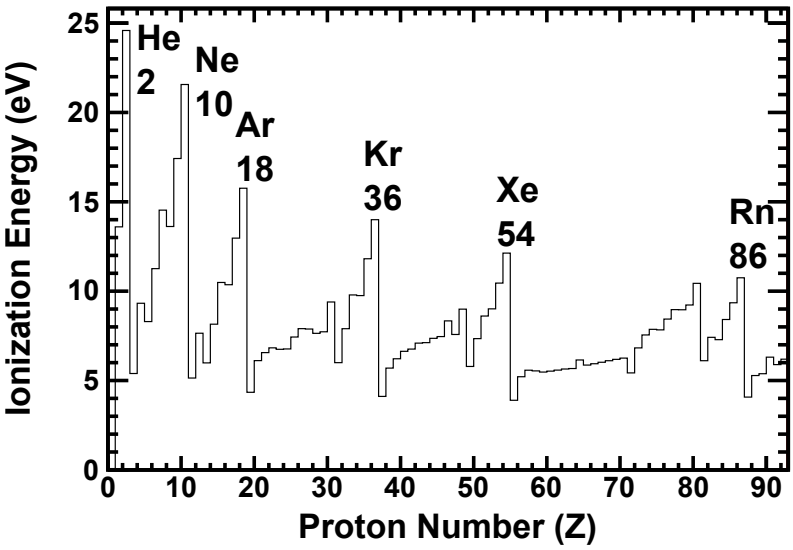

Figure 1.1 The ionization energy, or the energy required to remove an electron from a given element is shown for elements up to Z=92. Noble gases are marked, with their Z given below the elemental name. The data are from Ref. [23].

tations, or excitations involving multiple nucleons. One of the effects of some types of collective excitation is a change in the shape of the nucleus, which can be observed, for example, in rotational motion of that nucleus. The deformation of the nucleus can be described by its electric quadrupole moment for axially symmetric deformations, with a spherical nucleus having a moment of 0 e-barns, a prolate (football-like) nucleus having a positive moment, and an oblate nucleus (discus-like) having a negative quadrupole moment. Prolate and oblate deformations are ellipsoidal shapes where two of the axes of the ellipsoid are the same in length, with the third axis elongated or compressed. The quadruople moment may be expressed as follows [1]:

$$Q = \left(\frac{2}{5}\right) Ze(b^2 - a^2) \tag{1.1}$$

where Q is the quadrupole moment, Z is the proton number, e is the charge of the electron and a and b are the semi-minor and semi-major axes of the ellipse. The deformation of the nucleus can be parameterized [1] based upon the length of the axes of the ellipse:

$$\beta = \frac{4}{3}\sqrt{\frac{\pi}{5}}\frac{b-a}{R_{avg}} \tag{1.2}$$

where a and b are the semi-minor and semi-major axes, respectively, R_{avg} is the average radius $R_{avg}^2 = \frac{1}{2}(a^2 + b^2)$, and β is referred to as the deformation parameter. For spherical nuclei, β is 0, while prolate and oblate nuclei have a positive and negative β, respectively.

The Nilsson model describes the evolution of the spherical shell model orbitals when placed into a deformed nuclear potential [1]. The splitting of the nuclear orbitals, removing orbital degeneracy, as a function of the deformation parameter, β, is one of the model predictions. For example, a Nilsson diagram for A$\sim$110 nuclei was calculated in Ref. [25] (Fig. 1.2). The energy levels are split according to the projection of the single-particle angular momentum onto the nuclear symmetry axis, and are represented by the quantum number Ω. A spherical orbital will split into $(2j+1)/2$ levels, where j is the total orbital angular momentum, with the highest angular momentum states highest in energy for prolate deformations and the lowest angular momentum states highest in energy for oblate deformations (Fig. 1.3). Therefore, the ground-state spins and parities of odd-A nuclei can help with identifying the degree of deformation as a function of A within an isotopic chain. Higher-lying orbitals within the calculation with different spins and opposite parities are associated with the presence of low-lying isomeric states.

1.2.2 Ru isotopes

Several isotopic chains in the A$\sim$110 region show evidence of changing nuclear shape and theory likewise predicts a change in nuclear shape as A increases along these isotopic chains. Examples of changing nuclear shape include reduced energies in the first excited 2^+ states in even-even nuclei [26–28] (spherical nuclei have high first excited 2^+ energies due to gaps between closed shells), high spin data in odd-A nuclei [28, 29] (band-crossing may be related to shape transitions), and reduced quadrupole transition strengths [30] (the quadrupole moment is related to the deformation parameter by Eq. 1.1). Individual theories predict changes at different mass numbers. Isomeric states in odd-A nuclei can be used to search for fingerprints of deformation by constraining the spin and parity of nuclear states. Because isomers can arise due to large changes in spin or a change in parity, in addition to lower energy transitions delaying the transition rate, between two

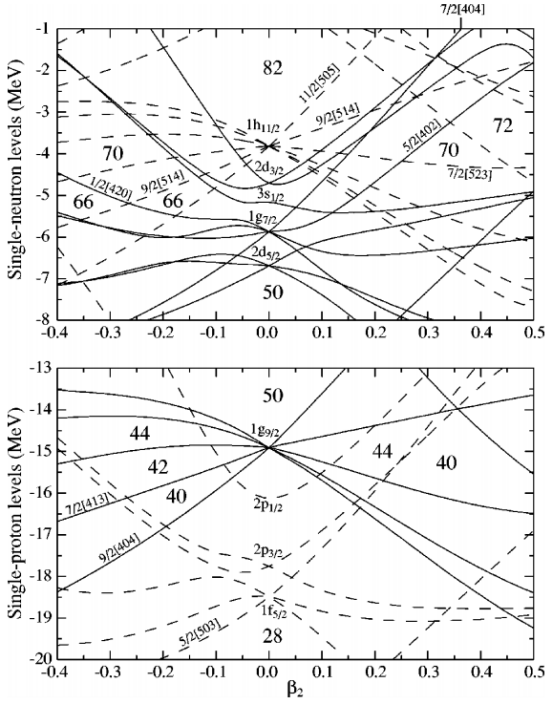

Figure 1.2 Nilsson diagram for nuclei with A∼110 reproduced from Ref. [25].

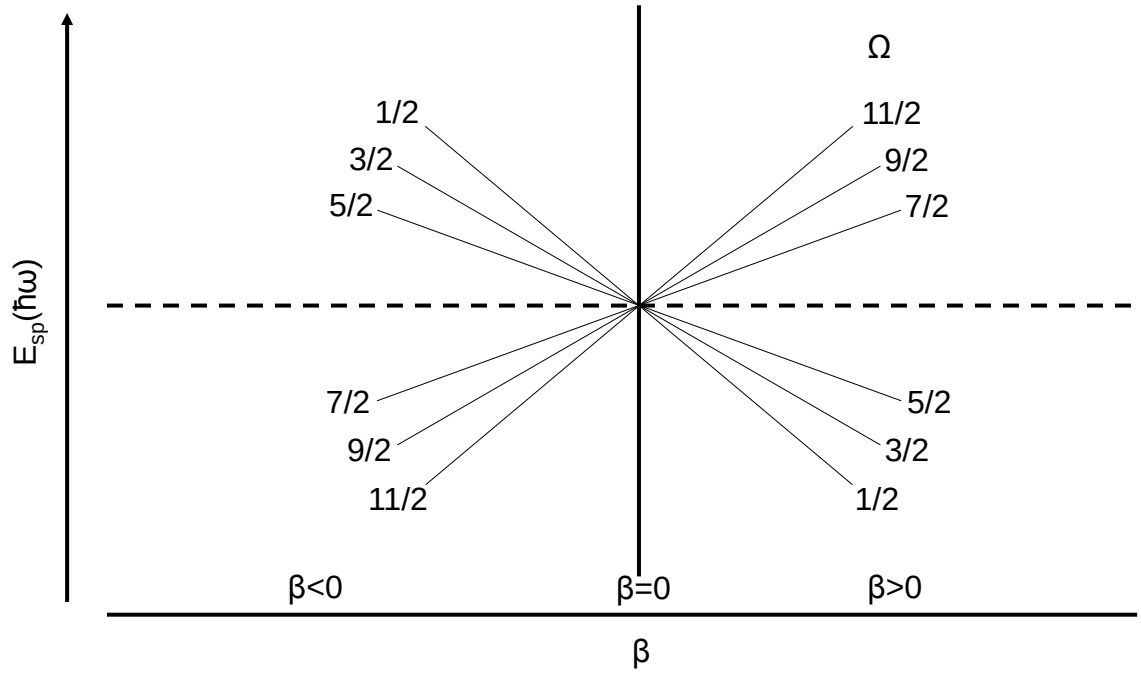

Figure 1.3 Schematic drawing illustrating the energy splitting of the $h_{11/2}$ orbital as a function of deformation parameter, β. The single particle energy increases toward the top of the figure.

levels, the character of the transition indicates the magnitude of the change (See Section 2.3.1 for more details). For the Ru isotopes with N between 50 and 82, there is only a single orbital, the $h_{11/2}$ orbital, with a negative parity. Thus if the multipolarity of an isomeric transition indicates that there is a change in parity, one of the two states most likely arises from this orbital. For example, in ^{115}Ru, an M2 isomeric transition indicating a change in parity was found [5]. The ground-state spin and parity, which was found to tentatively be $(3/2^+)$ [12], is difficult to place in a prolate or spherical configuration (Fig 1.2) with N=71, and therefore could signal a shift to more oblate shapes. This section will briefly outline the considerations that led to the present study, using the Ru isotopic chain as an example to illustrate the kind of structural evolution present in the A$\sim$110 region of the nuclear chart.

1.2.2.1 Previous experimental results

In the Ru isotopic chain, the heaviest nucleus with previously measured excited states is ^{117}Ru [31]. An isomeric state at 185 keV with a half-life of $2.487^{+0.058}_{-0.055}$ μs with an unknown spin and parity was observed and no spin or parity was assigned for the ground-state [31]. Fig. 1.4 illustrates the systematics for several odd-A Ru isotopes as a function of A. For these nuclei, 63$\leq$N$\leq$71, available neutron orbitals (Fig. 1.2) include the even parity $2d_{5/2}$, $1g_{7/2}$, $3s_{1/2}$, $2d_{3/2}$ and the odd parity $1h_{1/2}$ orbitals. The expected ordering of the orbitals between N=50 and N=82 is illustrated in Fig. 1.5. Thus, negative parity states, some of which may be isomeric, can arise from an unpaired neutron in the $h_{11/2}$ orbital, while positive parity states could potentially arise from the unpaired neutron occupying any one of the other orbitals. For less massive Ru isotopes, the evolution of the spins and parities of the energy levels can provide some insight into the changing nuclear structure.

In the less massive odd-A nuclei, the spins and parities of the ground-states can be compared to the expected spins and parities on a Nilson diagram such as the one shown in Fig. 1.2 in order to gain some insight as to whether these nuclei are prolate or oblate deformed. These nuclei show the progression of spins and parities leading up to the nuclei discussed in this work, and are

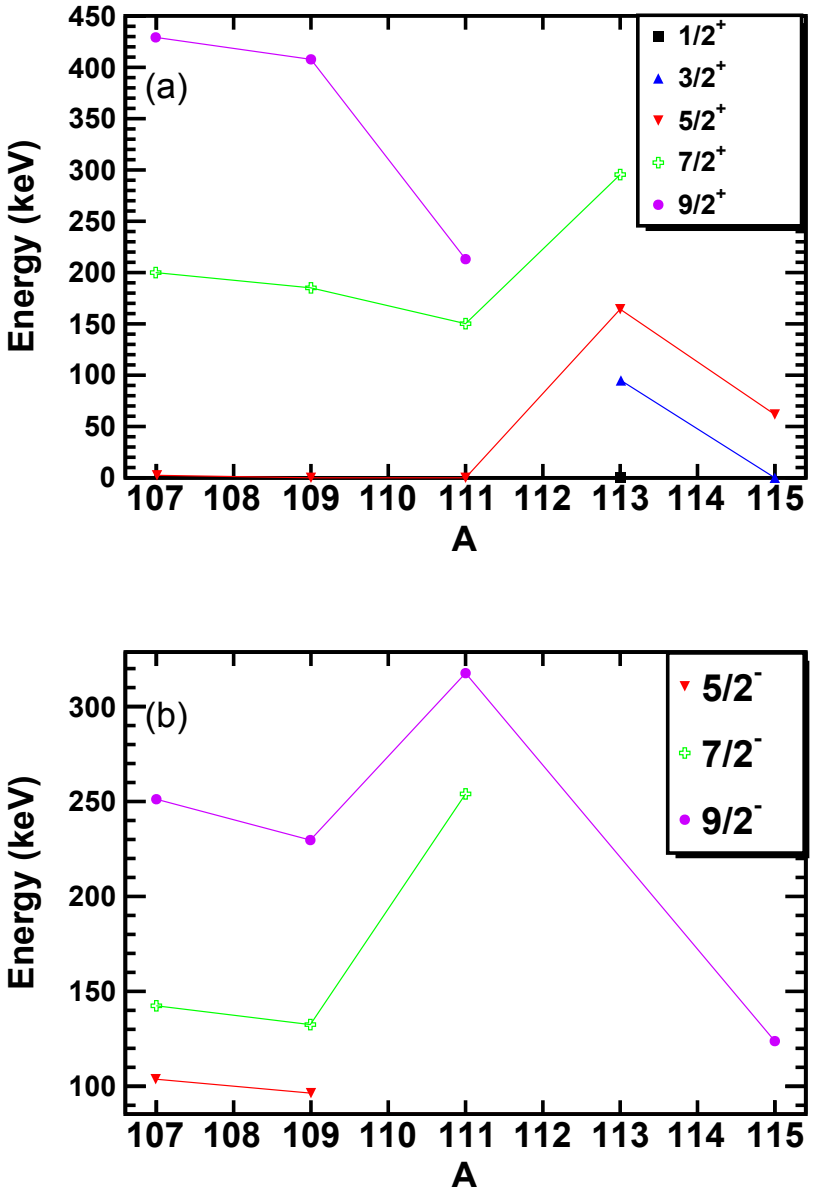

Figure 1.4 Evolution of spins and parities in the Ru isotopic chain [5, 12, 29, 32–34] shown for (a) positive parity states and (b) negative parity states. The $(7/2^+)$ state in ^{113}Ru could also be a $(5/2^+)$. There is also a $(7/2^-)$ β-decaying isomer at unknown energy in ^{113}Ru, with a $(9/2^-)$ state 112.9 keV above it [34].

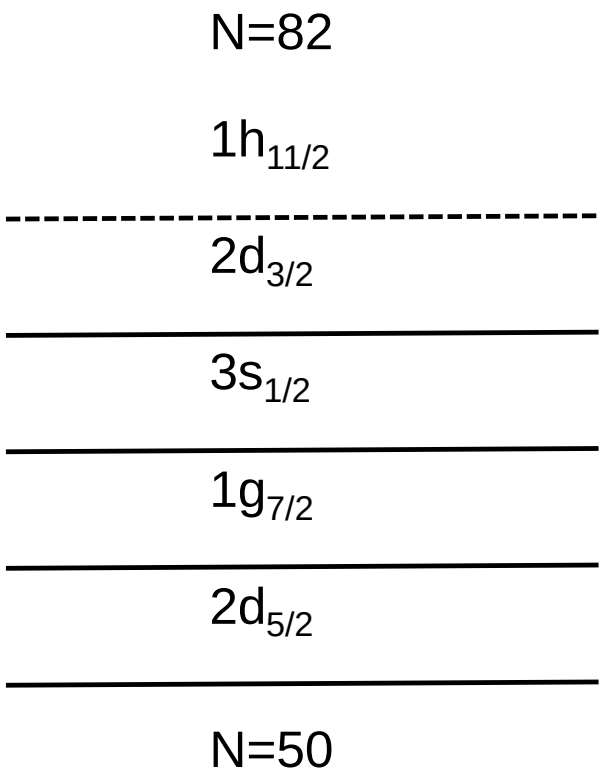

Figure 1.5 Schematic of the ordering of orbitals between N=50 and N=82. The ordering is based upon the calculations in [25]. Positive parity orbitals are shown with a solid line, while negative parity orbitals are drawn with a dashed line.

representative of the nuclei within the A$\sim$110 region of the chart of the nuclides. Results from B(E2) measurements indicated a deformation parameter, β in the even A isotopes between ^{102}Ru and ^{108}Ru to increase from 0.20 to 0.25 [35]. Other work measuring lifetimes in ^{108,110}Ru found a β of 0.29(1) [36]. Therefore, the spins and parities of the odd-A isotopes may be compared to the Nilsson diagram at β between approximately 0.2 and 0.3 for isotopes with A less than 110. In ^{107}Ru (N=63), the ground-state spin and parity is ($5/2^+$) [32]. This spin and parity can be obtained if the odd neutron in ^{107}Ru occupies the $d_{5/2}$ single particle state in the Ω=5/2 projection at a deformation of $\beta\sim$0.3. Adding two neutrons to N=65, the ground-state spin and parity of ^{109}Ru is ($5/2^+$) [29], which given a deformation parameter of $\sim$0.15 would populate the Ω=5/2 projection of the $g_{7/2}$ orbital. With two additional neutrons (N=67), ^{111}Ru also has a ground-state spin and parity of ($5/2^+$) [33], placing a neutron in the $g_{7/2}$ orbital at slightly higher prolate

deformations. There is, however, some high-spin data that suggests a transition to oblate excited states at A=111 [28, 29].

A spin and parity of ($1/2^+$) [34] for the N=69 ^{113}Ru isotope could signal a shift to oblate shapes, as the prediction according to the diagram in Fig. 1.2 suggests a spin and parity of ($5/2^-$) for a $\beta\sim$0.2 in an $h_{11/2}$ orbital. One way to explain this this observation would be the population of the $s_{1/2}$ orbital at $\beta\sim$-0.15. Alternately, placing a neutron into the $d_{3/2}$ orbital at very slight oblate deformations could also yield a spin and parity of ($1/2^+$) at N=69. Finally, adding two more neutrons, reaching ^{115}Ru (N=71) the spin and parity of the ground-state is expected to be ($3/2^+$) based upon β feedings and systematics [12]. Oblate states from the $d_{3/2}$ orbital at a $\beta\sim$-0.15 could explain the spin and parity. While lighter isotopes give experimental suggestions of prolate configurations, certainly more work in the heaviest Ru isotopes is needed to clarify the interpretation. By using experimental evidence to deduce the ground-state spins and parities in the more massive nuclei, the variation of deformation within the A$\sim$110 nuclei can be clarified. It is important to note that the spins and parities of many of the levels in these nuclei are uncertain, so firming up the spin and parity assignment would clarify the interpretation further, as incorrect spin and parity assignments could change the interpretation of the results.

Experimental results for the heaviest odd-A Ru isotopes have found isomeric states with spins and parities of ($7/2^-$) and ($9/2^-$), which would most likely originate from the neutron $h_{11/2}$ orbital [4, 5, 10–12, 34], at an oblate deformation of $\beta\sim$-0.15. Several of these isomeric states have a known half-life but unkown energy. Partial level schemes for the isotopes with isomeric states are shown in Fig. 1.6. It is therefore important to place these isomeric state at exact energies and to search for more isomeric states in heavier Ru isotopes, and the neighboring isotopic chains. The energy of a given isomeric state is related to its half-life: the lower the energy, the longer the half-life [1] (See Section 2.3.1 for more details about the relation between transition energy and decay constant). With the energy of a transition known, an estimate for the decay constant called the Weisskopf estimate may be calculated. This varies depending upon the character of the transtion, which in turn is indicitive of the change in spin and parity between the two states.

In the A∼110 region of the nuclear chart, for unpaired neutrons, a change in parity indicates that the $h_{11/2}$ orbital is populated by one of the two states. Once identified, conversion electron spectroscopy following the isomeric decays can be used to determine transition multipolarities and to check the tentative spin and parity assignments. States in high-mass nuclei with low transition energies and high multipolarities will likely have strong conversion electron emission. The emitted conversion electrons can easily be missed in many detection systems. The GeDSSD may be used to study these nuclei to search for the unobserved low-energy electrons.

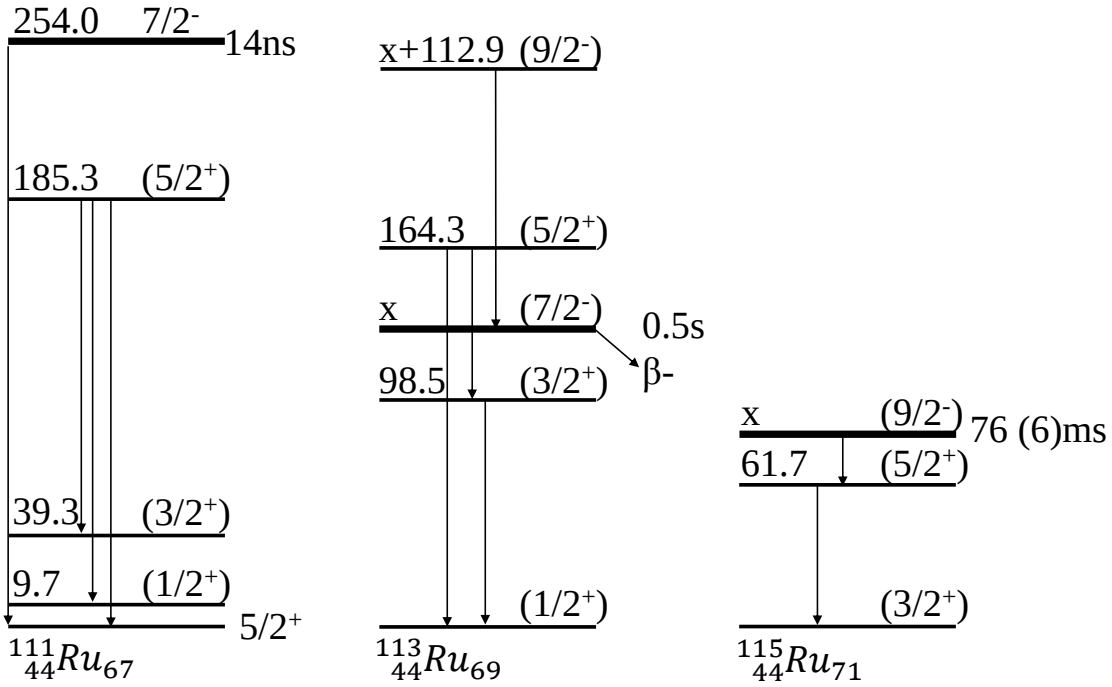

Figure 1.6 Partial level schemes for the heaviest odd-A Ru isotopes. Experimental data from [4, 5, 10–12, 34].

1.2.2.2 Theoretical predictions

There has been much theoretical work focused on describing the observed deformations in the A∼110 region. While many of the calculations predict changes in nuclear shape along the isotopic

chains in this region, the calculations differ as to the exact location of the shape changes. Some theoretical predictions for Ru isotopes are shown in Fig. 1.7.

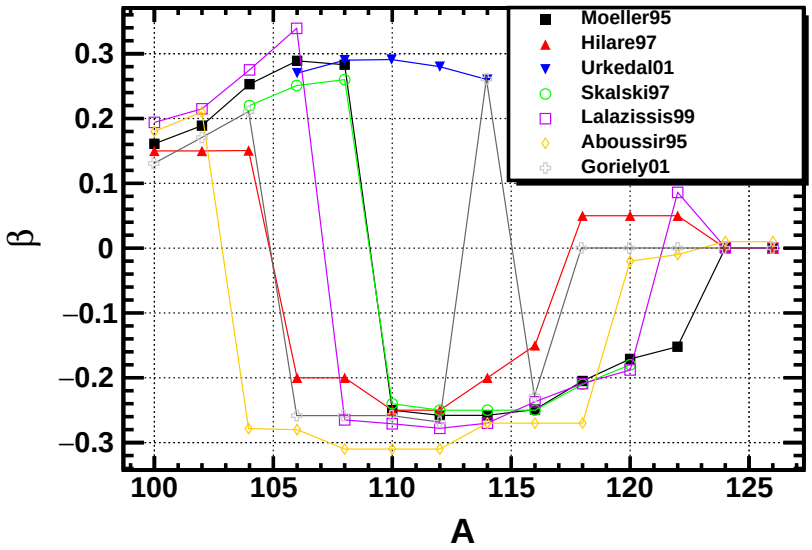

Figure 1.7 Theoretical Predictions of the deformation parameter, β for Ru isotopes. References in order of legend: [14–18, 20, 21].

In Ru isotopes, a transition between nuclear ground-state shapes from prolate to oblate is predicted anywhere from A=104 [20] to A=110 [14, 17], remaining prolate in one calculation up to A=114 [16]. At higher neutron numbers, the calculations eventually return to more spherical shapes.

1.3 Dissertation outline

This work describes the characterization and use of a GeDSSD to observe and identify isomeric states in exotic nuclei. β, γ, and electron spectroscopy will be detailed in Chapter 2. The GeDSSD will be described in more detail in Chapter 3, focusing on two experiments used to characterize the detector.

The rest of the document will detail the results of the application of the GeDSSD to the study of the nuclear structure of A$\sim$110 nuclei. Chapter 4 will detail the setup of the NSCL experiment,

including analytical techniques and data acquisition techniques not discussed previously, as well as ion identification. The results of the experiment will be detailed in Chapter 5, split into three sections: long-lived isomers (focused on ^{115}Ru), short-lived isomers and β-delayed γ rays.

Finally, Chapter 6 will summarize and conclude the presentation.

CHAPTER 2

TECHNIQUE

2.1 Introduction

This chapter includes a discussion of the experimental techniques used within this work. First, the principles of β-decay spectroscopy will be presented. Then, other transitions and radiation types that may be present in β decay and finally the detector systems utilized in this study will be presented,

2.2 β-decay spectroscopy

2.2.1 β decay

β decay is a selective spectroscopic tool that is used extensively to study nuclear structure. β-decay spectroscopy can be used to measure a variety of nuclear structure observables, including half-lives, branching ratios, and excited state energies. This information can be combined to offer constraints on the spins and parities of states. In β decay, a parent nucleus decays to its daughter, converting a proton into a neutron (or vice-versa), keeping the total number of nucleons constant. There are three modes of β decay:

$$\beta^- : {}^{\mathrm{A}}Z_N \rightarrow {}^{\mathrm{A}}(Z+1)^{+}{}_{\text{(N-1)}} + \beta^- + \bar{\nu}_e + Q_\beta \tag{2.1}$$

$$\beta^+ : {}^{\mathrm{A}}Z_N \rightarrow {}^{\mathrm{A}}(Z-1)^{-}{}_{\text{(N+1)}} + \beta^+ + \nu_e + Q_\beta \tag{2.2}$$

$$EC : {}^{\mathrm{A}}Z_N + e^- \rightarrow {}^{\mathrm{A}}(Z-1)_{\text{(N+1)}} + \nu_e + Q_\beta \tag{2.3}$$

where β is a beta particle (positron or electron), e^- is an atomic electron, ν_e is an electron neutrino, $\bar{\nu}_e$ is an electron anti-neutrino, and Q_β is the β-decay Q-value of the reaction. β decay occurs through a series of isobars (nuclei with the same A) ending at a stable nucleus.

The half-lives of β-decaying nuclei vary greatly across the chart of the nuclides, ranging from milliseconds in the most exotic nuclei to thousands or even billions of years in nuclei closer to stability. Assuming that a radioactive sample starts with no daughter nuclei present, the number of ions of any generation at any time, t, can be expressed using the Bateman equations as follows [1]:

$$N_n = C_1 e^{-\lambda_1 t} + C_2 e^{-\lambda_2 t} + C_3 e^{-\lambda_3 t} + ... + C_n e^{-\lambda_n t} \tag{2.4}$$

where N_n is the number of nuclei of the nth generation at time t, λ is the decay constant, t is time, and the C_n coefficients are [1]:

$$C_n = \frac{\lambda_1 \lambda_2 .... \lambda_{n-1}}{(\lambda_1 - \lambda_n)(\lambda_2 - \lambda_n)...(\lambda_{n-1} - \lambda_n)} N_1^0 \tag{2.5}$$

where N_1^0 is the number of parent nuclei at time $t = 0$. The Bateman equations may be used to extract the number of nuclei and the decay constant of a parent nucleus from the variation of the activity with time. A decay curve plotting the time difference between the detection of the arrival of the parent nucleus to the experimental station (assuming the time between the production of the ion and it's transport to the experimental station is negligible on the time scale of the decay) and the detected electron emission from the nucleus may be fit with contributions from the decaying parent, the growth and decay of the daughters, and typically, constant background events, yielding the decay constant of the parent λ_1. The half-life is simply determined via the relation:

$$T_{1/2} = \frac{ln(2)}{\lambda} \tag{2.6}$$

The total number of nuclei may be found by integrating the number of counts under the exponential curve of the parent decay, if all parent nuclei decay and taking into account the detector's efficiency.

β decay can populate multiple states in the daughter nucleus, which subsequently further decay toward the ground-state. A general schematic of β^- decay is displayed in Fig. 2.1. γ rays or conversion electrons emitted following β decay are referred to as "β-delayed" particles.

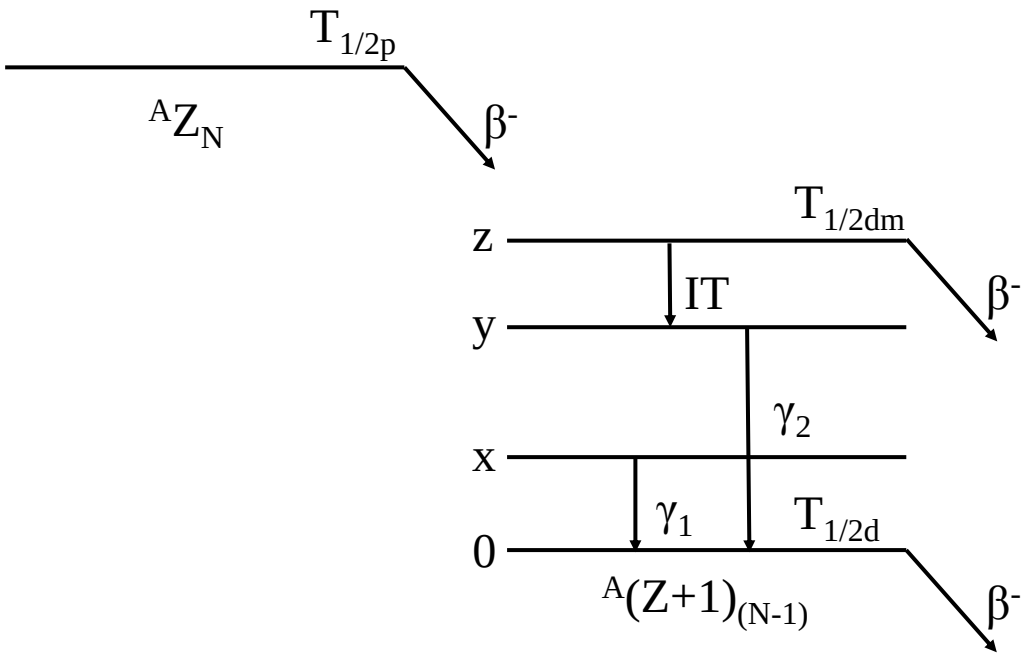

Figure 2.1 In this general schematic of β^- decay, multiple states are populated in the daughter nucleus, with the highest excited state shown here as an isomeric state, with competing β-decaying and internal transition de-exitations. Figure labels: IT, internal transition; $T_{1/2}$, half-life; γ, γ ray; β^-, β decay; p, parent; d, daughter; m, metastable state.

2.2.2 β-decay selection rules

The selection rules for cases where there is no net orbital angular momentum carried by the electron and antineutrino are a change in nuclear spin, ΔJ, of 0 or 1, and no change in parity, $\Delta\pi$=0. Such a decay is referred to as an "allowed decay". Decays with a change in net angular momentum or a change in parity are referred to as "forbidden decays". Despite what the name implies, forbidden decays do occur, albeit at a significantly lower rate compared to allowed transitions. The selection rules for β decay are summarized in Table 2.1.

One method to distinguish between allowed and forbidden decays is through their ft value called the comparative half-life. The t refers to the partial half-life of the β decay to the particular state of interest, which may be calculated from the branching ratio, BR_i:

$$\lambda_i = \lambda BR_i \tag{2.7}$$

$$T_{1/2i} = \frac{ln(2)}{\lambda_i} \tag{2.8}$$

Table 2.1 β-Decay Selection Rules [1].

Transition Type	$\Delta\pi$	ΔJ	logft
Superallowed	No	0	2.9-3.7
Allowed	No	0, 1	4.4-6.0
First Forbidden	Yes	0, 1, 2	6-10
Second Forbidden	No	1, 2, 3	10-13
Third Forbidden	Yes	2, 3, 4	>15

where λ is the total decay constant, λ_i is the partial decay constant to a given state and $T_{1/2i}$ is the partial half-life for the decay to the state. The partial half-life is multiplied by the Fermi integral, f to find the ft value for the decay [37]. Values for the Fermi integral that represent the phase-space available to the decay are available in tabulated form, for example in Ref. [38]. As half-lives can vary by many orders of magnitude, ft values are often reported as logft [1]. The logft ranges for the various types of β decay are indicated in the last column of Table 2.1.

2.3 Electromagnetic transitions

2.3.1 γ decay

The multipolarity of an emitted γ ray varies depending upon the change in parity and spins of the final and initial states, as described by:

$$|J_i - J_f| \leq l \leq (J_i + J_f) \tag{2.9}$$

where J is the nuclear spin of the initial (i) and final levels (f) and l is the amount of angular momentum carried away by the γ ray. It is forbidden for a single photon to carry away 0 $\hbar$ units of angular momentum; a 0^+ to 0^+ transition must occur via internal conversion or internal pair production (possible only when the energy of the transition exceeds 1.022 MeV). A γ-ray transition is classified by its multipolarity (Table 2.2) and also whether it is an electric or magnetic transition, the latter dictated by the change in parity of the nuclear states.

Table 2.2 γ-ray Multipolarities [1].

Multipolarity	l	$\Delta\pi$
E1	1	Yes
M1	1	No
E2	2	No
M2	2	Yes
E3	3	Yes
M3	3	No
E4	4	No
M4	4	Yes

The γ-ray transition rate depends on its character and multipolarity. One commonly used estimation of transition rate (λ) is the Weisskopf Single-Particle estimate [1]. This estimate assumes that a given transition is the result of a single nucleon moving between two states. The equations for transition rates of the first 5 multipolarities of both electric and magnetic transitions are given in Table 2.3. Note that electric transitions of the same multipole are faster than the corresponding magnetic transition, and higher multipole transitions are slower than lower multipoles of the same type. Experimental lifetimes for transition rates can be hindered or enhanced by a few orders of magnitude in comparision to Weisskopf estimates [37] by nuclear effects. Typically, E2 values are enhanced over their Weisskopf estimates [1], while E1 transitions are more hindered [37]. Weisskopf estimates can be useful for the analysis of isomeric states where there are multiple possible de-exitations possible. The estimates can also be useful in assigning multipolarities to specific transitions, where Weisskopf estimates are compared to experimental transitions rates, and the degree of agreement indicates the accuracy of the assumption of a single particle transition.

2.3.2 Internal Conversion

A process that competes with γ-ray emission is internal conversion-electron emission. Internal conversion occurs when a nucleus in an excited state interacts with an atomic electron and the electron is subsequently emitted from the nucleus. The vacancy is filled by outer shell electrons,

Table 2.3 Weisskopf Single-Particle Transition Rates (E_γ in MeV) [1].

Multipole (l)	E (λ s^{-1})	M (λ s^{-1})
1	$1.03\times10^{14}A^{2/3}E_\gamma{}^3$	$3.15\times10^{13}E_\gamma{}^3$
2	$7.28\times10^{7}A^{4/3}E_\gamma{}^5$	$2.24\times10^{7}A^{2/3}E_\gamma{}^5$
3	$3.39\times10^{1}A^{2}E_\gamma{}^7$	$1.04\times10^{1}A^{4/3}E_\gamma{}^7$
4	$1.07\times10^{-5}A^{8/3}E_\gamma{}^9$	$3.27\times10^{-6}A^{2}E_\gamma{}^9$
5	$2.40\times10^{-12}A^{10/3}E_\gamma{}^{11}$	$7.36\times10^{-13}A^{8/3}E_\gamma{}^{11}$

emitting X-rays or Auger electrons. The emission of Auger electrons occurs when the energy from filing a vacancy in the electron shells is transferred to another electron, which is then emitted. The fluorescence yield describes the ratio of X-ray emission to Auger electron emission [39]. The energetics of internal conversion is governed by the following equation:

$$E_{IC} = E_T - E_{BE} \tag{2.10}$$

where E_{IC} is the energy of the conversion electron, E_T is the energy of the transition, and E_{BE} is the binding energy of the atomic electron.

For a given transition, the internal conversion coefficient, α gives the relative intensity of γ-ray and internal conversion transitions [1]:

$$\alpha = \frac{number\ of\ conversion\ e^-}{number\ of\ \gamma\ rays} = \frac{\lambda_{IC}}{\lambda_\gamma} \tag{2.11}$$

where λ_{IC} is the transition rate of conversion electrons and λ_γ is the transition rate of γ rays. The total internal conversion coefficient, α_{tot} is the sum of conversion coefficients over all atomic subshells [1]:

$$\alpha_{tot} = \alpha_K + \alpha_L + \alpha_M + ... \tag{2.12}$$

where K, L, and M represent the atomic subshells. The conversion coefficient for shells closer to the nucleus will tend to be higher than that for shells farther from the nucleus, given the greater ease of interaction with the nucleus due to proximity.

Internal conversion coefficients can be utilized to infer the multipolarity of a transition. Approximate formulas for internal conversion coefficients are [1]:

$$\alpha(El) = \frac{Z^3}{n^3}\left(\frac{l}{l+1}\right)\left(\frac{e^2}{4\pi\varepsilon_0\hbar c}\right)^4\left(\frac{2m_ec^2}{E}\right)^{l+5/2} \tag{2.13}$$

$$\alpha(Ml) = \frac{Z^3}{n^3}\left(\frac{e^2}{4\pi\varepsilon_0\hbar c}\right)^4\left(\frac{2m_ec^2}{E}\right)^{l+3/2} \tag{2.14}$$

where l is the multipole order, n is the principle quantum number of the ejected electron, and $\frac{e^2}{4\pi\varepsilon_0\hbar c}$ is the fine structure constant, which is $\sim$1/137. From these relations, one can see that internal conversion becomes more important at heavier masses, and lower-energy transitions. In equations 2.13 and 2.14, one assumes that only the lowest l contributes, that the binding energy in the K shell is less than the transition energy, and finally that relativistic effects may be ignored [40].

There are two complimentary methods to determine conversion coefficients: detecting the X-rays or detecting the emitted conversion electrons themselves. Measuring the conversion elections directly is preferred. Alternately, the number of detected k-shell X-rays (corrected for detector efficiency) can be taken as a measure of the number of conversions. However, if there are multiple converting states within a nucleus, and no coincident transitions to gate upon, this method will not be able uniquely determine the conversion coefficients.

2.4 β-decay spectroscopy experimental design

An overview of β-decay spectroscopy at fragmentation facilities such as the NSCL is presented in this section. Data will be presented from three different experiments carried out at the NSCL, e11503, e09055, and e11003, which were focused on ^{67}Fe, ^{54}Ni, and A$\sim$110 nuclei, respectively. The first two experiments were used to characterize specific aspects of the GeDSSD's performance for the detection of electrons while the last was the study of isomeric states near A=110. The features in common to all of the experiments will be provided here and more detail will be given in later chapters.

All isotopes were produced at the NSCL in fragmentation reactions at the Coupled Cyclotron Facility (CCF). The A1900 fragment separator [41] selected the ions of interest out of those produced in the target. The separated ions then passed through thin PIN diode detectors, which were utilized for energy loss (ΔE) and time of flight (TOF) measurements. Energy loss and time of flight measurements allowed isotopic identification on an event-by-event basis. Ions were then delivered to the experimental station and deposited in a position-sensitive semiconductor detector. Instead of using a Si Double-Sided Strip Detector (DSSD) for this purpose [42–49], the ions were implanted into a GeDSSD [6] in the present series of experiments. The GeDSSD was surrounded by arrays of other detectors to observe β-delayed γ rays escaping the central detector. Arrays that have been utilized in conjunction with the GeDSSD include the Segmented Germanium Array (SeGA) [50] and the Yale Clover array [51].

The implanted heavy ions were correlated with subsequent decays using both position and time information (Fig. 2.2). Valid decay events and heavy-ion implantation events must occur physically close together in the detector, and in a time window that is set based upon the implantation rate and the half-lives of the nuclei. Position determination was accomplished by either taking the strip with the greatest amount of deposited energy for the event or by calculating the energy weighted average strip location. The timing information in the three experiments was provided by a digital data acquisition system.

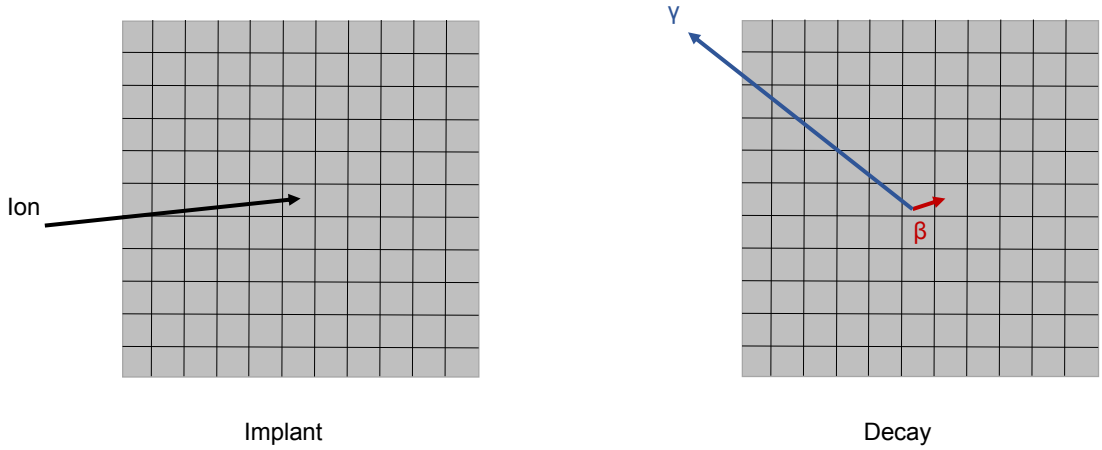

Figure 2.2 Cartoon of β-Decay Spectroscopy. Left side shows the arrival of a heavy ion in the detector, while the right side illustrates the β-decay products.

CHAPTER 3

GERMANIUM DOUBLE-SIDED STRIP DETECTOR

3.1 Introduction

In this chapter the GeDSSD will be discussed in detail. Section 3.2 gives the technical details of the device. The energy calibration of the GeDSSD will be described in Section 3.3. Section 3.4 contains the electron and γ-ray efficiency of the device. Some general experimental techniques will be described in Section 3.5. The chapter will end with a description of two data analysis techniques, β-γ summing and double-pulse analysis in Sections 3.6 and 3.7, respectively.

3.2 Hardware

The GeDSSD is 19-cm in diameter, 1-cm thick, and segmented into 16 by 16 orthogonal, 5-mm strips on the two faces of the crystal. The two sets of strips are referred to as the "back" and "front" of the GeDSSD, and the beam from all experiments entered the detector through the front side. Each of these strips is read out by two preamplifiers with different amplifications, a low-gain for measuring the energy deposited by stopping a high-energy radioactive ion (0-30 GeV) and a high-gain for measuring the β-decay electron and β-delayed transitions (0-15 MeV). The GeDSSD crystal is surrounded by a stainless steel cryostat with thin Al windows on the front and back approximately 1-mm thick and an infrared radiation shield with an additional 0.143 mm effective Al thickness between the crystal and the cryostat. A Sunpower Inc. Stirling Cooler, model CryoTel MT is used to mechanically cool the crystal. The vacuum inside of the cryostat is maintained by an active ion pump. This detector was manufactured by PhDs Co [52] and a schematic drawing of this detector is shown in Fig. 3.1.

The GeDSSD was used with the NSCL Digital Data Acquisition System (DDAS) [53]. The preamplifiers outputs were sent to XIA Pixie-16 modules [54]. Each module processed 16 channels

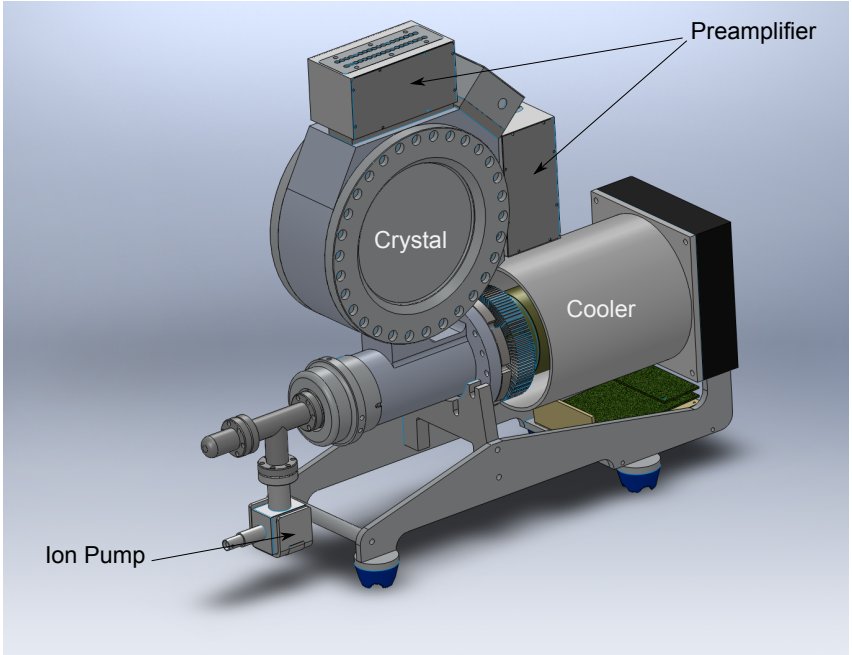

Figure 3.1 A schematic of the GeDSSD. The crystal is housed in the cylindrical region in the center of the image, with the preamplifiers for the two sets of strips to the top and right. The mechanical cooler is located within the bottom right cylinder of the image, and the ion pump is located to its left. This figure is reproduced from Ref. [6].

and digitized the signals with either 100 MSPS (Mega Samples Per Second) and a 12-bit resolution, or 250 MSPS and a 14-bit resolution. Each channel was triggered individually and recorded energy, which was extracted via a trapezoidal filter algorithm [55] with user-controllable parameters and timing information.

3.3 Energy calibrations

3.3.1 Energy extraction techniques

The energies of the incident radiations pulses are proportional to the measured pulse height in the preamplifier. The PIXIE 16 modules [54] output an energy value based upon internal pulse processing using a trapezoidal filter [55]. Traces of the individual waveforms were also recorded for offline processing. For the commissioning runs e11503 and e09055 traces were 6 μs long with the rise of the signal occurring 3 μs into the trace, while the traces recorded for e11003 were 20

μs long with the rise of the signal occurring 4 μs into the trace.

PIXIE used two trapezoidal filters, one for triggering and one for energy extraction. The trigger filter was used to detect the leading edge of the rise of a pulse and trigger the system. The second slower filter was used to determine the energy of the pulse. In both cases, the trapezoidal filter was calculated by subtraction of two integration regions separated by a gap. The shape of the trapezoidal filter output used for energy determination is shown schematically in Fig. 3.2. The filter for the energy determination accounts for the decay time of the signal [55], which was determined for each channel individually. The equation that describes the filter function is as follows:

$$F[i] = a_0\Big[\sum_{j=i-(L-1)}^{i} Trace[j]\Big] + a_g\Big[\sum_{j=i-L-G+1}^{i-L)} Trace[j]\Big] + a_1\Big[\sum_{j=i-(2L+G-1)}^{i-(L+G)} Trace[j]\Big] - kB \tag{3.1}$$

where

$$a_0 = \frac{-(b_1)^L}{1-(b_1)^L} \tag{3.2}$$

$$a_g = 1 \tag{3.3}$$

$$a_1 = \frac{-1}{(b_1)^L - 1} \tag{3.4}$$

$$b_1 = exp\Big[\frac{-\Delta t}{\tau}\Big] \tag{3.5}$$

and F is the value of the filter function at point i, L is the filter length, G is the size of the gap between the subtracted regions, Δt is the sampling time, k is a constant which depends upon the parameters a_0, a_g, and a_1, and B is the baseline of the trace [55].

Other offline, user-defined algorithms were used on recorded traces to determine the energy and identify interesting features for further investigation. A disadvantage of using an offline algorithm is a large increase in the amount of processing time, as looping through each trace individually is computationally time consuming. An offline algorithm may be used to see if the selected trapezoidal filters were optimized, and can improve the energy resolution if that the parameters were not optimized. A simple energy extraction algorithm is to find the highest bin near the rise of the trace and, after subtracting the value of the baseline of the trace, use the height as a measure of

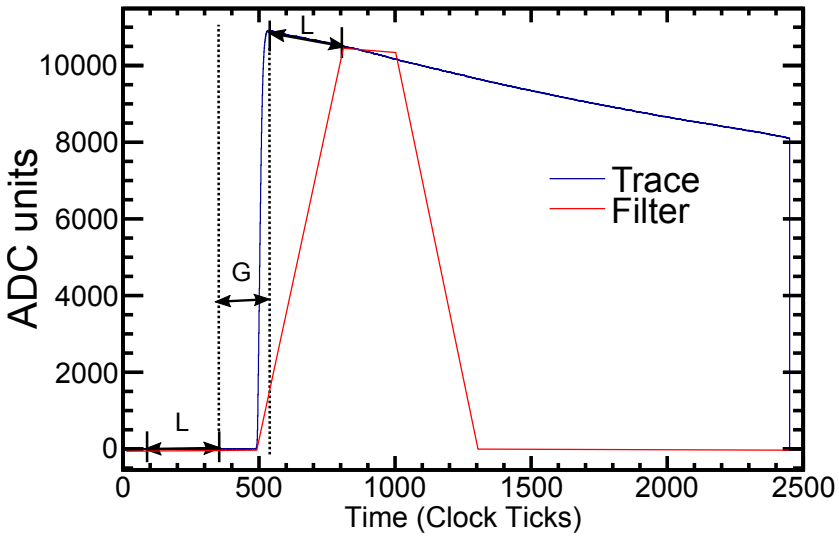

Figure 3.2 A typical trace with the baseline subtracted for one of the back strips (blue curve) and a schematic representation of the shape of the trapezoidal filter output (red curve).

the energy (Fig. 3.3). Alternatively, one could determine the area under the pulse and, after again subtracting the contribution to the area from the baseline of the trace, use the area as a measure of the energy (Fig. 3.4). While the area method is a little more computationally intensive, summing over multiple bins lessens the influence noise or unusual trace features can have on the energy extraction. The resolutions of the various energy extraction techniques are discussed in the next section.

3.3.2 High-gain energy calibration

3.3.2.1 Commissioning runs e11503 and e09055

A ^{137}Cs source was used to calibrate the detector, using a one dimensional (1-D), linear calibration, where the slope and intercept were set individually for each strip. In the commissioning runs, e11503 and e09055, the 662-keV γ ray and the 32-keV X-ray were used to create a two-point calibration.

$$E(keV) = slope[strip] * E(ADCunits) + intercept[strip] \tag{3.6}$$

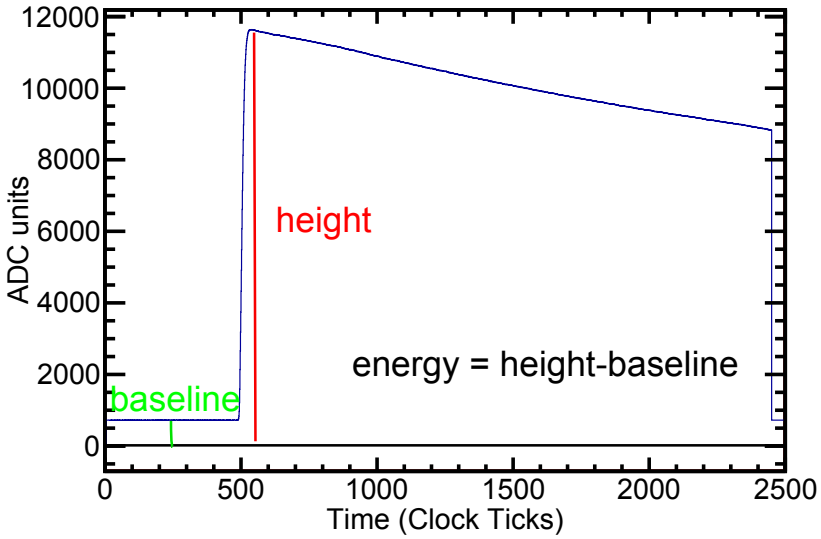

Figure 3.3 A typical trace shape for one of the back strips of the GeDSSD (blue curve) and the baseline height (green) and the trace height (red).

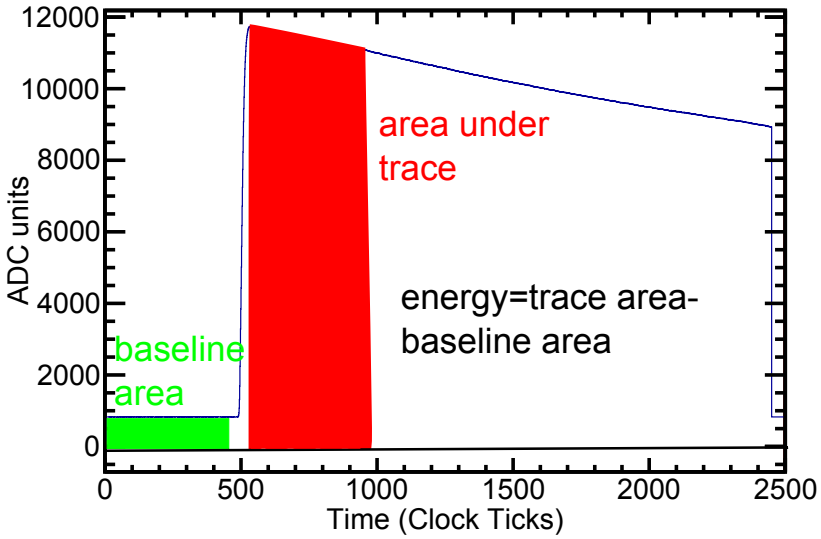

Figure 3.4 A typical trace shape for one of the back strips of the GeDSSD (blue curve) and shown in green and red are examples of the regions of the trace used to obtain a measure of the energy of the trace.

The PIXIE trapezoidal filter energies were used for the energy determination. The results from a ^{137}Cs source calibration taken after the very first commissioning run (e11503) are shown in Fig. 3.5. For the front strips, the FWHM of the middle strips was greater than that of the strips at the edges of the GeDSSD. For the back strips, the FWHM was much more consistent across all strips.

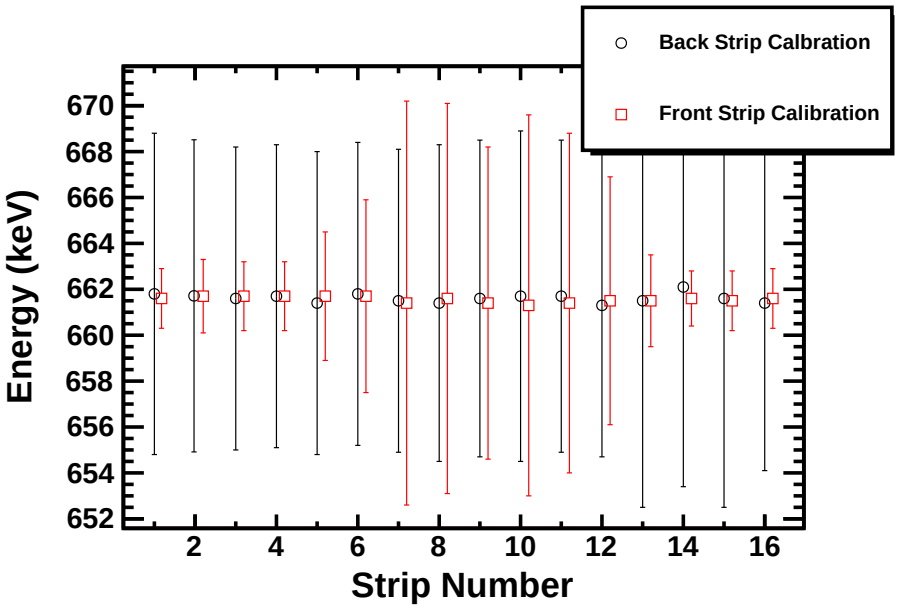

Figure 3.5 The 1-D strip energy calibration for the 662-keV transition from ^{137}Cs measured immediately after the first commissioning run. Error bars indicate the FWHM of the peaks.

The bombardment of the GeDSSD with heavy ions caused radiation damage and a degradation in energy resolution. As shown in Fig. 3.6, the degradation was seen immediately after of the first commissioning run in the front strips of the detector. The entire GeDSSD was not illuminated with ions during the commissioning runs and so the edges of the detector retained their initial resolution while the middle of the detector was damaged. The resolution as a function of ion implantation for the back strips is shown in Fig. 3.7. In the GeDSSD, the generated holes travel to the front of the detector, while the electrons travel toward the back. The radiation damage suffered by the GeDSSD affected the hole migration more than that of the electrons [56] by introducing hole trapping. Thus the resolutions of the back strips were less affected by the bombardment of heavy ions.

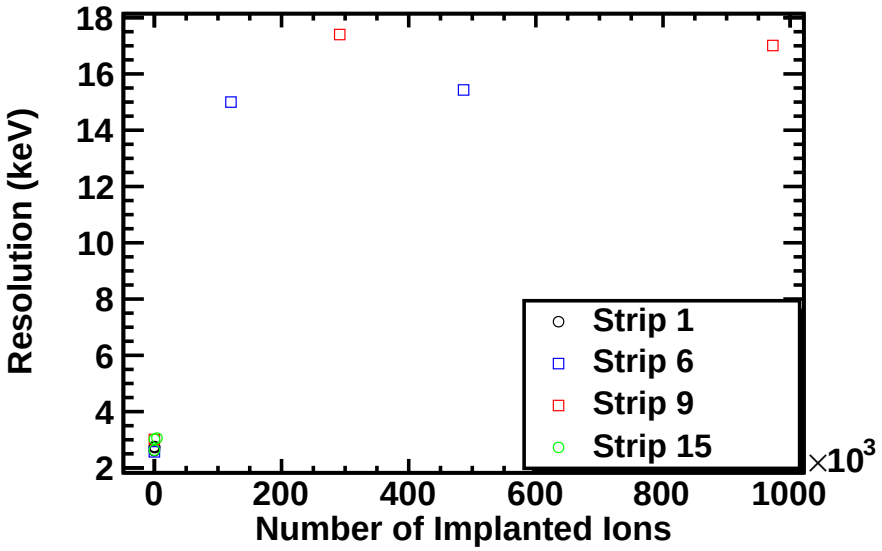

Figure 3.6 The resolutions of the high-gain strips in the GeDSSD for the 662-keV ^{137}Cs transition as a function of number of implanted ions in each individual strip for the first few experiments. Data shown for the front side of the detector, with two edge strips shown as an example (strip 1 and 15 in circles) and two middle strips shown as an example (strips 6 and 9 in square). The resolution worsens as the detector is bombarded.

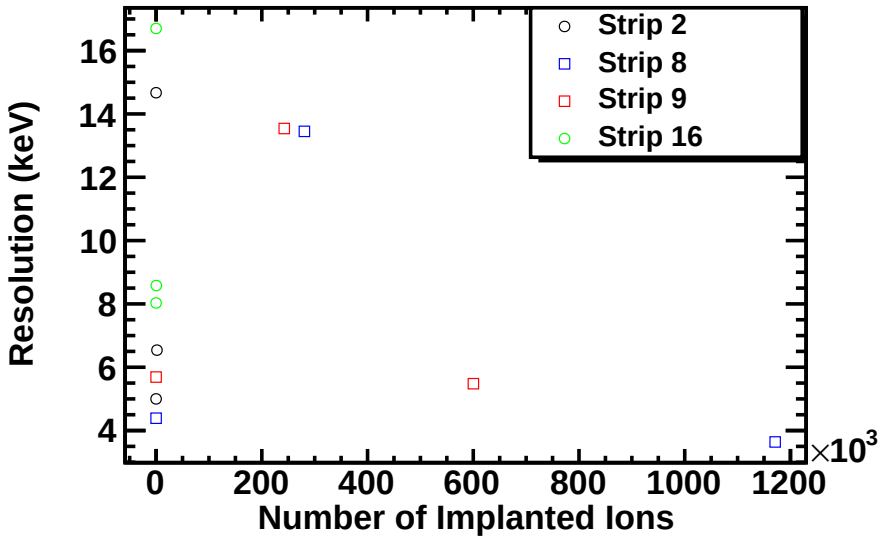

Figure 3.7 The resolutions of the high-gain strips in the GeDSSD for the 662-keV ^{137}Cs transition as a function of number of implanted ions in each individual strip for the first few experiments. Data shown for the back side of the detector, with two representative edge strips (2 and 16 in circles) and two representative middle strips (8 and 9 in squares). The effects of the implantation of beam are less noticeable on the back strips.

3.3.2.2 e11003

Subsequent experiments (e11003) utilized the following procedures for energy calibration. Energies were extracted from offline pulse-shape analysis, utilizing the pulse height algorithm described in Section 3.3.1. The energies observed in two adjacent strips are plotted against one another in Fig. 3.8 to illustrate cross-talk effects produced within the detector, which arises from the electronic coupling between strips and is independent of energy extraction method [57]. With a signal in strip i, a pulse proportional in energy appears in strips i+1 and i-1, as shown in Fig. 3.9, where gating around the 662-keV γ ray from a ^{137}Cs source revealed the cross-talk peaks in the two adjacent strips. Cross-talk manifests as a constant fraction of the energy in the adjacent strip, which is the case for the regions labeled as cross-talk in Fig.3.9. If these effects were the result of charge sharing, which occurs when the charge cloud of a particle overlaps with multiple strips in the detector, the amount of energy within the adjacent strip would not be a constant fraction, and would change depending upon the location of the particle within the detector. Additionally, if the signal arising from a γ ray from a calibration source is calibrated, the calorimeter spectrum (energy spectrum summing all the deposits within all strips together) of the GeDSSD will result in peaks at slightly higher energies than the energy expected from calibration if there is cross-talk within the detector [57]. The effects of cross-talk were corrected by gating on the full energy 662-keV γ ray and determining the pulse height in the neighboring strip for each pair of strips. This one point correction was used to correct the recorded energies by iteratively subtracting the fraction of the full pulse height from both neighboring strips for each strip recording an energy in the event. The multiplicity (before and after cross-talk correction) of back strips gated on the 662-keV peak from the ^{137}Cs source is given in Fig. 3.10, where multiplicity is the number of strips with an energy above threshold within a single event.

After cross-talk correction, the strips were calibrated using several γ rays: the 59.5-keV γ ray from ^{241}Am, the 662-keV γ ray from ^{137}Cs, the 1173-keV and 11332-keV γ rays from a ^{60}Co source and several additional background γ rays (^{40}K: 1460 keV, ^{208}Tl: 1592-keV escape peak

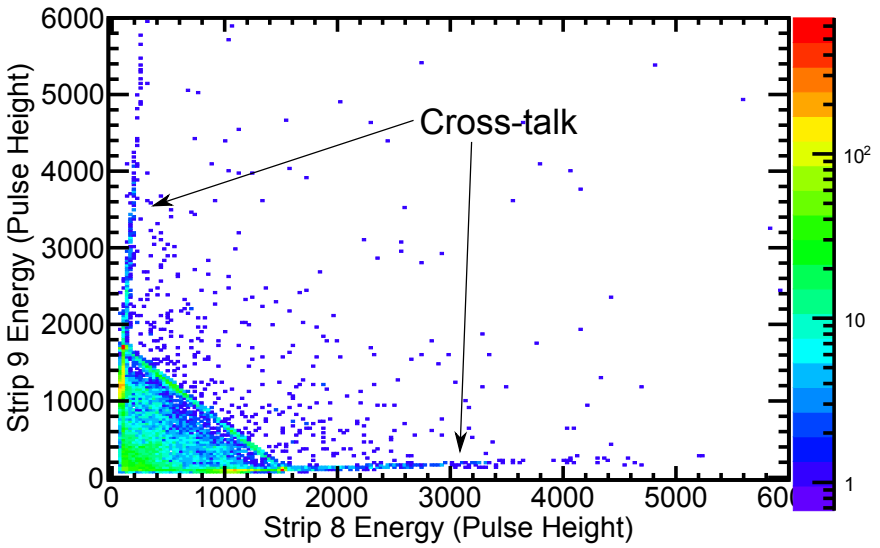

Figure 3.8 The uncalibrated energies of two adjacent strips for multiplicity 3 events from a ^{137}Cs source on the back side of the detector. The effects of cross-talk appear in the regions on the edge of the figure.

from 2615 keV) visible in the GeDSSD spectrum during a week of recording data (Fig. 3.11). No drift in the peak positions was observed as a function of time.

With the 1-D calibration, it was apparent that the calibration for a single strip on one side of the detector was dependent upon the position of the event in the opposite set of strips, as shown in Fig. 3.12. This effect was seen across strips on both sides of the detector, indicating that both the front and the back of the GeDSSD required a two dimensional (2-D) energy calibration. A 2-D calibration takes the position in both sets of strips, defining a pixel, as the position to calibrate by.

$$E(keV) = slope_{back}[strip_{back}][strip_{front}] * E(ADCunits) + intercept_{back}[strip_{back}][strip_{front}] \tag{3.7}$$

$$E(keV) = slope_{front}[strip_{back}][strip_{front}] * E(ADCunits) + intercept_{front}[strip_{back}][strip_{front}] \tag{3.8}$$

When calibrating the back strips, the position of the event on the front was taken as the strip centroid (and vice-versa). For example, if the back strips registered energies above threshold in strips 7 and 8, if the front strip centroid was in strip 9, then the two calibrated pixels would be 7, 9, and 8, 9. The need for a 2-D energy calibration arose from the radiation damage within the detector, as a result of charge trapping.

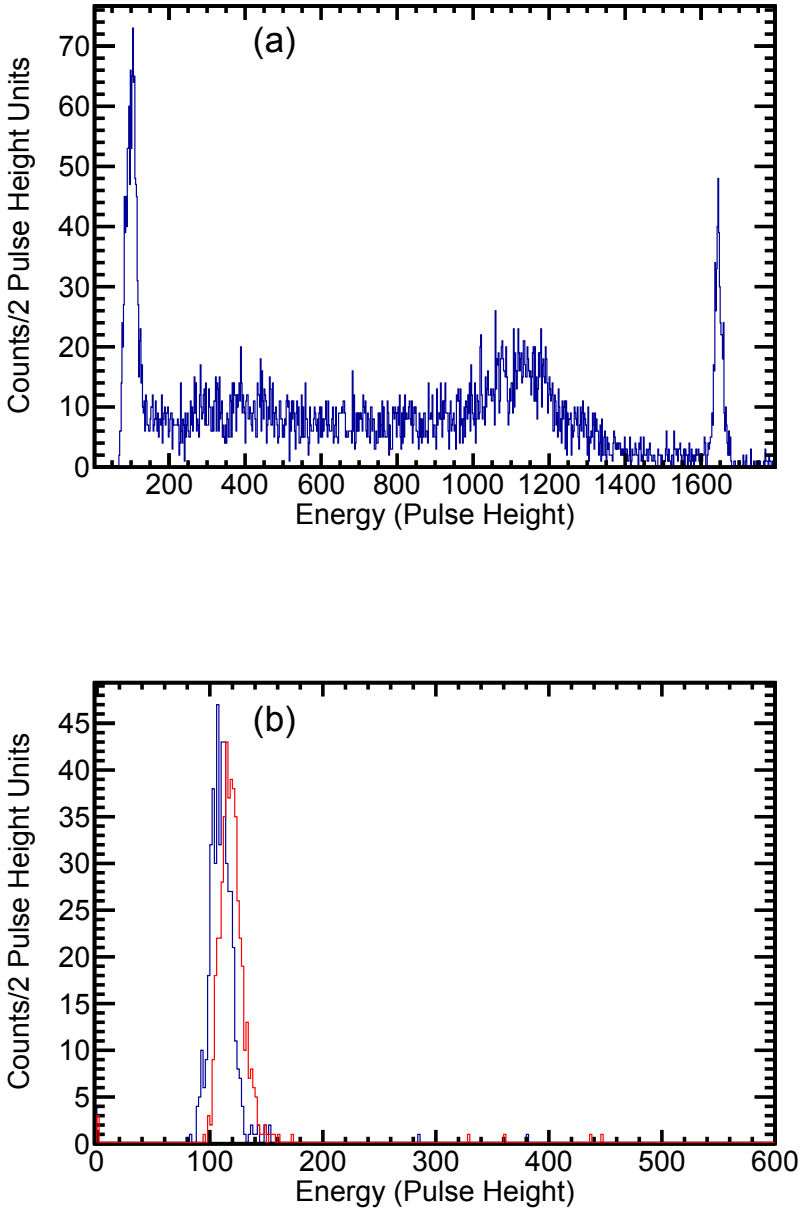

Figure 3.9 (a) The raw energy histogram for multiplicity 3 events for front strip 5. Gating around the peak at 1650 ADC units, corresponding to the full ^{137}Cs energy deposition, (b) the effects of cross talk can been seen in the neighboring strips, strip 6 shown in blue and strip 4 in red.

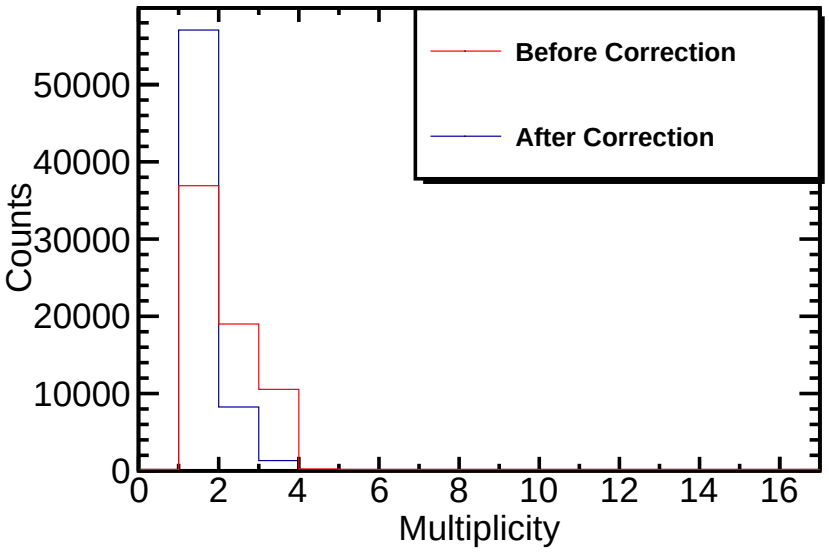

Figure 3.10 Multiplicity of the back high-gain strips gated on the 662-keV γ ray from ^{137}Cs. In red is the multiplicity before cross-talk correction, and in blue is the multiplicity after cross-talk correction.

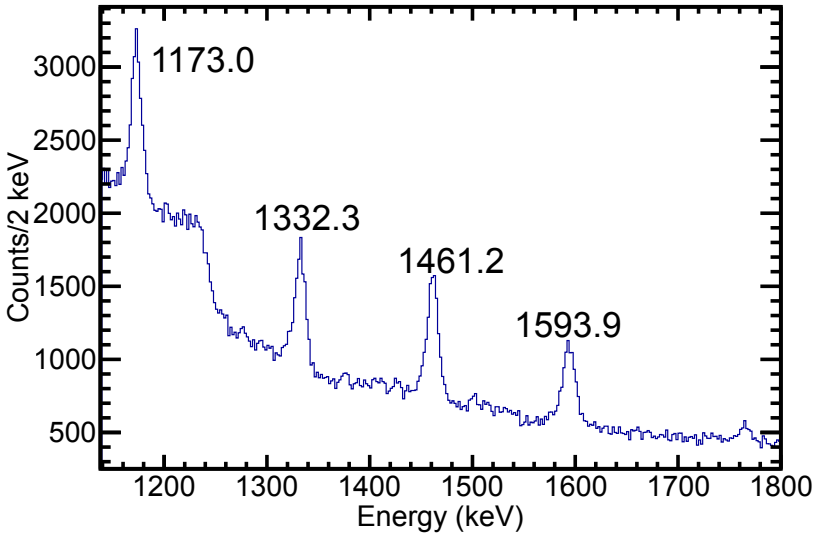

Figure 3.11 Calibrated strip energy spectrum for all back strips on the detector showing the higher energy calibration peaks.

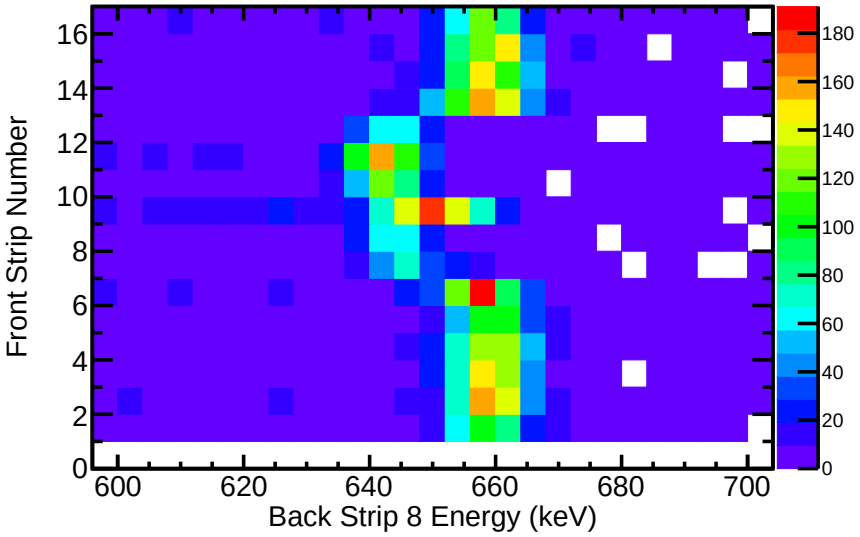

Figure 3.12 Dependence of back strip 8 cross-talk corrected, energy calibrated ^{137}Cs spectrum on the coincident front strip. The figure is zoomed in around the 662-keV transition.

The 2-D calibration was determined pixel by pixel (where a pixel is defined as the intersection of the strips on both side of the detector) with a linear calibration based upon the 662-keV ^{137}Cs and 59-keV ^{241}Am peaks. Each pixel position had two calibrations; one for the back strip and one for the front strip. The two calibrations (1-D and 2-D) are compared in Fig. 3.13 for the same strip shown in Fig. 3.12. Thus, compared to the commissioning runs, the calibration technique for the high-gain strips had to shift from a one dimensional, linear energy calibration to a multi-step calibration, consisting of cross-talk correction, followed by 1-D calibration, and finally the 2-D calibration.

The ^{137}Cs and ^{241}Am calibration data was taken for 3 hours after the end of the beam time, waiting until each strip on both sides had several hundred counts within the 662-keV peak in order to check the calibration and condition of the GeDSSD after being exposed to more beam. Since the pixels at the very edge of the detector had a limited number of counts, this necessitated the use of a 1-D strip calibration before the 2-D pixel calibration to insure that no pixels were left uncalibrated. The resulting resolutions from this approach are displayed in Fig. 3.14. In comparison to Fig. 3.6, for the same strips (1 and 9 on the front), the resolution from the 2-D calibration using the pulse

height energy extraction algorithm was similar to that from the 1-D calibration using the Pixie energies for strip 9 in the middle of the detector (∼17 keV from the PIXIE energies vs.∼15 keV for the pulse height energies). As the strip on the edge (1) was exposed to beam, its resolution was poorer in Fig. 3.14 compared to that of the earlier experiments, in which the strip was not yet exposed to any beam. This would suggest that most of the resolution degradation occurred after the first beam exposure, with less degradation upon further bombardment, which is evidenced in Fig. 3.6 where the middle of the detector's resolution remains roughly constant after some ions implanted.

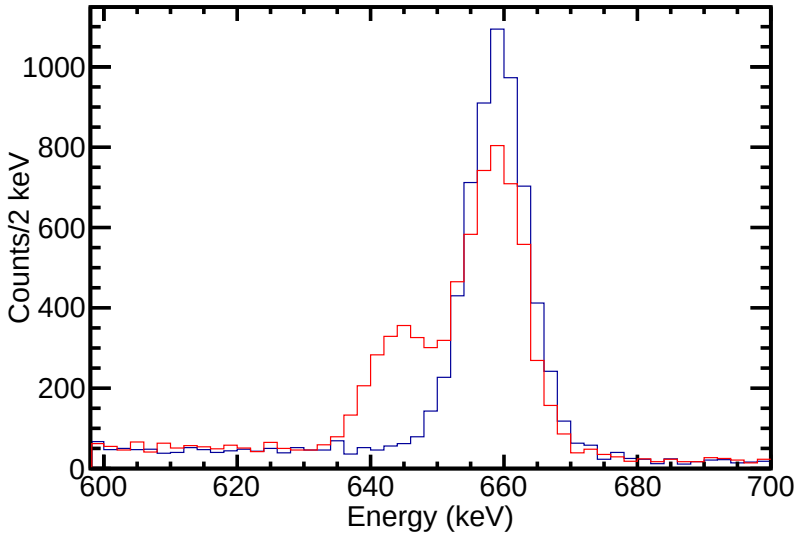

Figure 3.13 Calibrated back strip 8 energy spectrum comparing the 1-D calibration (red) to the 2-D calibration (blue).

3.3.2.3 Re-analysis of e11503

The techniques developed in later experiments were used to re-analyze the resolutions and calibration from the earliest datasets. Some resolution can be recovered by pulse processing and correcting for the effects within the GeDSSD investigated during e11003. The source data taken after the first experiment, e11503, was re-investigated to determine if improvements could be made to the resolution after beam deposition into the detector. Moving from PIXIE energies to pulse process-

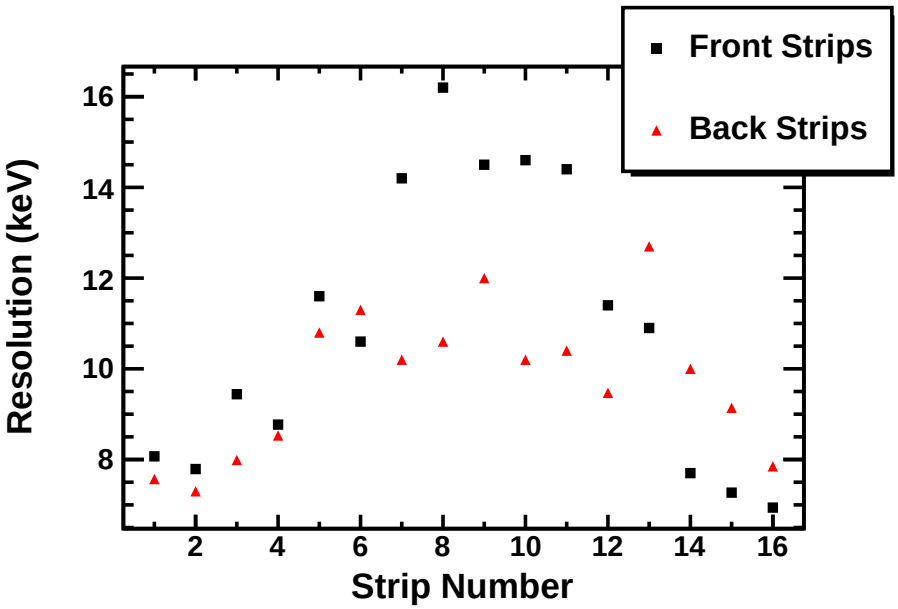

Figure 3.14 Resolution in keV of individual strips after calibration the pixels of the detector with a ^{137}Cs source after experiment e11003.

ing for the energy determination, with no other analysis, an improvement in resolution was seen across strips (Fig. 3.15). After 1-D calibration (with the pulse height energy determination), the back strip energy vs. front strip number for the same strip (strip 8) as Fig. 3.12 is shown in an analogous histogram in Fig. 3.16. The dependence upon 2-D position is much less than that for data taken from later experiments, due to less damage.

Comparing the data for strips shown in Fig. 3.7, the pulse height analysis for a ^{137}Cs source after e11003 (Fig. 3.14) yielded resolutions of 12 keV in strip 9 and 7 keV in strip 2, whereas the resolutions shown in Fig. 3.15 are similar (9 keV in strip 9 and 8 keV in strip 2). The PIXIE resolutions in Fig. 3.7 also compare favorably to those in Fig. 3.15. The resolutions of back strips 2 and 9 are summarized in Table 3.1. For the two experiments, different PIXIE modules were used (100 MSPS for e11503 and 250 MSPS for e11003), and as a result, the PIXIE trapezoidal filter parameters were not the same.

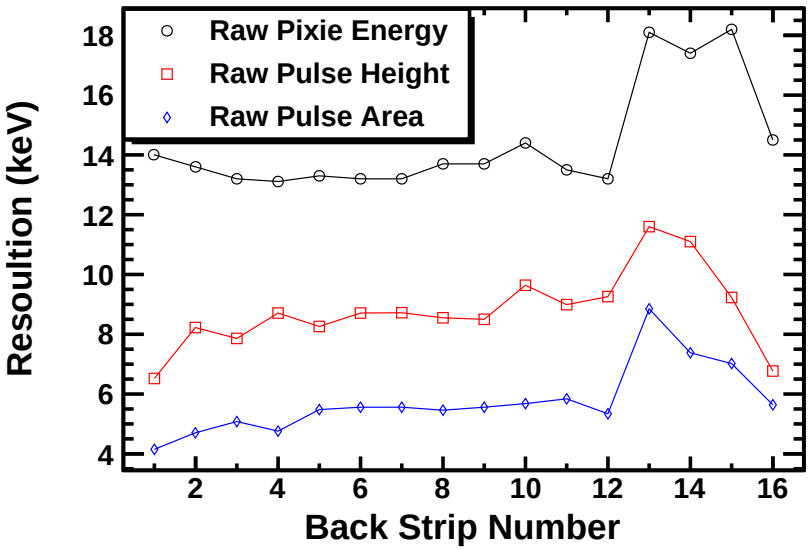

Figure 3.15 Resolution of back strips from raw (non-calibrated or cross-talk corrected) energy spectra comparing energies calculated by the PIXIE trapezoidal filter (black circles), pulse height algorithm (red squares), and pulse area algorithm (blue diamonds) for the 662-keV peak from a ^{137}Cs source. These data were taken immediately after experiment e11503.

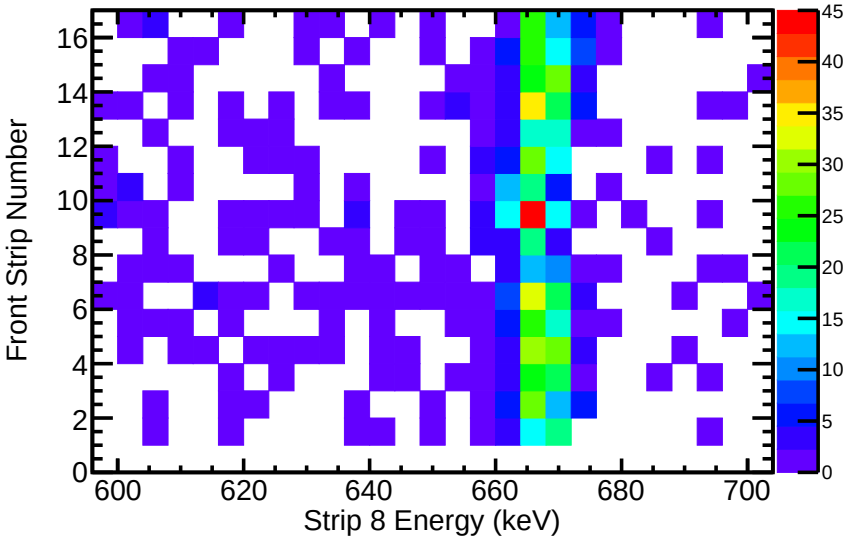

Figure 3.16 Front strip location vs. back strip energy calibration for the re-analyzed data after e11503 for the ^{137}Cs source at 662-keV. A much smaller variation within calibration as a function of strip location on the other side is seen compared with the later data.

Table 3.1 Resolutions of strips 9 and 2 on the back side of the detector on the figures shown in this section.

Strip	Figure	Energy Extraction	Resolution
9	3.7	PIXIE	5.48-15.8
	3.14	Pulse Height	12.0
	3.15	PIXIE	13.7
		Pulse Height	8.50
		Pulse Area	5.56
2	3.7	PIXIE	5.00-14.7
	3.14	Pulse Height	7.30
	3.15	PIXIE	13.6
		Pulse Height	8.22
		Pulse Area	4.69

3.3.3 Low-gain energy calibration

3.3.3.1 Commissioning runs e11503 and e09055

The first commissioning run (e11503) used a 130 Mev/A ^{76}Ge beam with a 423 mg/cm^2 Be target, with a 0.5% momentum acceptance in the A1900 spectrometer [41]. This beam was fragmented to produce Mn, Fe, Co and Ni isotopes with A$\sim$68 and was centered on transmitting ^{67}Fe. For more experimental details, please see Section 3.4.2.2. In the first commissioning experiments, the low-gain (or implant) signals were simply gain-matched based upon the PIXIE energy extraction. The strip energy was calibrated based on the energy deposition of ^{67m}Fe [58]. The subsequent γ-ray emission from ^{67m}Fe at 367 keV ($t_{1/2}$=0.730(31) ms) provided a clean tag for ^{67}Fe ions. The energy pulses were gain matched according to the following equation:

$$E(MeV) = \frac{LISE(MeV)}{E_{implant}(ADCunits)}[strip] \times E(ADCunits) \tag{3.9}$$

where $LISE(MeV)$ is the LISE [59] prediction of the amount of deposited energy by a ^{67}Fe ion, $E_{implant}$ is the amount of energy in ADC units deposited by an ^{67}Fe ion in a given strip and E is the current energy deposition being calibrated. For the strips with the most beam intensity in the middle of the detector, Fig. 3.17 shows the calibration to demonstrate the effects of gain matching.

The structures in the energy spectrum were the result of different ions depositing different energies in the detector.

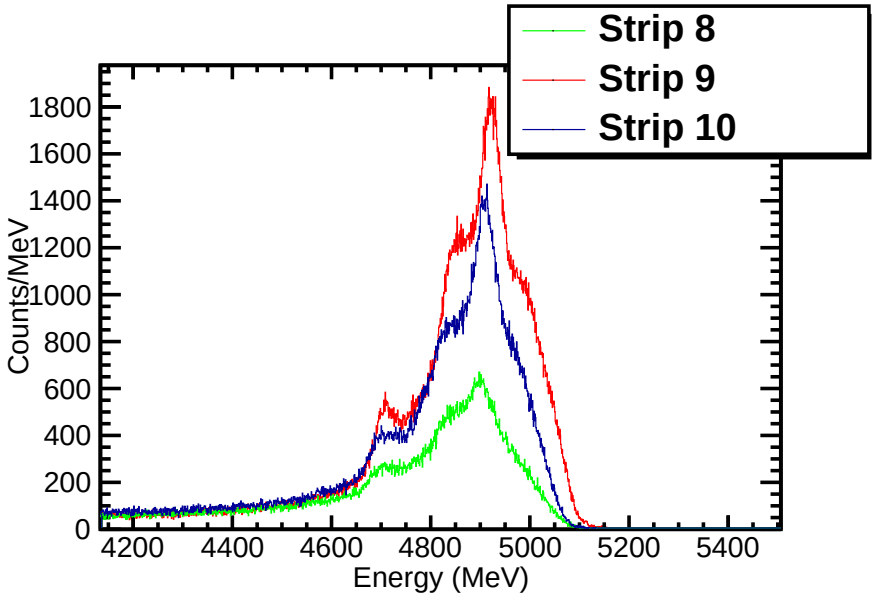

Figure 3.17 Calibration of the low-gain strips utilizing the gain matching to the LISE predicted energies technique. Shown in green, red and blue are shown the events for strips 8, 9, and 10, respectively.

3.3.3.2 e11003

In e11003, the calibration of the front low-gain electronics followed a similar pattern to that of the high-gain strips, calibrating the energy with a ^{124}Sn beam based upon LISE energy calculations. On the back side of the detector, the preamplifiers saturated and thus those strips were simply gain matched, as the location in ADC units for the saturated strips was a little different for different strips (making the peaks from the ion deposition slightly different between strips, necessitating the gain matching), using the PIXIE energies in lieu of pulse processing. An example of a saturated pulse is shown in Fig. 3.18. Many ion events saturated more than one strip on the back side of the detector. Therefore, the strips on the back side of the detector were used to determine the position of the event by an energy weighted average of the strip number, but were not used for an energy calculation. The distribution of strips on the back side tended to be symmetrical, with a

few (typically 1-3) saturated strips at the middle of the detector and a strip on either side of that distribution from electronic cross-talk. The energy deposited by the ions was greater in e11503 than that in the other two experiments.

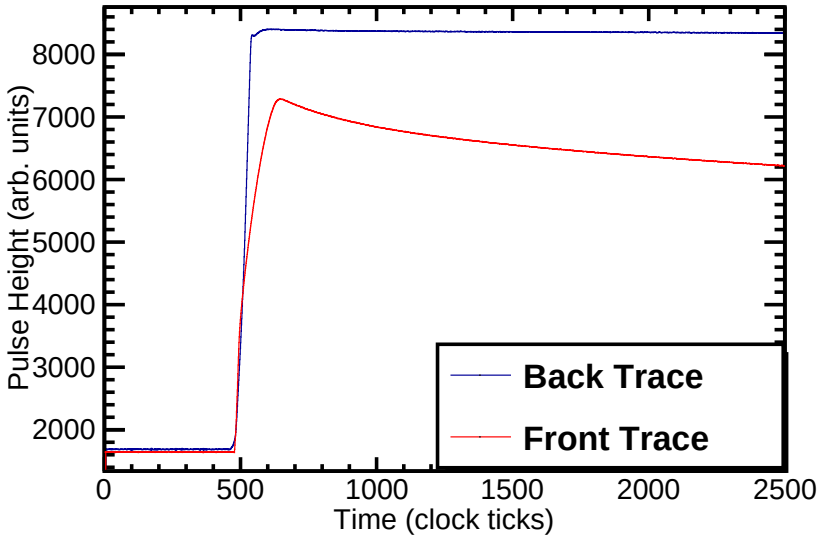

Figure 3.18 An example trace from the back of the GeDSSD (blue), illustrating the preamplifier saturation. The maximum amplitude is 16384, whereas the low-gain back strips reach a maximum well before the maximum of the ADC range. For comparison, a trace from the front of the GeDSSD is shown (red).

On the front strips, cross-talk calibration was completed using the same techniques as with the high-gain electronics. A $^{124}Sn^{50+}$ beam was utilized for this purpose. The two dimensional plot of energies of two adjacent strips is shown in Fig. 3.19. Analogous to Fig. 3.8, depicting the high-gain strips, the effects of cross-talk can be seen in the regions on the sides of the figure. Charge sharing is observed in the center of the spectrum and occurs when the charge cloud created by a particle overlaps with the gap between adjacent strips [60]. Energy from the particle is deposited into both strips. This is distinct from two particles depositing their energies individually into two adjacent strips. While not implemented in this analysis, one could consider summing charge sharing events to recreate a single energy deposition. In comparison to Fig. 3.8, the charge sharing region in Fig. 3.19 had discontinuities instead of being straight across. One possible explanation lies in the difference in energy loss between the heavy particles and γ rays. The energy loss across the crystal

is lower for γ rays, and the particles can penetrate through the entire thickness. The heavy ions stop a very small distance into the crystal, losing a large amount of energy. The connections of the electrodes to the crystal make up a greater proportion of a particle's path for the heavy ions, and therefore there are energy losses. In the charge-sharing region, some of the charge cloud overlaps with the gap between adjacent strips, and there is less energy loss.

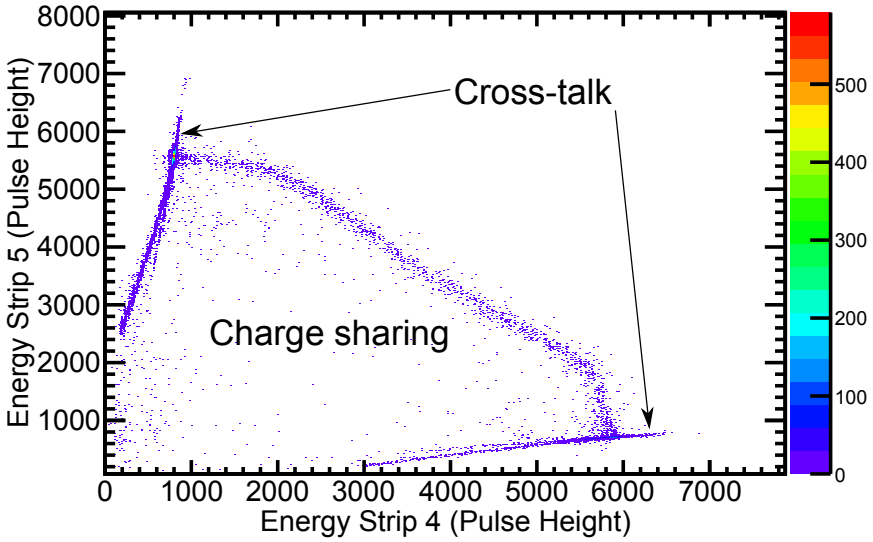

Figure 3.19 A 2-D plot of neighboring strips showing cross-talk and charge sharing.

The subsequent one and two dimensional energy calibrations were carried out in the same procedure as their high-gain counterparts. In Fig. 3.20, the one dimensional energy calibration of strip 4 on the front of the detector is shown as a function of the location in the back strips. Like the high-gain electronics, the calibration depends upon the 2-D location within the detector. In Fig. 3.21, the difference between the 1-D and 2-D calibration is shown.

While the above techniques work well for the side strips, which have seen less ion deposition, the middle strips became significantly damaged and the calibration was more difficult. In the middle of the GeDSSD, the full-energy deposition peak is not clear and so calibrations were made based upon events that had multiplicity 1 after cross-talk correction, which were assumed to consist of the full-energy-deposition peak and cross-talk peaks in strips on one or both sides. Higher multiplicity event used the multiplicity 1 calibration, and were not thrown away. The calibrated

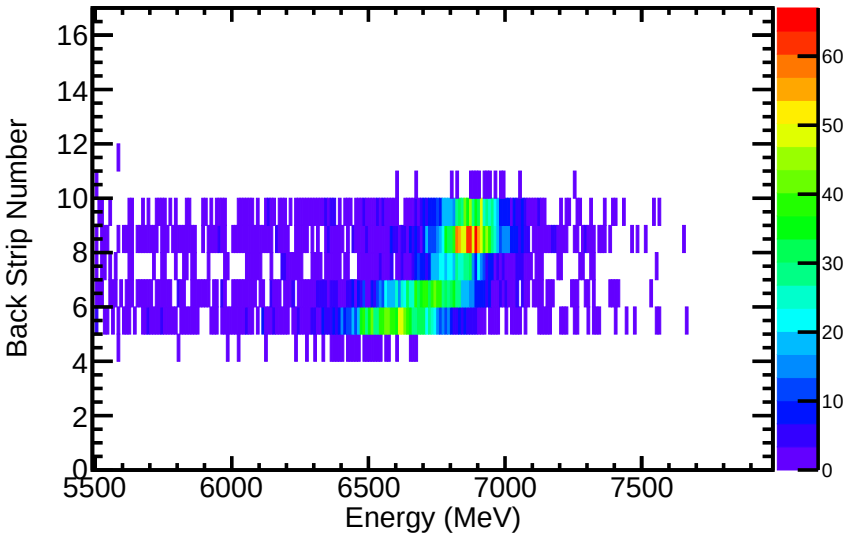

Figure 3.20 Back strip location as a function of energy in front strip 4 showing the dependence in calibration on location in detector.

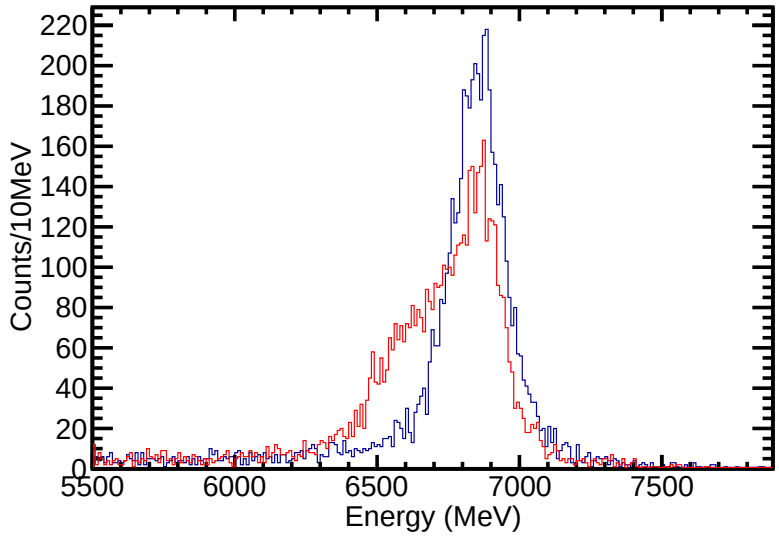

Figure 3.21 A comparison of recorded energy deposition from the $^{124}Sn^{50+}$ beam between the 1-D calibration (red) to the subsequent 2-D calibration (blue) for front strip 4.

spectrum for a strip 7 is shown in Fig. 3.22 in blue, while the multiplicity 1 after cross-talk events are overlaid in red. Higher multiplicities do not have apparent peaks, as is shown in Fig. 3.23. The multiplicity distribution before and after cross-talk correction for all front low-gain events is displayed in Fig. 3.24. The 2-D histogram of the energy in adjacent strips 8 and 9 in the beam implantation profile is given in Fig. 3.25. The regions on the sides of the plot resulting from cross-talk between strips are still relatively clear but the center of the plot where charge-sharing would be expected is not as clear as that seen in the edge strips of the detector (Fig. 3.25). Another way to visualize this effect is to compare the results for the fully-stripped Sn ions before and after the beam time. In Fig. 3.26, a peak is visible in the data at the start of the beam time but not at the end.

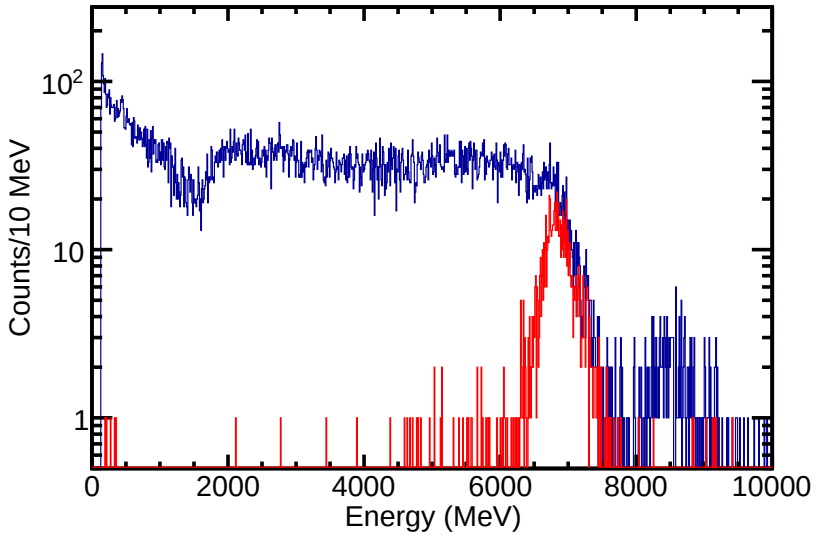

Figure 3.22 The calibrated energy for a strip in the middle of the detector, strip 7. All multiplicities (blue) and multiplicity 1 after cross-talk correction (red).

Finally, there was also a gain-matching applied for the later two settings (centered on Ru and Nb isotopes, see Chapter 4) to account for any small shifts in calibration during the beam time. This was done for two reasons: to try to improve the resolution as much as possible, and because the calibration for the ^{124}Sn beam was slightly different for data taken at the start of the experiment and the end. The calibration was completed using the ^{124}Sn beam at the end of the experiment

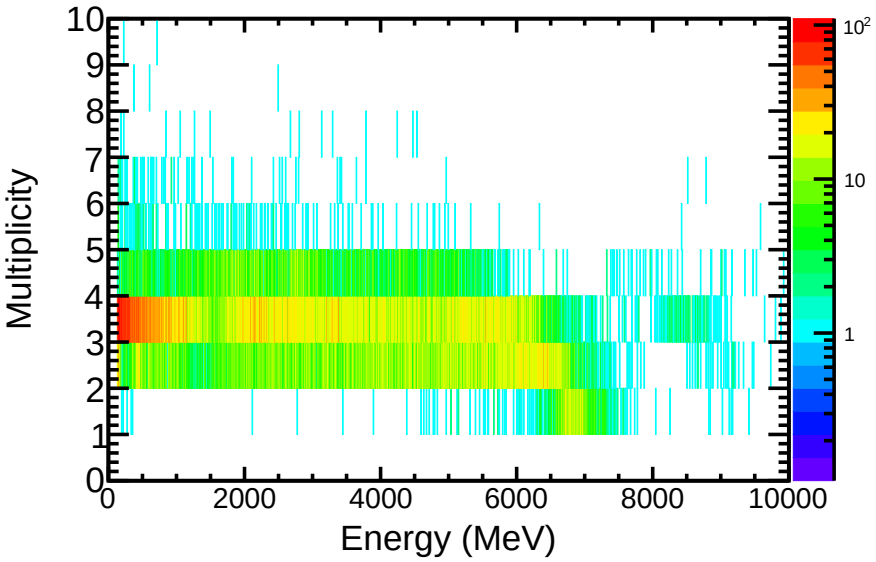

Figure 3.23 The multiplicity distribution as a function of the energy of strip 7.

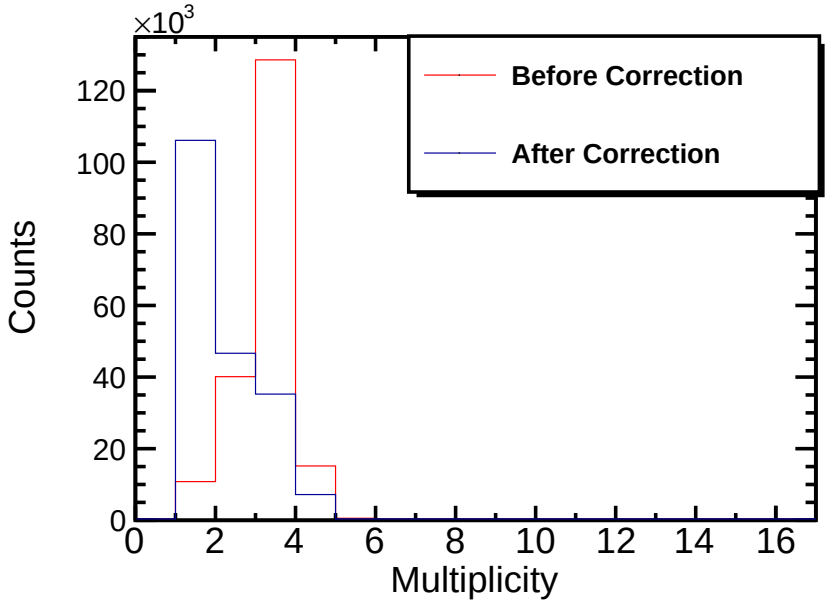

Figure 3.24 The multiplicity distributions of front low-gain events in e11003, before cross-talk correction (red) and after cross-talk correction (blue).

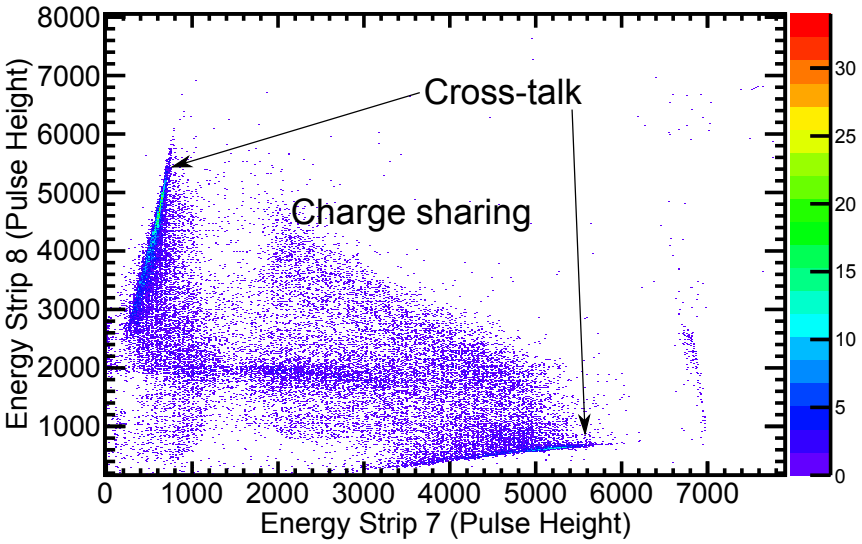

Figure 3.25 A 2-D distribution of the energy observed in two neighboring strips in the middle of the detector.

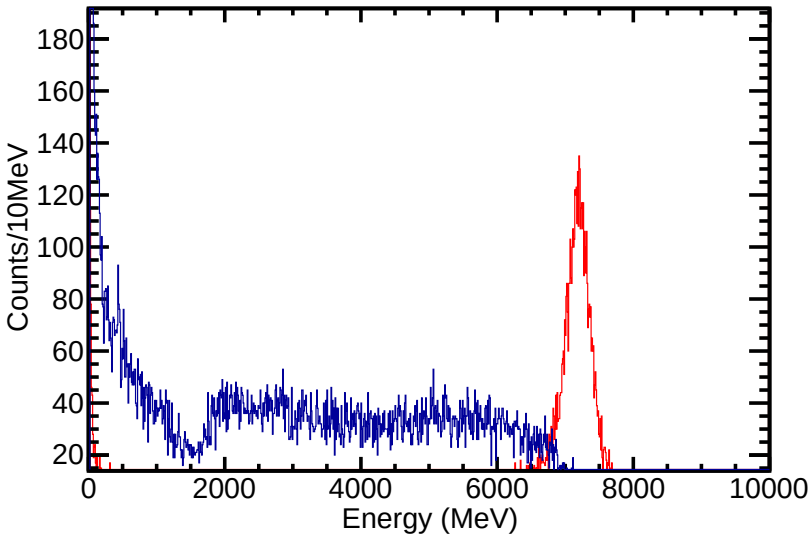

Figure 3.26 A comparison of low-gain strip 7 in the ^{124}Sn fully-stripped beam before (red) and after (blue) the duration of the beam time. The full-energy deposition is not clear in the data after the rest of the experiment.

and used for the preceding week's beam time. For two-thirds of the strips, the shift in calibration, relative to the average value, was less than 2% (with energies on the order of 5.5 GeV). Fig. 3.27 illustrates the degree of this gain shift for each of the strips on the front, for both of the beams that followed the ^{124}Sn beam (see Chapter 4 for more details on the experiment). This shift was corrected as a function of time.

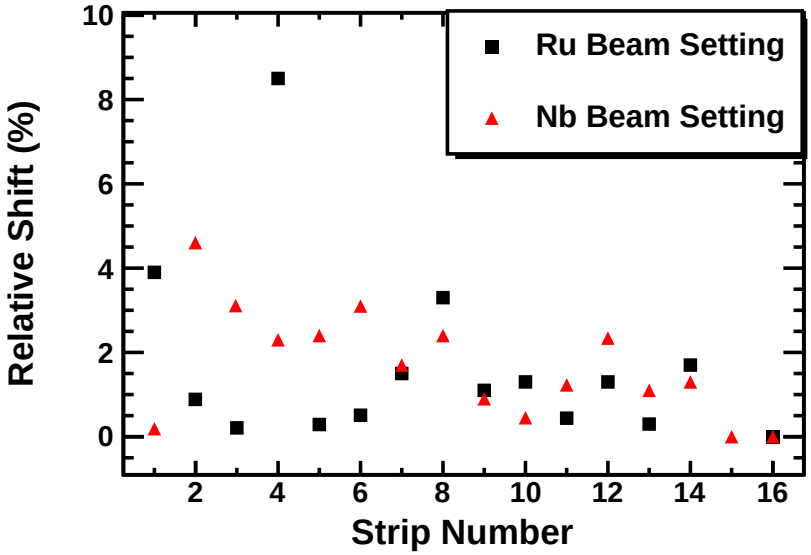

Figure 3.27 Relative shift (compared to the average value across all strips) in the energy calibration as a function of strip number, shown for the two later beam settings in e11003.

As previously mentioned, the GeDSSD sustained damage due to the implantation of heavy ions. This effect manifested in a variety of different ways: a degradation of resolution, the need for a 2-D calibration, and the loss of an observed full-energy peak in the middle of the low-gain strips. While the degradation in resolution occurred immediately, the other effects worsened over time. The effects of neutron damaged within segmented, planar Ge detectors has been previously studied [61]. For neutron damage, the crystal lattice of the crystal becomes disordered, which results in vacancies in the crystal. The displaced atoms create charge trapping, which is greater for the hole collection. This results in the loss of events within the damaged region of the detector, where full energy deposition is not observed. These effects are similar to what was observed after the bombardment of the GeDSSD by heavy ions.

3.4 Efficiencies

Simulations played a large role in quantifying the efficiency of the GeDSSD since a standardized source cannot be placed at the location within the germanium material from which radiation originates, though if an isotope with well-known γ-ray absolute intensities over a range of energies can be produced and delivered to the experimental station, one could measure efficiencies. The detection efficiency was measured using a source external to the GeDSSD's cryostat and was matched with simulation to verify the accuracy of the simulation. Then the simulation was used to obtain the detection efficiency from a location inside the GeDSSD's crystal. Off-line efficiency measurements for a source external to the GeDSSD cryostat with the germanium detectors utilized in the experiments discussed in this document were performed using a NIST calibrated Standard Reference Material (SRM) $^{154\backslash155}$Eu source, SRM 4275C-69.

3.4.1 Absolute γ ray efficiency

The efficiency of the GeDSSD was measured for an SRM source placed 2.4 cm in front of the GeDSSD entrance window. The comparison between simulation and experiment is shown in Fig. 3.28, with simulation matching quite well at energies above 100 keV. The simulation was then used to determine the efficiency of γ rays from an ion location a few millimeters inside the GeDSSD. Ions were expected to stop within a the first few millimeters of the GeDSSD depending upon the ion and the energy of the beam, for example, LISE calculations indicated an expected implantation depth between 1-2 mm into the Ge crystal for the ions in both e11503 and e09055. For e11003, LISE predicted implantation depths between 0.5 and 1 mm. Fig. 3.29 shows the simulated efficiencies for implantation at depths of 1 and 2 mm in the GeDSSD. The GeDSSD is quite efficient for low-energy γ rays but the efficiency quickly drops below 5% at 500 keV.

The efficiencies presented in Fig. 3.29 were simulated for an isolated γ-ray source. The presence of β-decay electrons will reduce the efficiency of γ-ray detection in the GeDSSD as the energy deposition by the β and γ particles within a single strip will sum together. This effect is

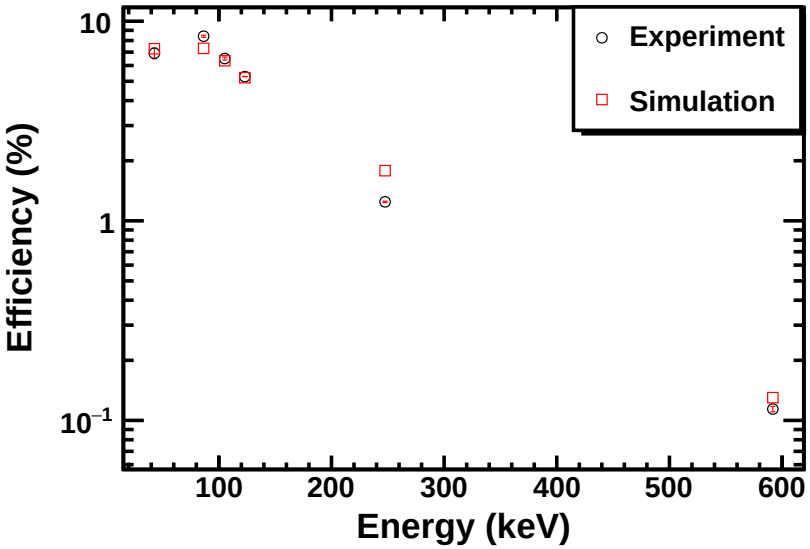

Figure 3.28 Comparison of simulated and experimental efficiencies from a ^{154,155}Eu SRM source located outside of the GeDSSD's cryostat. The figure is reproduced from [6]. The efficiency shown is a peak efficiency. The total number of counts in each peak in the SRM source was determined for each strip individually, and the results from each strip were summed to find the efficiency plotted in the figure.

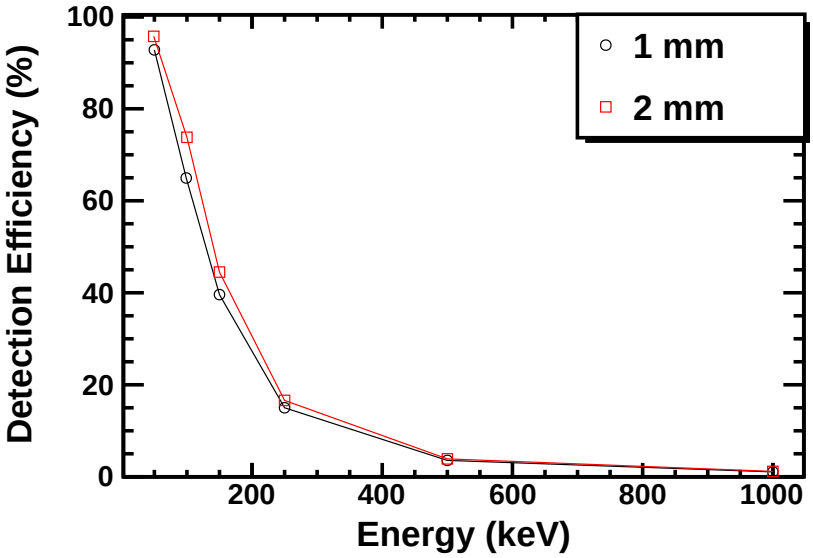

Figure 3.29 γ ray detection efficiency of the GeDSSD. Simulated for two implantation depths. The figure is reproduced from Ref. [6]. The efficiency shown is a peak efficiency. The total number of counts in each simulated energy was determined for each strip individually, and the results from each strip were summed to find the efficiency plotted in the figure.

discussed in more detail in Section 3.6.

3.4.2 Electron efficiency

Another important consideration is the efficiency for discrete electron transitions, analogous to the detection of an isolated γ ray. This efficiency is necessary for conversion electron spectroscopy following isomeric decays. A related efficiency is the electron correlation efficiency, which is the percentage of β-decay electrons not only detected, but successfully correlated (or matched) to the preceding ion that emitted it. The electron correlation efficiency depends upon overall implantation rate, the electron efficiency, and decay half-life.

3.4.2.1 Electron detection efficiency

The GeDSSD should be highly efficient for detecting electrons, making it an ideal conversion electron detector. For electrons with energies less than 500 keV, the GeDSSD is nearly 100% efficient. As the energy of the electron increases, so does the range of the electron and the absolute efficiency for detecting the full energy of the electron decreases. For 1 mm and 2 mm implantation depths, the calculated efficiency for detecting the energy of low-energy electrons in the same strip as the ion is shown in Fig. 3.30. The simulated source of electrons was uniformly distributed across a five by five mm area (the size of a single pixel) and was placed in the center of a strip at the middle of the detector. The source was assumed to emit electrons isotropically. The observed drop in efficiency at higher energies was due to the electron traveling beyond a single strip, depositing energy into multiple strips or from electrons escaping from the face of the GeDSSD. Greater implantation depths increases the efficiency at higher energies, due to fewer electrons escaping out of the face of the detector, to a point. The efficiency as a function of depth into the GeDSSD for 3000 keV electrons is summarized in Table 3.2. Near the middle of the detector, the efficiency is less dependent upon the depth, as the electrons have penetrated far enough inside to limit their escape out of the GeDSSD.

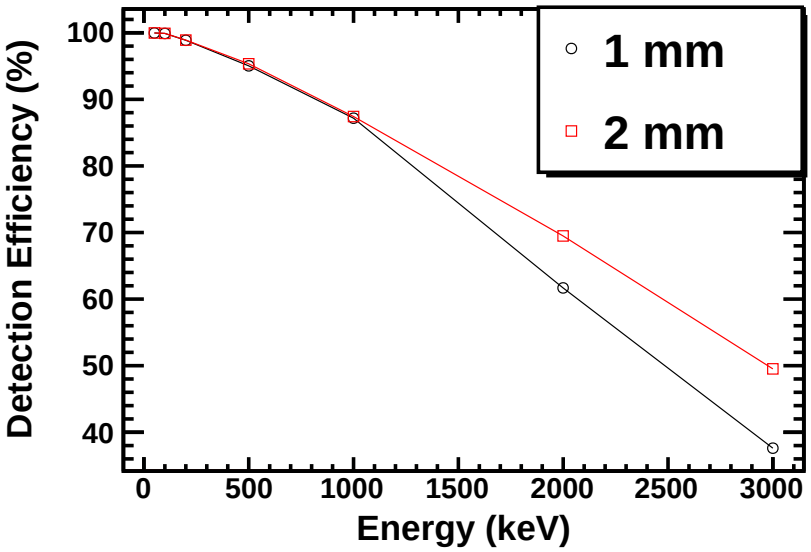

Figure 3.30 Efficiency for detecting low-energy electrons for implants located at 1 mm (black) and 2 mm (red) from the front face of the GeDSSD. The efficiency was determined by the number of counts within the peak at the full energy of the simulated electrons for the strip in which electron originated.

Table 3.2 Electron detection efficiency as a function of depth into the GeDSSD for 3000 keV electrons. The efficiency was determined by the number of counts within the peak at the full energy of the simulated electrons for the strip in which electron originated.

Depth (mm)	Efficiency (%)	Uncertainty (%)
1	49.6	0.3
2	65.5	0.4
3	68.9	0.4
5	69.4	0.4

3.4.2.2 β-decay electron correlation efficiency

In order to determine the GeDSSD's electron correlation efficiency, ^{54}Ni ions produced during experiment e09055 were studied. The second commissioning experiment (e09055) used a 160 Mev/A ^{58}Ni beam with a 520 mg/cm^2 Be wedge. Here the momentum acceptance of the A1900 was 1%, to produce ^{54}Ni and ^{55}Cu. The ions were produced, separated, and transmitted to the experimental area. The ions passed through two PIN detectors (303 and 488 μm thick) to measure their energy loss and TOF relative to the A1900. The ions then passed through a thin Kapton window at the end of the beam pipe and a few mm of air before going through the GeDSSD cryostat and stopping a few mm into the crystal. The GeDSSD was surrounded with the Segmented Germanium Array, or SeGA [50], to detect β-delayed γ-rays. SeGA was arranged in two rings of eight detectors, one upstream of the GeDSSD position and one downstream. The configuration was similar to the standard β-SeGA layout [62], but with a 11.6 cm spacer between the two halves of SeGA to accommodate the increased width of the GeDSSD compared to smaller Si DSSD setups. Photographs of the experimental setup are shown in Fig. 3.31 and Fig. 3.32.

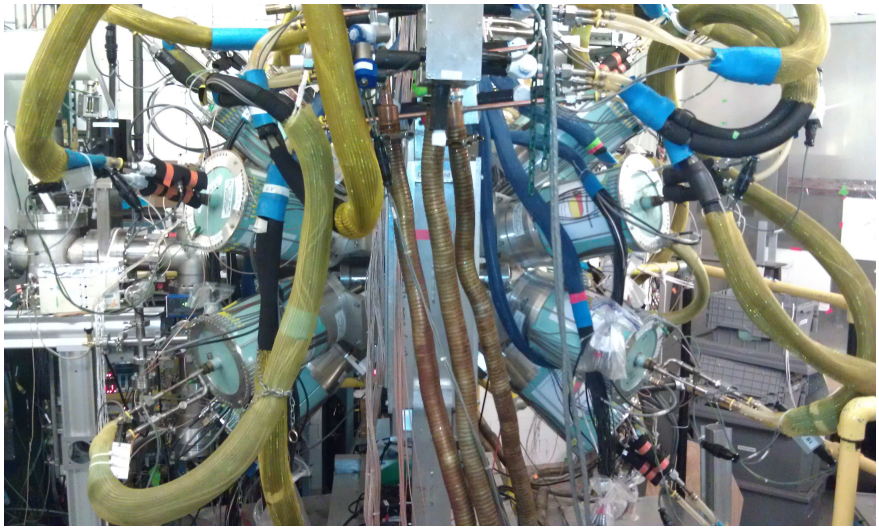

Figure 3.31 A photograph of the GeDSSD and SeGA configuration used for experiments e11503 and e09055 viewed from the side. The beam travels left to right in the image.

Electron correlation efficiency is one way to compare the increased performance of the GeDSSD to its more traditional Si counterparts. Depending upon the ions' half-lives and the experimental

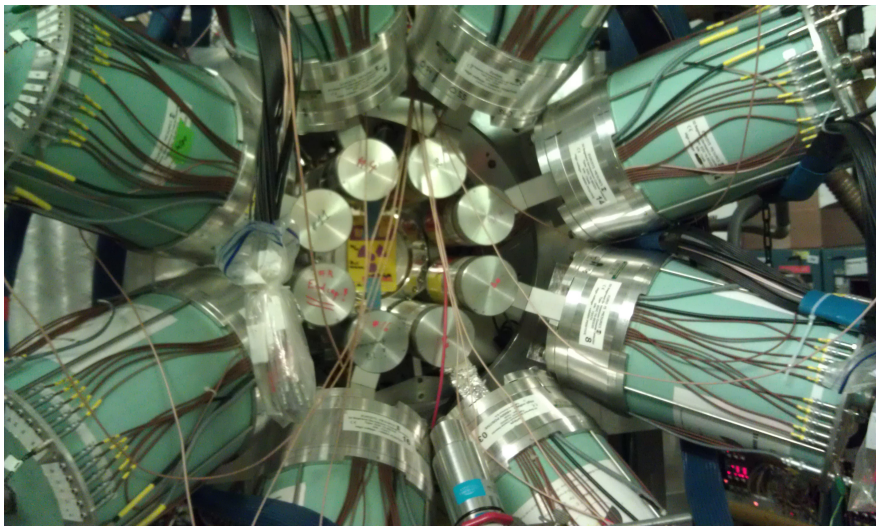

Figure 3.32 A photograph of the GeDSSD and SeGA configuration used for experiments e11503 and e09055. The beam exists the page toward the viewer.

implantation rate, Si-based systems exhibit a correlation efficiency of 30-40% [6, 42]. Given the high implantation rate relative to the ions' half-lives in experiment e09055, correlations were made allowing only decays in the same pixel as the implant to be correlated. A wider correlation field was not used due to the increase in random correlations.

Fig. 3.33 shows the β-decay half-life curve for the ^{54}Ni ions, where a half-life of 97(2) ms was extracted using the Bateman equations. The parameters within the fit that were varied were the parent decay constant, the activity of the parent, and the constant background. The decay constant of the daughter nucleus was input into the fit, but kept as a constant. The half-life of ^{54}Ni was extracted from the parent decay constant of the fit. The fit was performed using a chi-square method. Previous results report 106(12) ms [63] and 103(9) ms [64] for the half-life. The maximum correlation time was chosen to be 500 ms, which is roughly 5 half-lives. The decay curve was fitted with the Bateman equations for radioactive decay, where the contributions from the parent ^{54}Ni nuclei, the daughter ^{54}Co nuclei ($t_{1/2}$=193.23 ms [63]), and a constant background are also shown. The number of ^{54}Ni decays was extracted and compared to the total number of implanted ions to give an electron correlation efficiency of 55(2)%. Simulating this decay, an electron correlation efficiency of 61.6(6)% was predicted for same-pixel correlations. While the

experimental data did not allow for an expansion into a wider correlation field, simulation predicted a 87.0(7)% efficiency for an expanded correlation field.

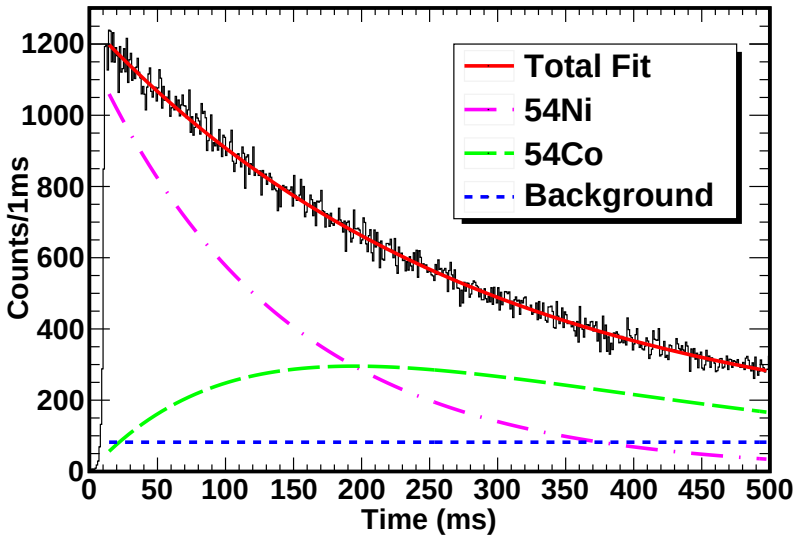

Figure 3.33 Decay curve of ^{54}Ni and the fit with the Bateman equations, which was used to determine the electron correlation efficiency. The decay of the ^{54}Ni parent is shown in pink, the growth and decay of the ^{54}Co daughter is shown in green, and the contribution from the background is shown in blue. The figure is reproduced from [6].

The difference between simulation and experiment arises from the details of the simulation. The original simulation was completed using a point source of electrons at the center of a pixel. For a distributed source of electrons across a pixel, the number of events where the electron and ion would be found in the same pixel drops by 10%.

3.5 β-decay spectroscopy techniques

3.5.1 Triggering

There are several triggering schemes that may be used with the GeDSSD: free running, external validation (front-back coincidence), and force recording for all channels. In the free running scheme, each channel triggers independently and records its data to the internal memory buffer of

the electronics module for event readout and event assembly. In the external validation mode, an external validation signal must arrive in coincidence with a delayed copy of the channel's internal trigger. This mode is used to select events where both a front and back signal are present from the GeDSSD allowing localization to a single pixel. The trigger is created from a logical OR signal of the 16 front strips on the detector with a logical AND to the OR of the 16 back strips. The AND signal is fed back into the modules as the external trigger. Finally, the system may also be run with an external trigger forcing all channels in a module to record data whenever the external trigger is applied, regardless of whether an individual channel has observed a signal over threshold or not. Not unexpectedly, this third mode results in a large amount of data. The forced trigger mode can be helpful for aligning the start of traces in time. All experiments discussed in the present work used the second, front-back coincidence mode for the GeDSSD, while the free-running mode was used for the ancillary γ-ray array.

3.5.2 Event localization

The heavy ions produced by the Coupled Cyclotron Facility (CCF) stopped, or implanted, a few millimeters into the GeDSSD. This event is referred to as an "implant event" and was identified by the presence of signals in the low-gain electronics of the GeDSSD, the PINs, and TOF information. There will also be overflow signals in the high-gain electronics of the GeDSSD. A timing gate between the front and back strips in the detector was also placed upon the event. The charge deposited by the heavy ion travels to either side of the detector on the order of 100 ns for 1 cm of Ge [65], so events with larger timing differences were unphysical. The timing difference (back-front) between signals on the two sides of the detector as a function of front strip energy is plotted Fig. 3.34. Events with energies corresponding to the full ion implant energy were closely grouped at small, positive timing differences. The black gate in Fig. 3.34 is the timing and energy gate placed on the low-gain events. In the figure, the lower energy region corresponds to events with what appeared to be cross-talk peaks in multiplicity 1 events, and also potentially light ions produced by the beam fragmentation.

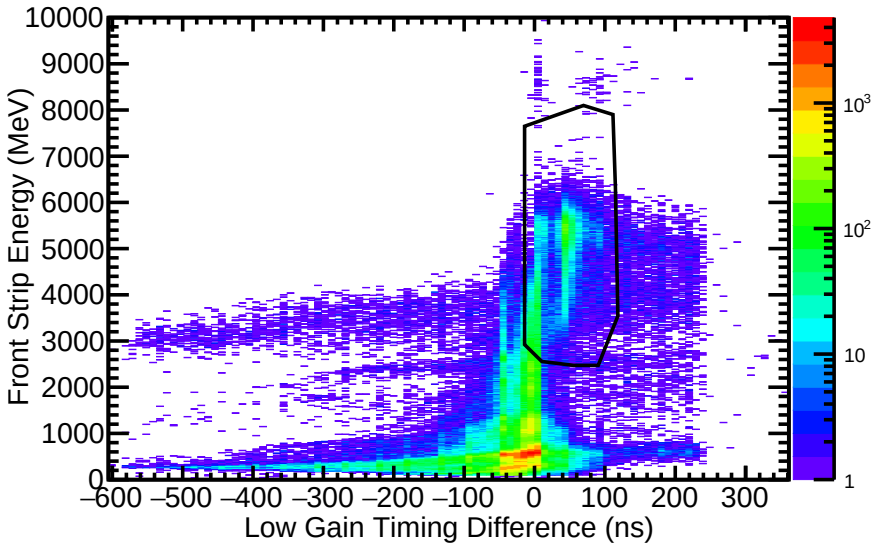

Figure 3.34 Back strip timing minus front strip timing vs. front strip energy (cross-talk corrected and 2-D calibrated) for implant events. The black gate shows the cut placed on the low-gain events. The events shown in the figure do not require a ΔE signal within the PINs.

The radioactive ions implanted into the GeDSSD subsequently β decay. The β-decay electron was detected by the GeDSSD, and β-delayed γ rays were detected by either the GeDSSD or an ancillary Ge array. An event of this type is referred to as a "decay event". A decay event was identified if there is no energy deposited into the PINs or low-gain signals of the GeDSSD, and there must be a signal above threshold on both sides of the GeDSSD in the high-gain electronics. As with the implant events, a timing gate was placed on the difference in time between the front and back strips. The distribution of timing differences is displayed in Fig. 3.35, and a gate of 0.8 μs was placed on the decay events. The vast majority of events fell within this timing gate, with 99.99% of the events on the front and back of the detector occurring within 0.8 μs of one another. Analogous to Fig. 3.34, the energy vs timing difference for decay events is plotted in Fig. 3.36 for the front and back of the detector. The FWHM for the timing distribution is 0.112 μs.

In an event, more than one strip within the GeDSSD can record an energy. In order to define the location of the event, the weighted average of the energies of the strips is taken to determine

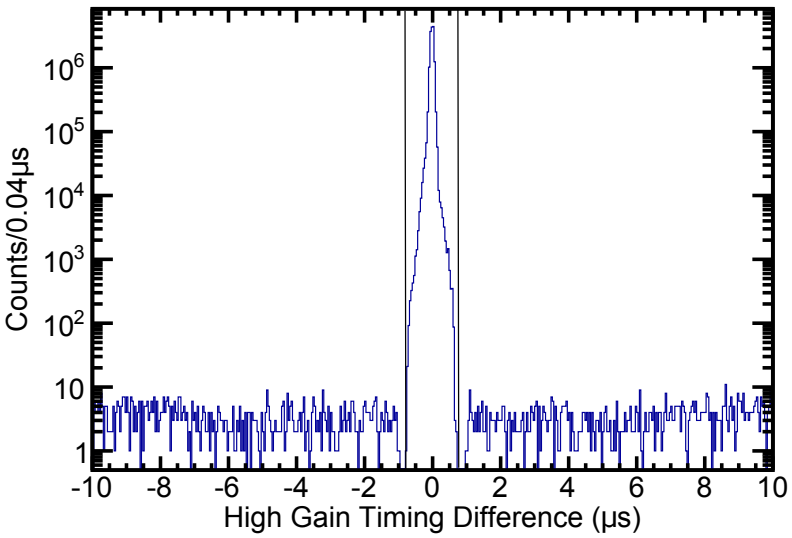

Figure 3.35 Back strip timing minus front strip timing for decay events. The timing gate is in black on the figure.

the event location:

$$maxch = \frac{\sum_{i=1}^{16} i \times E(i)}{\sum_{i=1}^{16} E(i)} \tag{3.10}$$

where *maxch* is the strip number of the strip centroid (rounded to the nearest integer), i is the number of the strip and $E(i)$ is the energy of strip i. The location of the event was determined by the energy centroid on both sides of the detector and corresponded to a pixel within the detector. The pixel location of an event was used along with timing information to correlate implants to their subsequent decay events. Decays must occur within the same pixel or one of the eight closest neighboring pixels as a preceding implant and within a specified timing window (the correlation window), which was chosen depending on the implantation rate and the half-lives of the produced nuclei. Typically, a correlation window was chosen on the order of 2-3 half-lives. For more details about the efficiency of correlation, see Section 3.4.2.2.

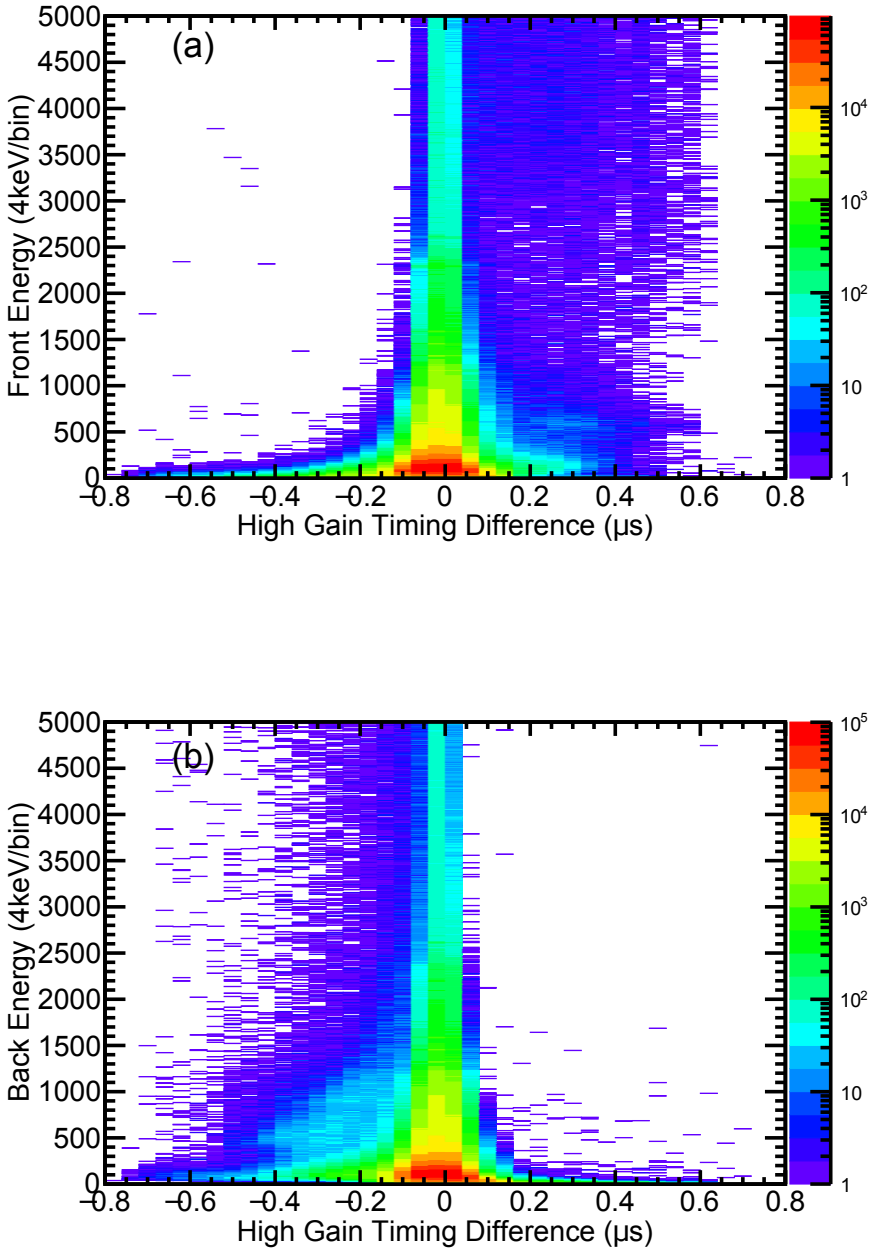

Figure 3.36 Energy of the strip chosen as the event location vs. the high-gain timing difference for (a) front strips and (b) back strips.

3.6 β-γ Summing

Given the high efficiency for detecting low-energy γ rays, it is possible that the β-decay electron and β-delayed γ rays could deposit their energies in the same location within the detector at the same time, thus summing their energies into a single-pulse. An algorithm to correct for this effect is discussed in this section. The β-γ summing effect is mitigated when studying isomeric states since the half-life of the metastable state provides a delay between β-decay electron and subsequent isomeric γ ray or conversion electron electron, separating them in time.

The algorithm to correct for the effects of β-γ summing was developed via simulation, and preliminarily verified by experiment. In the commissioning run e11503, ^{67}Fe was produced. This decay populates a 680.5-keV state which decays via a 188.9-keV transition in ^{67}Co [66] to a long-lived isomeric state. This transition was well-suited to studying β-γ summing algorithms due to the high efficiency for detection of a γ ray at 189 keV within the GeDSSD and the ability to detect coincident feeding transitions in SeGA (Fig. 3.37). For an isolated γ ray (in the absence of β-γ summing), the efficiency of the GeDSSD at 189 keV was 27.5% for the strips of the detector on a single side (see Fig. 3.29) based upon simulation. The additional presence of a β-decay electron in the simulation dropped this efficiency to 10%, because the energy from the electron will primarily be deposited in the strip where the ion was located, preventing any γ rays from being separately detected within that strip. If the electron travels beyond its initial strip, those strips would also sum with any γ-ray energy deposition, preventing detection of the γ ray's full-energy peak. For high-energy electrons, the electrons will lose anywhere from 10's of keV up to the total energy of the electron in a single strip. This results in a wide distribution of energies within a single strip of the GeDSSD.

3.6.1 Development of technique in simulation

In order to try to separate energy depositions due to β-decay electrons and β-delayed γ rays, the two dimensional capabilities of the detector were utilized. Recall that each strip reads out an

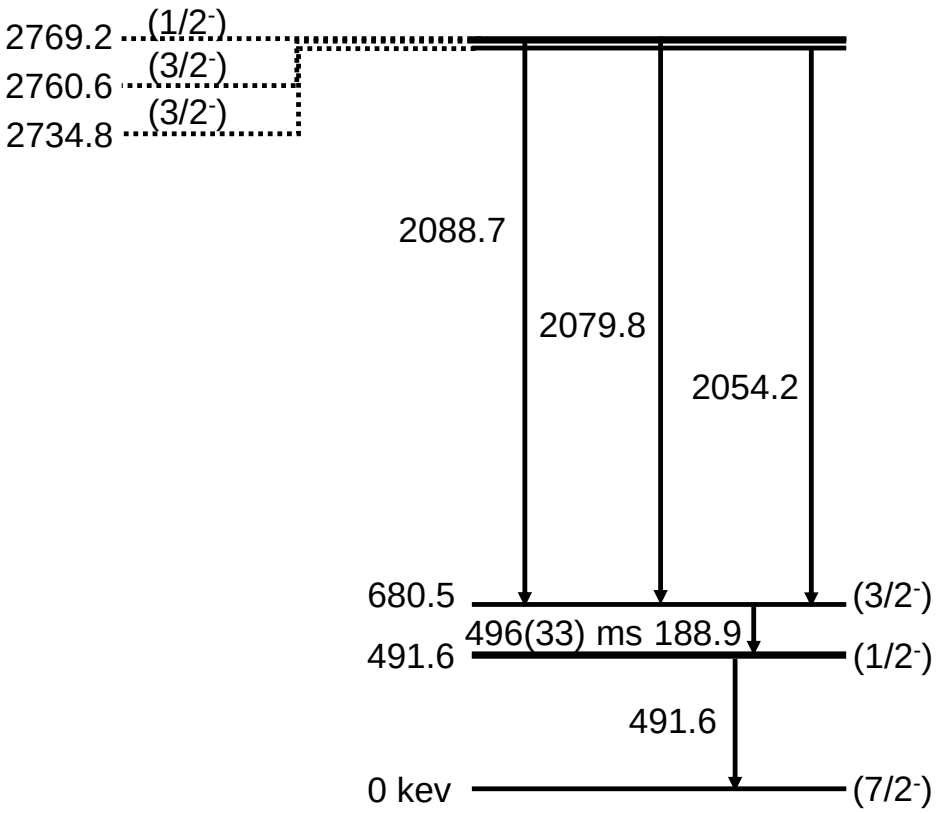

Figure 3.37 Partial level scheme and feeding in ^{67}Co. Data are taken from Ref. [66].

energy independently, and the pixel number was defined using the front and back strips in software as the location of the event. Alternatively, the event location can be defined as (1) the strip on both sides of the detector with the greatest amount of energy deposited (e11503 and e09055) or (2) the strip centroid (e11003). If more than one strip on a side recorded an energy above threshold, multiple pixels could be assigned an energy deposition but the conversion between multiple strips and multiple pixels is not necessarily unique. The position algorithm considers several different cases based on the strip multiplicity on the two sides of the detector (Table 3.3). The energy depositions on each side were organized into arrays ordered by descending energy, and the energy of single strips and sums of strips on one side of the detector were compared to the energy of single strips and sums of strips on the other side to find combinations of matching energies. Some of the possible combinations of strip energies will not be unique and, in some cases, several reconstructed positions were possible. This approach assumed that the total amount of energy deposited on both

sides is the same, i.e. $\sum_{i=1}^{x} E_{S1}(i) = \sum_{i=1}^{x} E_{S2}(i)$, where $E(i)$ represents the energy of a single strip and $S1$ and $S2$ denote the two sides of the detector.

Table 3.3 Description of strip arrangements and possible pixel reconstruction in the β-γ summing algorithm

Side 1 Multiplicity	Side 2 Multiplicity	Description of Strip Arrangement	Energy Relationship
1	1	Pixel at intersection of strips	$E_{S1} = E_{S2}$
1	x>1	Single strip on one side split into x pixels	$E_{S1} = \sum_{i=1}^{x} E_{S2}(i)$
2	2	Energy split by 2 by 2 box Two matching energy depositions	See text $E_{S1}(1) = E_{S2}(1); E_{S1}(2) = E_{S2}(2)$
2	x>2	One-to-one strip matches, single strip to sum of multiple strips	Check for matching strips in the above patterns
y>2	x>2	Many possible arrangements	Check for matching strips(s) in the above patterns

The scenarios described in Table 3.3 are depicted schematically in Fig. 3.38, Fig. 3.39, and Fig. 3.40. In each figure, a diagram of the GeDSSD divided into strips, and the intersection of strips is a pixel. The strips are labeled at the edge with the energies in the notation used in Table 3.3, and the pixels are labeled within the diagram with the pixel energies derived from the strip energies. For events with multiplicities greater than 1 on both sides, the algorithm searched for matching sums on both sides of the GeDSSD in these patterns until as many of the strip energies as possible were placed. Any remaining strips were left as strip energies and were added to the output spectra on their own. When one side had a multiplicity of 1, the pixel assignment was generally unambiguous, as all energies on the opposite side must sum to the energy of the single strip.

In a few cases, the energy of multiple strips was split among several pixels. The first of these possibilities was when both sides have multiplicity 2. If the individual energies did not match on both sides (see Fig. 3.40), then this energy was split between the pixels encompassing the

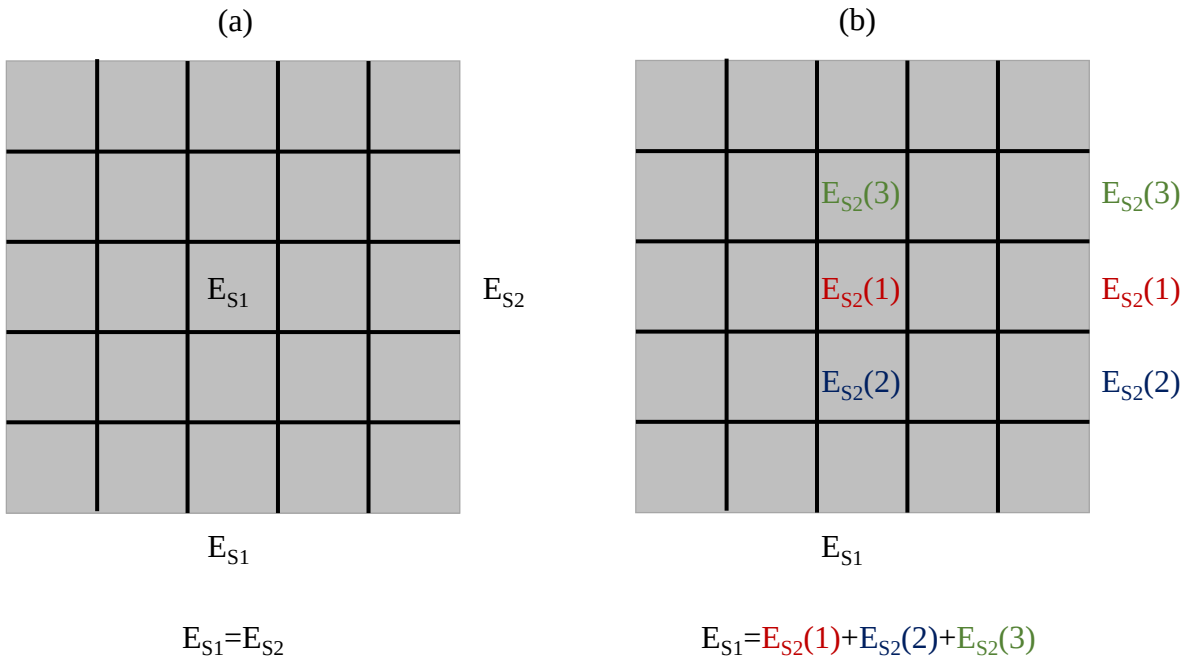

Figure 3.38 An illustration of the strip arrangements and pixel reconstruction as utilized by the β-γ algorithm for cases with multiplicity 1. (a) Multiplicity 1 on both sides. (b) Multiplicity 1 on a single side. Only one possibility exists for these cases.

intersection of the four strips. Assuming the pixel with the greatest amount of deposited energy was at the intersection of the two strips with the greatest amount of energy, two scenarios were possible if $E_{S1}(1) > E_{S2}(1)$ (for the case of $E_{S2}(1) > E_{S1}(1)$, $S1$ and $S2$ are simply swapped in the following schemes). If $E_{S2}(1) - E_{S1}(2) > E_{S1}(2)$ and $E_{S2}(1) - E_{S1}(2) > E_{S2}(2)$, the arrangement of pixels is shown in Fig. 3.40 panel a. Otherwise (if $E_{S2}(1) - E_{S1}(2)$ was less than the energies of either of the two strips with the lowest energy), the arrangement of pixels is shown in Fig. 3.40 panel b. This is, of course, not the only possible arrangement, though it's inclusion in the algorithm increases the fraction of γ rays recovered by about 3% absolute. This scheme was chosen based upon the most common and least ambiguous pixel arrangement since the energies could be calculated based upon addition and subtraction of strips, not random fractions of strip energies split among 4 pixels.

In total, when simulating the decay of ^{67}Fe, the algorithm recovered 17$\pm$1% of emitted γ rays at 189 keV, which is an increase over the amount recovered by a strip histogram (10%) in the presence of electrons.

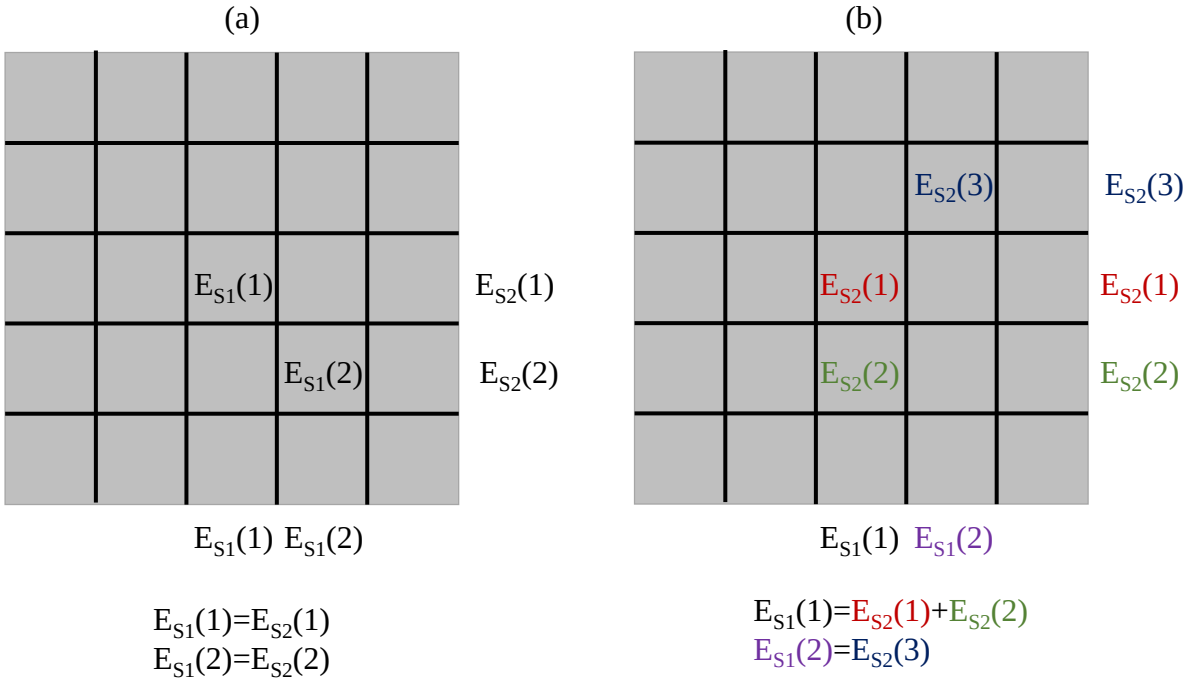

Figure 3.39 An illustration of the strip arrangements and pixel reconstruction as utilized by the β-γ algorithm for cases where one side has multiplicity 2. (a) Multiplicity 2 on both sides. (b) Multiplicity 2 on a single side. Multiple arrangements are possible.

3.6.2 Application of technique in data

In order to identify the decays of the ^{67}Co ions, several high-energy γ-ray transitions that populate the 680.5-keV state emitting the 188.9-keV γ ray were required to be observed in SeGA. These transitions are shown in Fig. 3.41. After gating on the high energy feeding transitions, the strip histogram (a plot of the energies deposited in all strips in the GeDSSD, without any β-γ summing algorithms applied) for both sides of the GeDSSD are shown in Fig. 3.41 and 3.42. The simulation predicted that the strip histogram would have an efficiency of 10$\pm$1%. Based upon the total number of counts of the gated SeGA γ rays and the known absolute efficiencies, 28$\pm$7 counts would be expected within the GeDSSD strip histograms. The experimental spectra were consistent, within error, of this value.

After applying the β-γ summing correction algorithm on the experimental data, there was an increase in counts in the 188.9-keV peak. The simulation predicted that 17$\pm$1% of the emitted γ

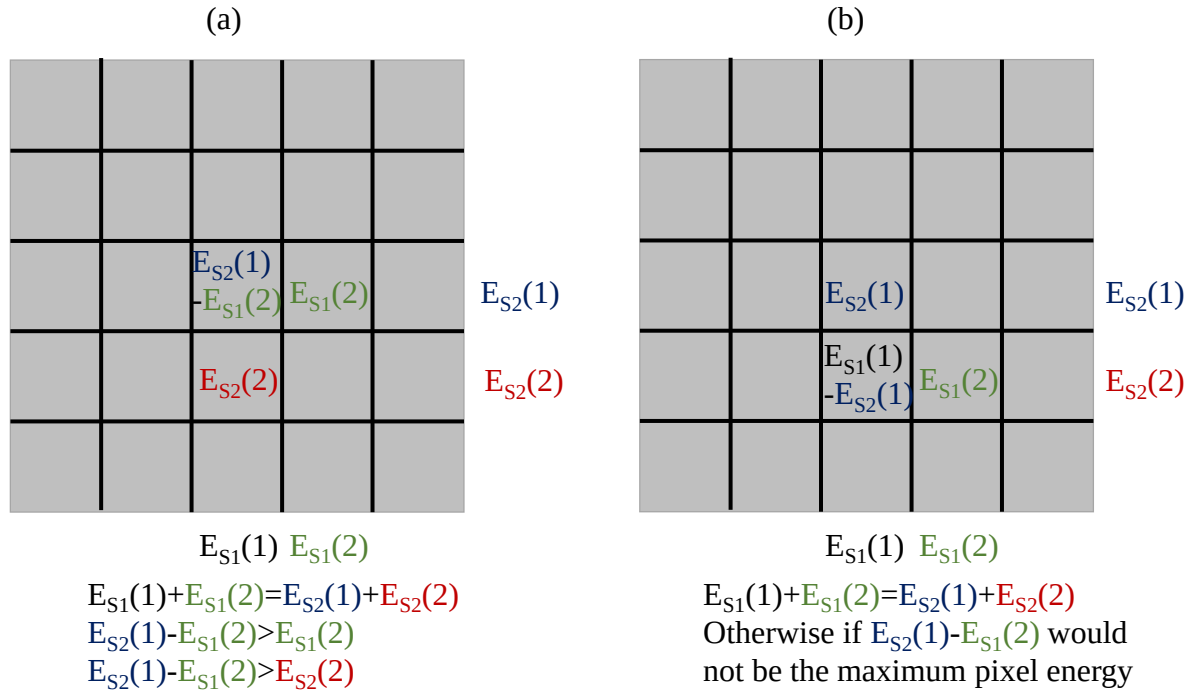

Figure 3.40 An illustration of the strip and energy arrangements for two cases where the energy within the strips is split between multiple pixels. (a) If $E_{S2}(1) - E_{S1}(2) > E_{S1}(2)$ and $E_{S2}(1) - E_{S1}(2) > E_{S2}(2)$, this arrangement puts the maximum energy at the intersection of the strips with the highest energy. (b) Otherwise, if $E_{S2}(1) - E_{S1}(2)$ would not result in the highest pixel energy, this alternate arrangement preserves the maximum pixel location.

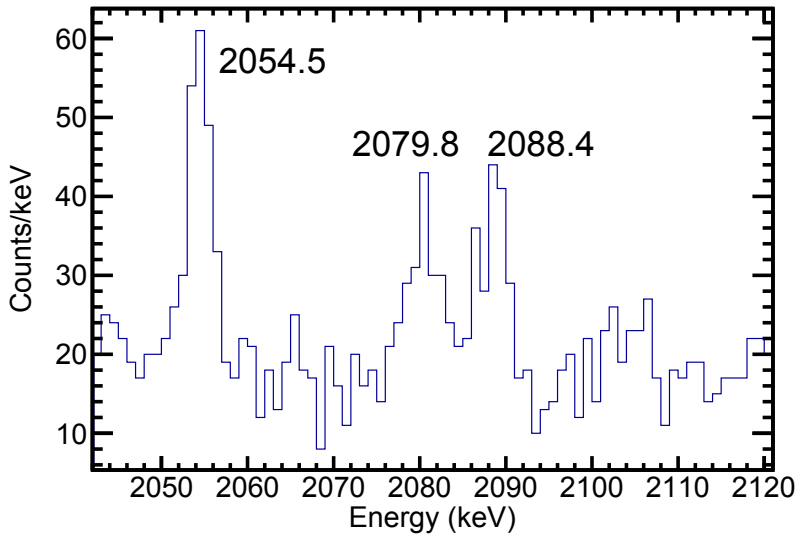

Figure 3.41 SeGA energy spectrum showing the higher energy γ rays at 2088.7, 2079.8, and 2054.2 keV used as gates to select the 188.9 keV transition used for testing the β-γ summing algorithm.

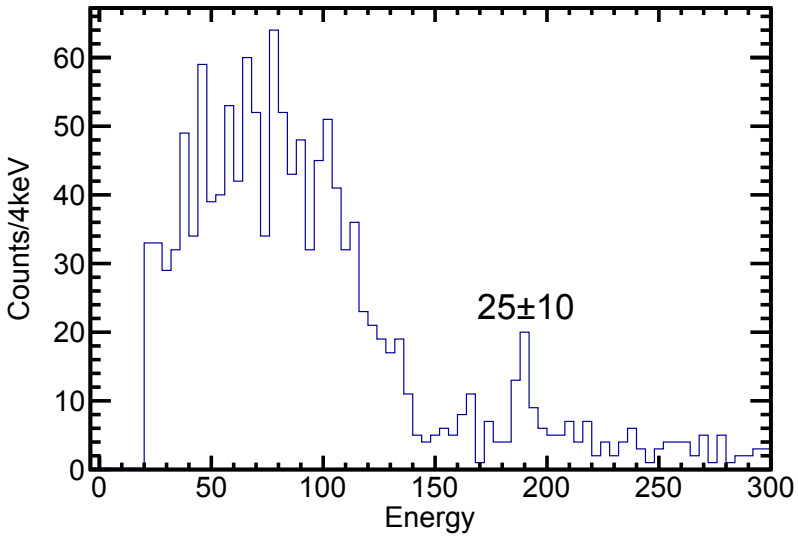

Figure 3.42 Strip energy spectrum of the back side of the GeDSSD after gating on the γ rays shown in Fig. 3.41. The number of counts in the peak at 189 keV is consistent with the 10% predicted by simulation.

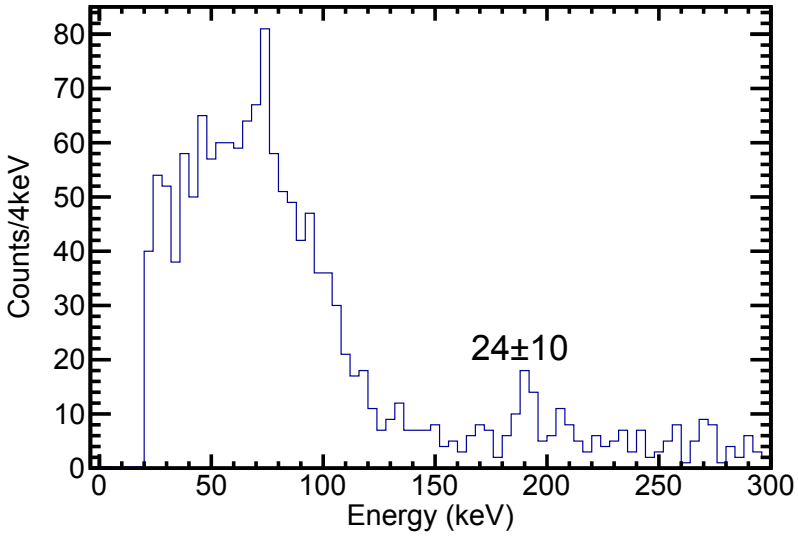

Figure 3.43 Strip energy spectrum of the front side of the GeDSSD after gating on the γ rays shown in Fig. 3.41. The number of counts in the peak at 189 keV is consistent with the 10% predicted by simulation.

rays would be observed, leading to an expectation of 48±13 counts at 189 keV. The experimental γ-ray energy spectrum after applying the β-γ summing algorithm is shown in Fig. 3.44, where the peak has 32±11 counts, which agrees with the lower predicted range of the algorithm.

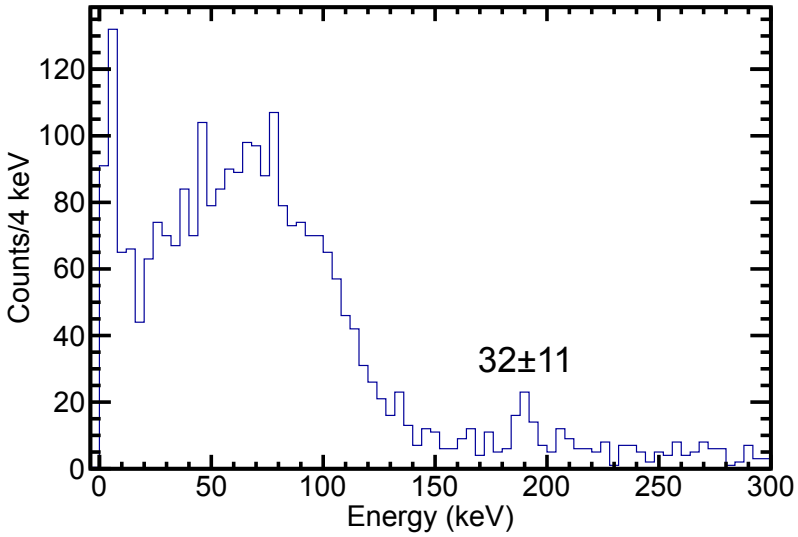

Figure 3.44 Energy spectrum in the GeDSSD from the β-γ summing algorithm to re-create the pixel energies gated on the three high energy transitions, 2055, 2080, 2088 in ^{67}Fe. The intensity of the 189-keV transition is shown.

3.7 Double-pulse processing

The deposition of energy within the GeDSSD creates a voltage signal from the preamplifier with a sharp rise from a baseline voltage, rising to a maximum and then decaying with a characteristic decay time back toward the baseline. However, some pulses deviating from this characteristic shape can be found in the data. While some alternate shapes are not understood and can be filtered out by pulse processing, those pulses that look like a stair-step are two pulses in one trace separated by an amount of time less than the trace length (Fig. 3.45). A trace of this type corresponds to two energy depositions very close in time within a single strip, such as the population and subsequent decay of short-lived isomeric states. Thus, both the timing between the two pulses and

the amplitude (energy) of any pulse with this shape can be extracted. The technique described in this work to analyze double-pulses was adapted from work in Ref. [67, 68].

To identify these double-pulses, an ideal pulse-shape database for each channel in the GeDSSD was generated based upon averaging the trace shape for each strip for the 662-keV γ ray from a ^{137}Cs source. A minimum of 1000 baseline subtracted traces were averaged for each strip. The trigger of the rise within the traces was found and aligned so that all traces triggered at the same point within the trace (and thus aligned the rises of the traces). Traces with leading edges before the common start point (here at 500 clock ticks or 4 μs) were delayed, and traces triggering after the common start point were advanced so that the leading edges of all traces started at 500 clock ticks. The total length of a trace is 2500 clock ticks, or 20 μs.

First, the trace fit was attempted with a single-pulse-shape. The form of the fit was:

$$Fit[i] = B + S \times (IdealPulse[i+P]) \tag{3.11}$$

where $Fit[i]$ is the value of the fit in ADC units, B is a the value of the baseline, S is a scaling factor, and $IdealPulse[i+P]$ is the pulse height in ADC units at bin i as determined by the ideal shape of that strip including a timing offset P. The ideal pulse was scaled to match the height of the trace, which also gives the energy.

A trace was fit between bins 200 and 2300, encompassing a portion of the baseline, the rise, and a portion the decay back toward baseline within the trace length. The baseline was determined by averaging the value of trace between 10 and 300 clock ticks, and was kept constant in the fit, while the scaling factor and timing offset parameters were allowed to vary freely. The chi-square of the fit was defined as follows:

$$\chi^2 = \sum_{i=200}^{2300} (Trace[i] - Fit[i])^2 \tag{3.12}$$

where $Trace[i]$ and $Fit[i]$ are the values of the trace and the fit of the pulse at index i in ADC units. The error in the $Trace[i]$ and $Fit[i]$ are assumed to be 1.

The logarithm of the chi-square divided by the amplitude of the trace is shown in Fig. 3.46 for the front and Fig. 3.47 for the back. The value of the chi-square was systematically higher for

signals with larger amplitudes, so the chi-square was divided by the height of the trace to account for this effect. The logarithm of the normalized chi-square values made the figure of merit easier to visualize. This value was compared to selected cutoffs in order to identify whether a trace is a single-pulse. For the front, the value selected as a cutoff was 3.15, while for the back this value was 3.05. These values were chosen to minimize the number of single traces at the tail end of the distribution being labeled a double trace, and to maximize the number of double traces with short timing differences. If the single chi-square cutoff was too low (for example, 2.9 on the back side of the GeDSSD), traces with a slow rise time like the one shown in Fig. 3.48 fail the single-pulse test, and are subsequently labeled a double-pulse. Likewise, if the single-pulse chi-square was too high, some of the double-pulses with short timing differences passed the single-pulse chi-square cutoff, and thus did not get labeled as a double-pulse. Fig. 3.49 shows a double-pulse that passed the single-pulse test when the chi-square value was 3.2. The final value of the single chi-square was chosen to balance between these two effects. Near the cutoff, both single traces with a slow rise time and double-pulses with a short timing difference between the two pulses exhibit similar chi-square values.

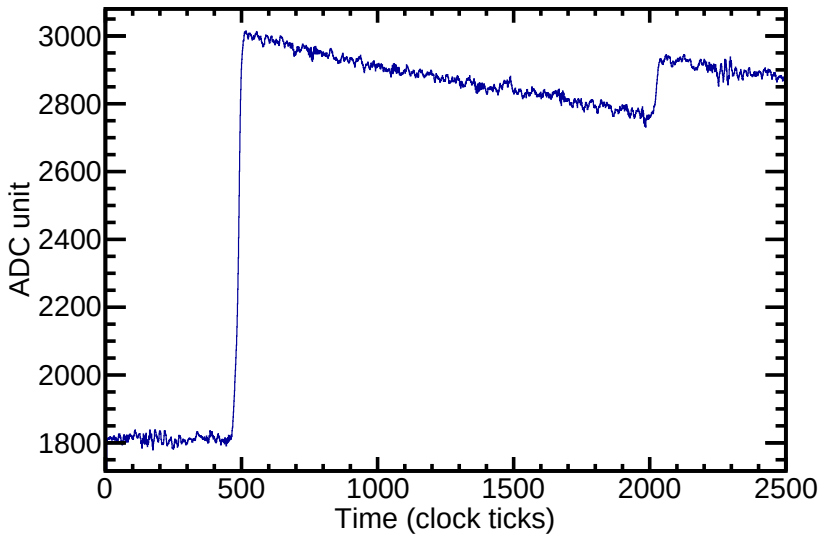

Figure 3.45 An example trace exhibiting the double-pulse-shape searched for by this technique.

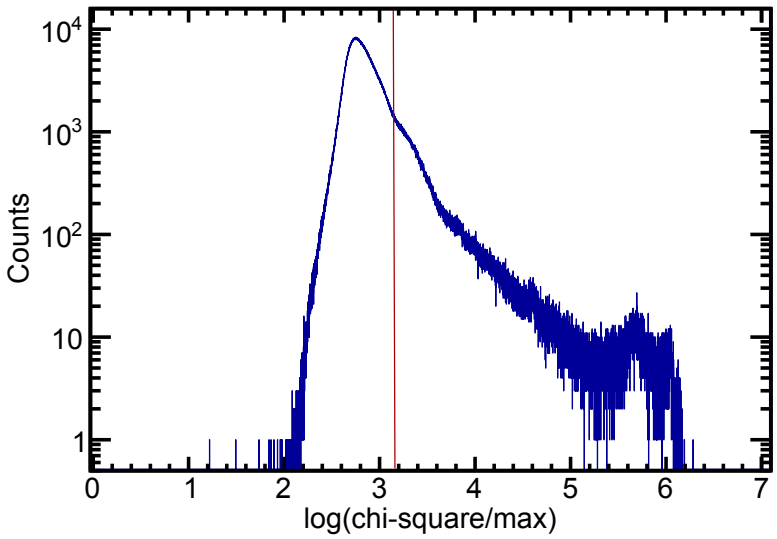

Figure 3.46 The log of the chi-square distribution of the single-pulse fit over the amplitude of the pulse for the front strips of the detector. A cutoff of 3.15 (shown as the red dashed line) for the front strips was used to determine whether the fit was good.

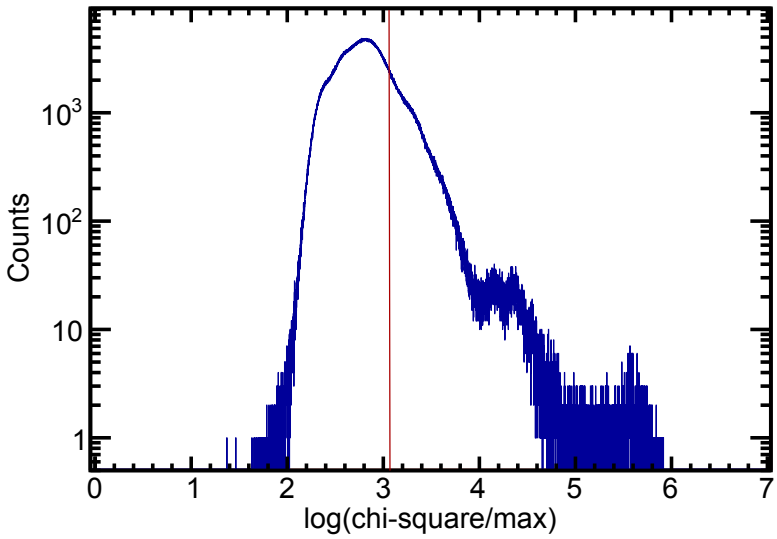

Figure 3.47 The log of the chi-square distribution of the single-pulse fit over the amplitude of the pulse for the back strips of the detector. A cutoff of 3.05 (shown as the red dashed line) for the back strips was used to determine whether the fit was good.

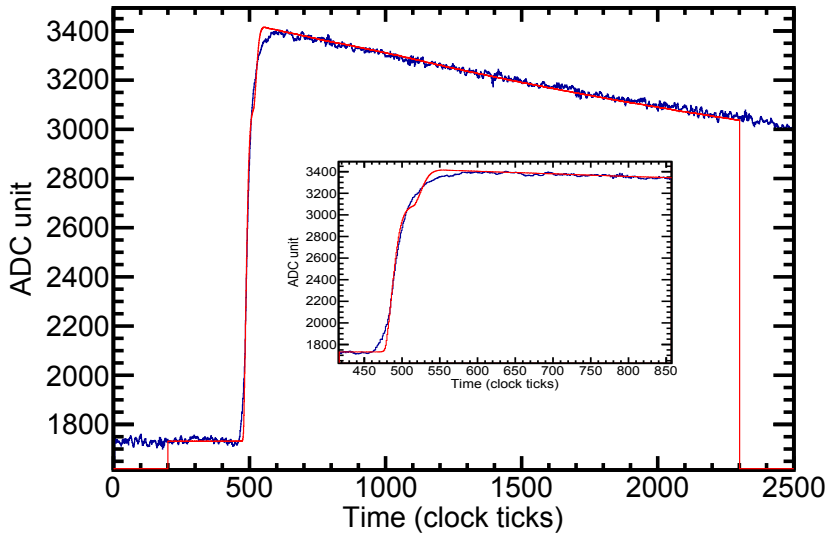

Figure 3.48 An example trace on the back side of the detector incorrectly labeled as a double trace if the cutoff is lowered to 2.9. The inset shows a closer view of the rise to illustrate the double-pulse fitting. The trace is shown in blue while the fit is shown in red.

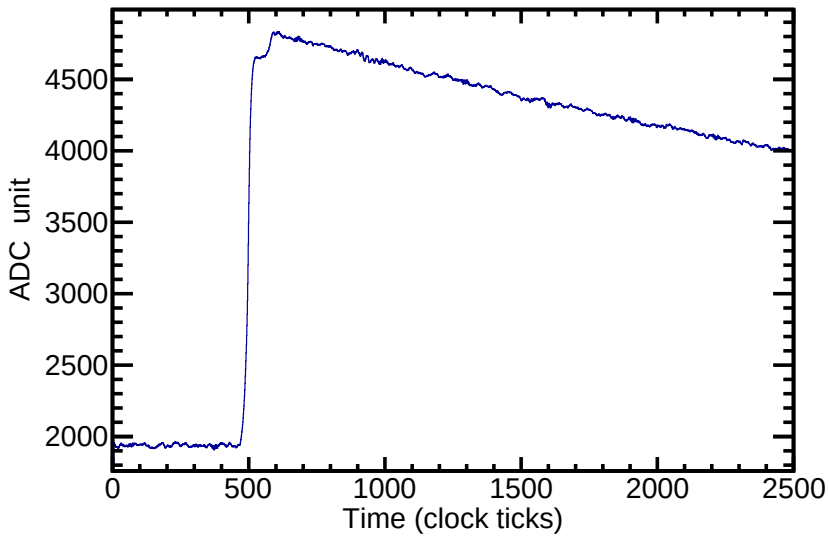

Figure 3.49 An example trace on the back side of the GeDSSD incorrectly labeled as a single-pulse when the cutoff was raised to 3.2. This trace that clearly has two parts and should be classified as a double-pulse.

If the single-pulse test was failed, then a fit of a combination of two single-pulses offset in time (a double-pulse) was attempted. The form for a double-pulse fit was the sum of two single ideal pulses, offset in time:

$$Fit[i] = B + \sum_{k=1}^{2} S_k \times (IdealPulse_k[i + P_k] \tag{3.13}$$

where B is the baseline, S_k are the scaling factors, P_k are the timing offsets of the two pulses, and the sum is over k single-pulses. Each pulse was individually scaled for the height of the trace, and was fit for a timing offset (relative to 500 clock ticks). If the double fit was good, then that event was identified as a double-pulse event. For all pulses for which a double fit was attempted, the chi-square results (calculated in the same way as for the single fits) are shown in Fig. 3.50 for the front of the detector and Fig. 3.51 for the back. A cutoff of 2.95 was utilized for the front strips, and a cutoff of 2.85 was chosen for the back to identify double-pulses. As with the single fits, the chi-square values were chosen to maximize the number of double-pulses passing, and minimizing the number of other pulse-shapes passing. In the front strips, compare to the back strips, there was a larger number of unusually shaped traces. These traces failed the single-pulse test, but many were able to pass the double-pulse test with chi-square values similar to those of true double-pulses. For these reasons, the distributions in the double-pulse chi-square are different. An example of a well-fitting double-pulse is shown in Fig. 3.52.

In order to ensure that the values of the fit parameters remain physical, a limit of 30 clock ticks was placed on the timing difference between pulses, and both pulses must have a positive energy. A timing limit shorter than 30 clock ticks allowed more single-pulses, as well as pulses with a transient signal on the rise, to pass the double-pulse requirements. With the length of the trace and the minimum pulse separation, the half-lives that may be studied by this technique were limited between 240 ns and 20 μs. If neither fit matched the trace well, then the trace was most likely noisy or otherwise poorly-shaped trace, and is thus not included in the single or double-pulse results. Out of all events, only a very small percentage, 0.04%, were double-pulses with acceptable parameters. Results from this technique will be discussed in Sections 5.3.1 and 5.3.2.

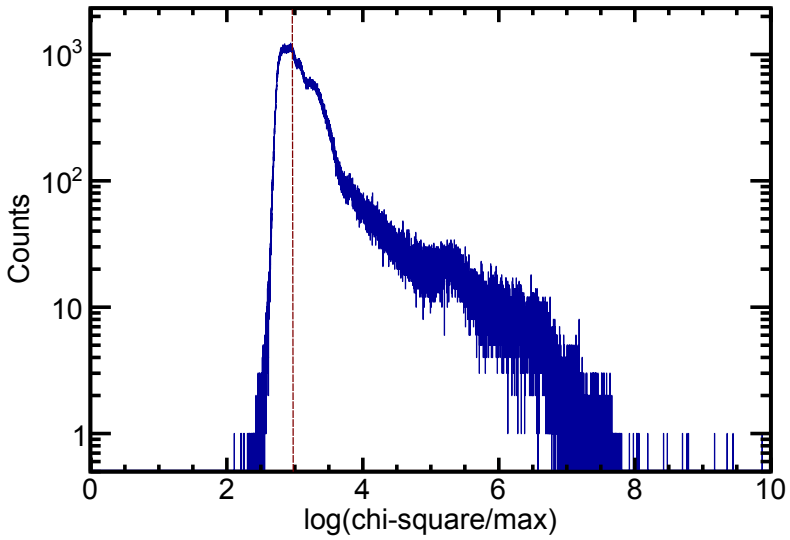

Figure 3.50 The log of the chi-square distribution of the double-pulse fit over the amplitude of the pulse for the front strips of the detector that failed the single fit. A cutoff of 2.95 for the front strips was used to determine whether the fit was good and therefore could be considered a double-pulse.

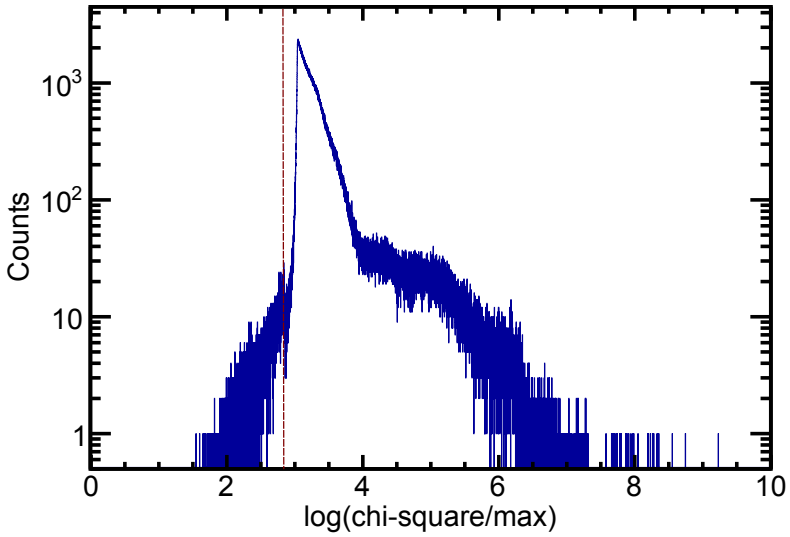

Figure 3.51 The log of the chi-square distribution of the double-pulse fit over the amplitude of the pulse for the back strips of the detector that failed the single fit. A cutoff of 2.85 for the back strips was used to determine whether the fit was good and therefore could be considered a double-pulse.

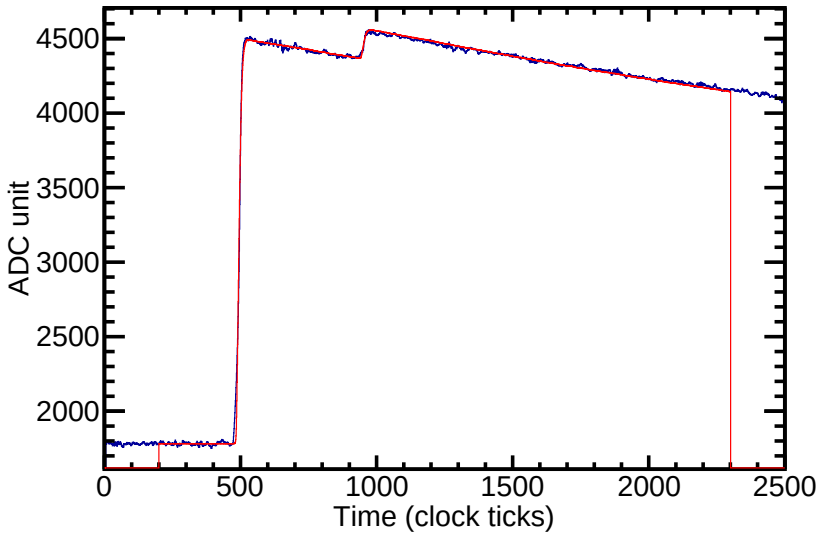

Figure 3.52 An example double-pulse (blue) with the fitted function (red).

CHAPTER 4

EXPERIMENTAL SETUP

4.1 Introduction

For the remainder of this document, results from a NSCL experiment focused on populating A$\sim$110 nuclei with Z between 40 and 46 will be discussed. Nuclei in this region have long been of interest due to the rapidly changing structure within the region [25, 27, 69–71]. An example of an isotopic chain (Ru) exhibiting these structural changes was discussed in Section 1.2.2. In particular, experiment e11003 focused on producing Nb, Mo, Tc, and Ru isotopes to search for isomeric states in Mo, Tc, Ru, and Rh daughter nuclei. This chapter present details of the detector and beams used for the experiment. The experimental setup for e11003 was very similar to the commissioning run setups. Ions were transmitted through two PIN detectors, a Kapton window, a few cm of air and then came to rest inside the GeDSSD. The GeDSSD was discussed in detail in Chapter 3. Surrounding the GeDSSD were 9 HPGe clover detectors [51], which will be discussed in greater detail in Section 4.4

4.2 Beam settings

For neutron rich nuclei with A$\sim$110, the LISE code [59] predicts low production rates, with some nuclei expected to be produced with only 500 ions over the course of 10 days. Three rigidity settings of the A1900 fragment separator [41] were used to determine the final production setting and are listed in Table 4.1. At each setting, the PID (particle identification) was confirmed using β-delayed γ rays from known isotopes that were implanted in the GeDSSD before moving to the next setting. The primary beam was ^{124}Sn at an energy of 120MeV/u for all the secondary beam settings, and was impinged on a ^{9}Be target, the thickness of which depended upon the beam setting (see Table 4.1). The second half of the A1900 was kept at a constant rigidity of 3.931 Tm

to simplify particle identification, as was the Kapton wedge, at a thickness of 20 mg/cm^2. The primary ^{124}Sn beam was delivered to the end-station in two charge states, fully-stripped ^{124}Sn^{50+} and Hydrogen-like (H-like) ^{124}Sn^{49+} to calibrate the low-gain strips in the GeDSSD and PIN detectors for a Total Kinetic Energy (TKE) measurement. The energies of the ^{124}Sn beams are summarized in Table 4.2. Both Sn beams were run at the start of the experiment, with the fully-stripped run for 60 minutes and the H-like for 15 minutes. The fully-stripped beam was run again at the end of the beam time for an additional 90 minutes. The first half of the A1900 had a rigidity setting for the fully-stripped and H-like beams of 3.931 Tm and 3.962 Tm, respectively.

Table 4.1 Summary of the three beam setting used in the experiment.

Central Isotope	Bρ First Half (Tm)	Bρ Second Half (Tm)	Target Thickness (mg/cm^2)	Momentum Acceptance (%)	Wedge Thickness (mg/cm^2)
^{118}Ag	4.033	3.931	9	0.5	20
^{117}Ru	4.039	3.931	141	1.5	20
^{112}Nb	4.038	3.931	188	5	20

Table 4.2 The predicted energy deposition from LISE within the PINs and GeDSSD for the two Sn beams in e11003.

Beam	Detector	Energy (MeV)
^{124}Sn^{50+}	GeDSSD	6854
	PIN 1	1486
	PIN 2	1522
^{124}Sn^{49+}	GeDSSD	6056
	PIN 1	977
	PIN 2	1007

The first A1900 setting was centered on ^{118}Ag with a 0.5% momentum acceptance and a 9 mg/cm^2 Be production target. This beam was characterized by the A1900 group and the PID was confirmed by decays. The first setting ran for approximately 9 hours. The second setting was centered on ^{117}Ru with a 1.5% A1900 momentum acceptance and a 141 mg/cm^2 Be production

target. This setting was chosen as an intermediate rigidity to check the scaling of the A1900 separator. The second setting ran for approximately 18 hours and the PID was confirmed again based on the β-γ coincidences (discussed in Section 5.4.1). The final A1900 setting for ^{112}Nb utilized the full 5% momentum acceptance of the A1900 and a 188 mg/cm^2 Be production target. The ^{112}Nb secondary beam ran for the remainder of the beam time of approximately 98 hours and the PID was confirmed based on the β-γ coincidences (see Section 5.4.2).

4.3 Particle identification

Multiple isotopes were delivered to the experimental end-station in a so-called cocktail beam, and event-by-event isotope identification was performed with ΔE and TOF measurements. Two PIN detectors of thicknesses 488 and 303 μm were placed approximately 1 m upstream of the GeDSSD in vacuum. With the ^{124}Sn^{50+} beam, the PIN resolutions at 1486 MeV for PIN 1 (448 μm) was 2.3% and at 1522 MeV for PIN2 (303 μm) was 2.2%.

As particles pass through a material, the particles lose energy in proportion to Z^2. The energy deposited into PIN 1 for the Ru beam setting is presented in Fig. 4.1 and several peaks are apparent corresponding to the elements delivered during the experiment. The relationship between energy loss and the Z of a heavy charged particle can be expressed through the Bethe formula [65]:

$$-\frac{dE}{dx} = \frac{4\pi e^4 z^2}{m_0 v^2} NZ \left[ln\frac{2m_0 v^2}{I} - ln\left(1 - \frac{v^2}{c^2}\right) - \frac{v^2}{c^2} \right] \tag{4.1}$$

where $\frac{dE}{dx}$ is the differential energy loss for a particle within a medium, v is the velocity of the particle, z is the atomic number of the particle, N is the number density of the material, Z is the atomic number of the material, I is the average excitation and ionization potential of the absorber, m_0 is the electron rest mass, c is the speed of light, and e is the charge of the electron.

One method for identifying the mass number of the produced ions is a TOF measurement. The A1900 selects ions with the same momentum to charge ratio: $\frac{mv}{q}$. With all the ions produced at roughly the same velocity, the TOF is proportionate to a particle's mass to charge ratio if all

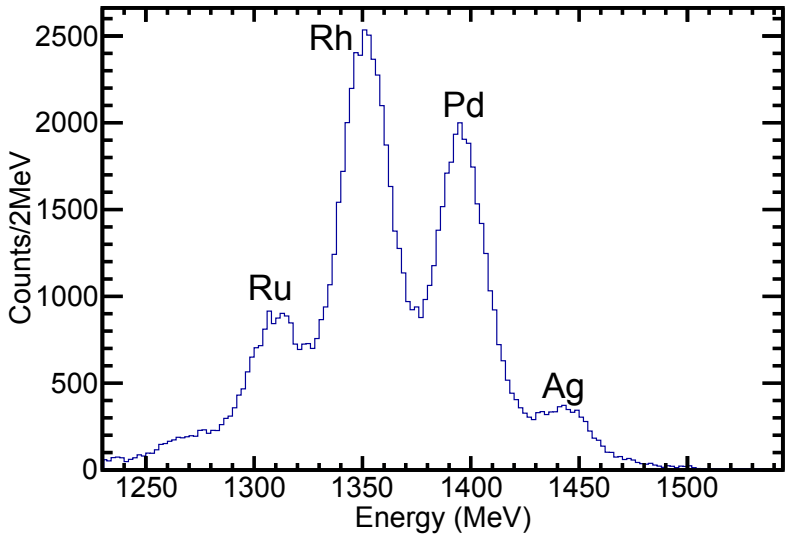

Figure 4.1 PIN 1 energies (ΔE signals) for the Ru beam setting. The different elements are marked on the figure.

particles have the same total path length. The TOF was measured between PIN 1 at the front of the setup and the scintillator at the intermediate dispersive image 2 (I2) position in the A1900. The PIN timing was used as a start signal and the timing from the I2 scintillator at the center of the A1900 was delayed and used as a stop signal. In this way, ions that did not make it from the accelerator to the experimental end-station did not produce start signals without subsequent stop signals in the data acquisition. At high momentum acceptances and heavier masses, two additional factors complicate the ΔE and TOF identification techniques: variations in ion path length and charge state ambiguities.

4.3.1 Image 2 TOF correction

The first factor complicating ion identification is that the TOF depends upon the ion's total path length through the A1900. Particles can take slightly different paths through the separator due to their momentum. This results in different total travel distances through the separator, blurring the TOF, and requiring correction so that the TOF of the ions is independent of their path. The momentum of a particle is correlated with its position at Image 2 of the A1900 and the TOF can be

corrected with a position measurement. This effect is illustrated in Fig. 4.2, where the correlated position at I2 with the raw TOF is visible in (a) and the non-corrected poor particle identification in which the individual isotopes are unresolved is visible in (b). The TOF was corrected to be independent of the ion's position in the I2 scintillator and the resulting corrected TOF and PID are shown in Fig. 4.3.

4.3.2 Total kinetic energy

The second factor complicating ion identification is the production of multiple charge states of the same isotope leading to ambiguities in the PID because multiple isotopes of a given Z can have very similar mass to charge ratios. The experiment was found to have delivered fully-stripped, H-like (one electron remaining), and He-like (two remaining electrons) secondary ions to the experimental end-station. For example, $^{118}Rh^{45+}$ has a mass to charge ratio of 2.62, $^{115}Rh^{44+}$ has a mass to charge ratio of 2.61, and $^{119}Rh^{45+}$ has a mass to charge ratio of 2.64. Therefore, in the present experiment, adjacent masses in an isotopic chain with the same charge state will appear as distinct groups n a PID plot but will be contaminated with the (A-3) mass nucleus in a lower charge state. This difficulty is depicted by the cartoon in Fig. 4.4. The experimental PID can be seen in Fig. 4.5; the group marked with a black circle contains both $^{118}Rh^{45+}$ and $^{113}Rh^{44+}$.

One method to separate different charge states is to measure the TKE of the ions since the TKE is proportional to the mass of the ion. In an ideal experiment, the TKE can be reconstructed from the energy deposited into all of the detectors. In the present system, this was not possible due to the GeDSSD cryostat. In experiment e11003, the ions passed through the PIN detectors, a Kapton window, a small amount of air, the GeDSSD's Al cryostat, and finally are stopped in the GeDSSD, depositing all remaining energy. This is illustrated in the cartoon in Fig. 4.6. Since the I2 scintillator provides a measure of the momentum, plotting the sum of energies in the PIN detectors and the GeDSSD versus the position within the I2 scintillator should show a correlation and a way to separate multiple charge states. According to LISE calculations, the TKE for the ions produced in experiment e11003 was expected vary between 4 and 11%, depending on the ion. For

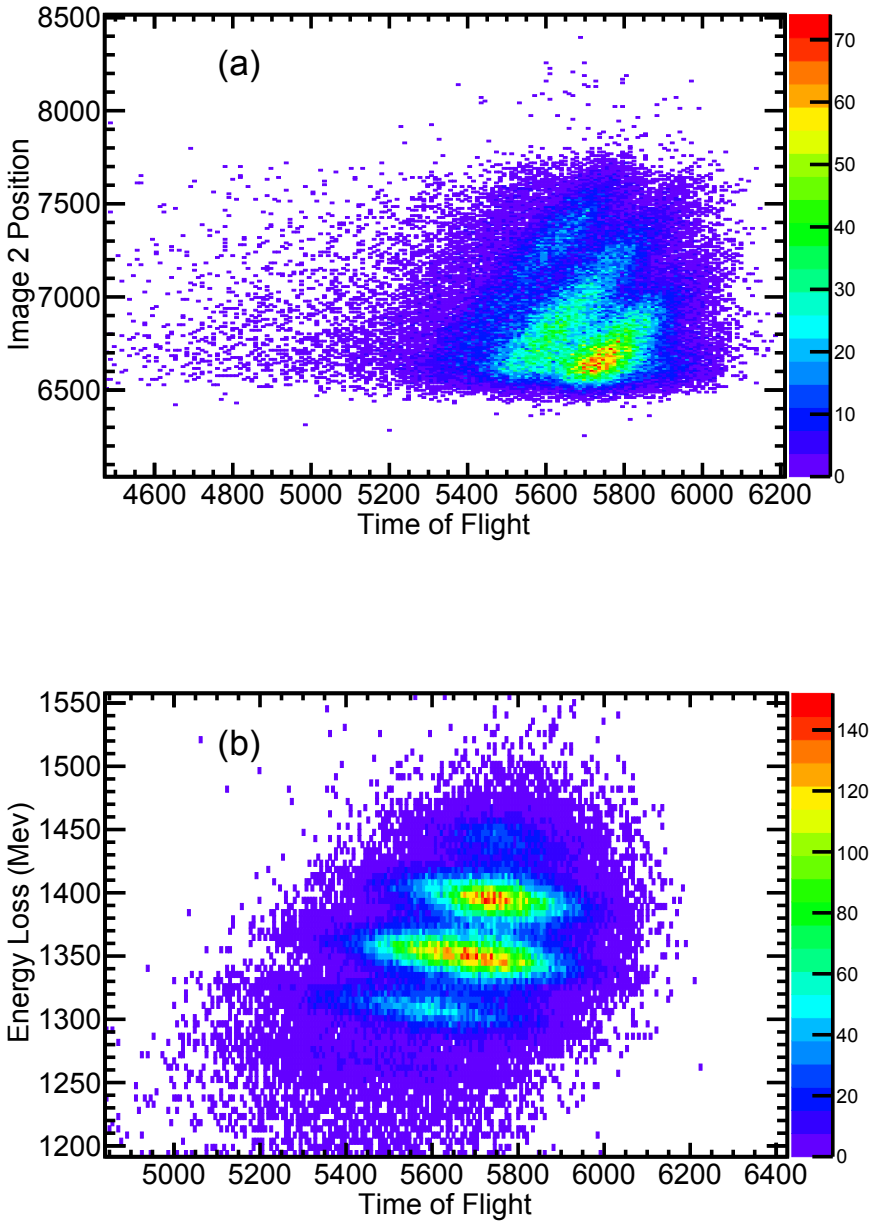

Figure 4.2 (a) TOF (arbitrary units) vs. Image 2 position for all particles illustrating the need to correct TOF. (b) The PID plot for the Ru setting with non-corrected TOF (arbitrary units). The isotopes overlap in this figure although the elements are separated.

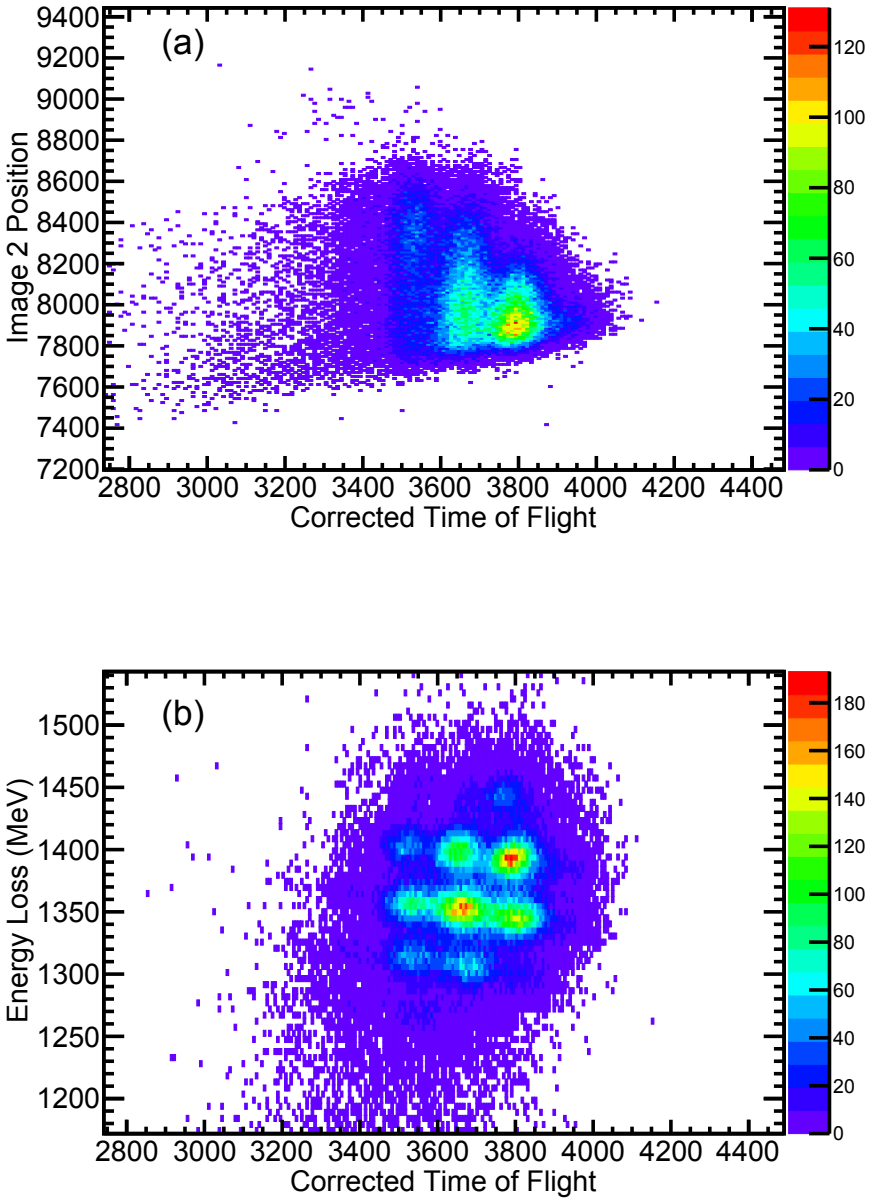

Figure 4.3 (a) The corrected TOF (arbitrary units) and Image 2 position for all particles illustrating the same TOF for all positions within the I2 scintillator. (b) The PID plot for the Ru setting with the corrected TOF (arbitrary units).

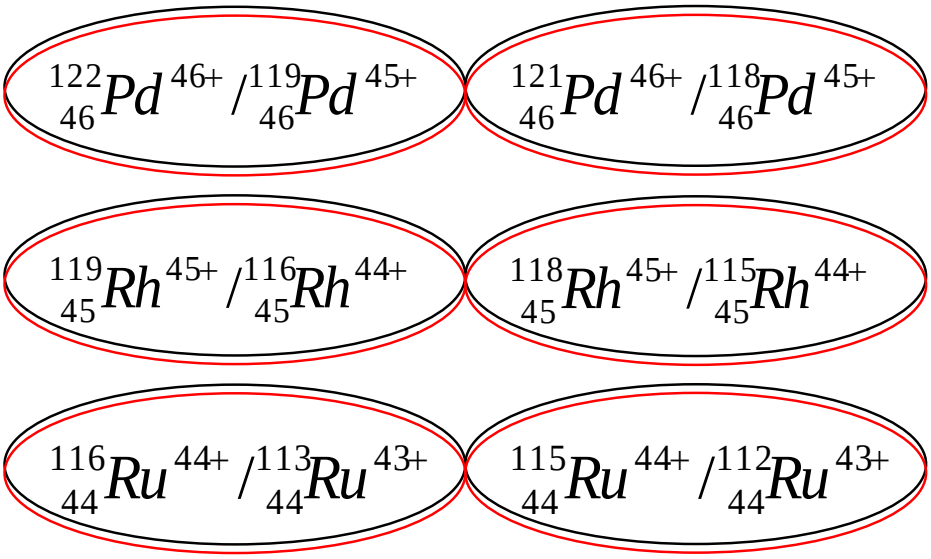

Figure 4.4 Cartoon depicting the problem created by the creation of multiple charge states. Each charge state forms a PID. These PID overlap, creating gates that include multiple nuclei. The charge states shown match what was observed in the Ru secondary beam setting.

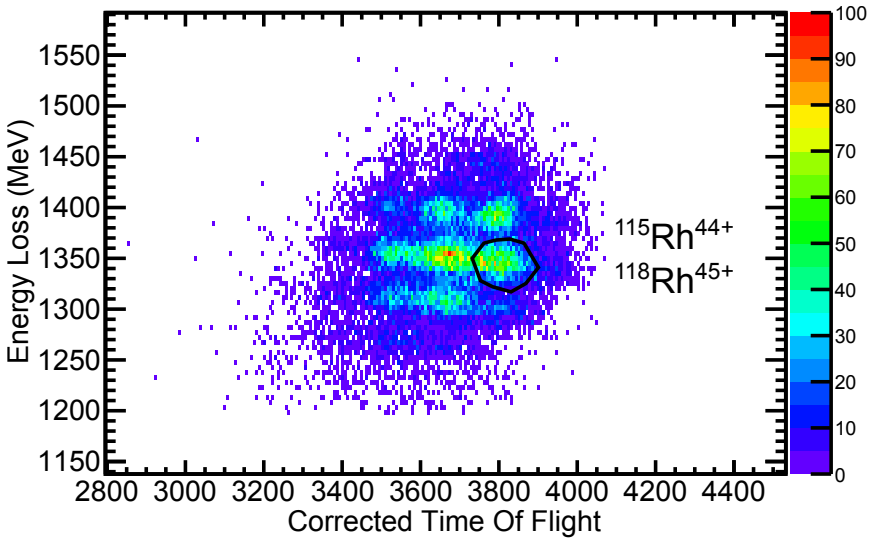

Figure 4.5 PID for the Ru setting. The spot marked contains $^{115/118}$Rh, which was used to investigate TKE measurements to separate different charge states.

the $^{115/118}$Rh example, the expected separation is 4.9%. The calibration over time for the front low-gain strips shifted on the order of 2%, so the gain matching as a function of time (discussed in Section 3.3.3.2) was important to obtain a good TKE measurement. The sum of the energy deposited in the PINs and the low-gain strips of GeDSSD was used to approximate the TKE (as there were additional materials the beam passed through on its way to the sensitive volumes of the detectors, losing more energy that was not detected). The position at the I2 scintillator is plotted vs. the TKE in Fig. 4.7 with the expected locations of ^{115}Rh and ^{118}Rh indicated. The figure is constrained to events within the edge strips of the detector. The middle of the detector was more significantly radiation damaged (see Section 3.3.3.2), and clear separation was not achieved. For comparison, the I2 position vs. TKE is displayed for ions that struck the middle of the detector in

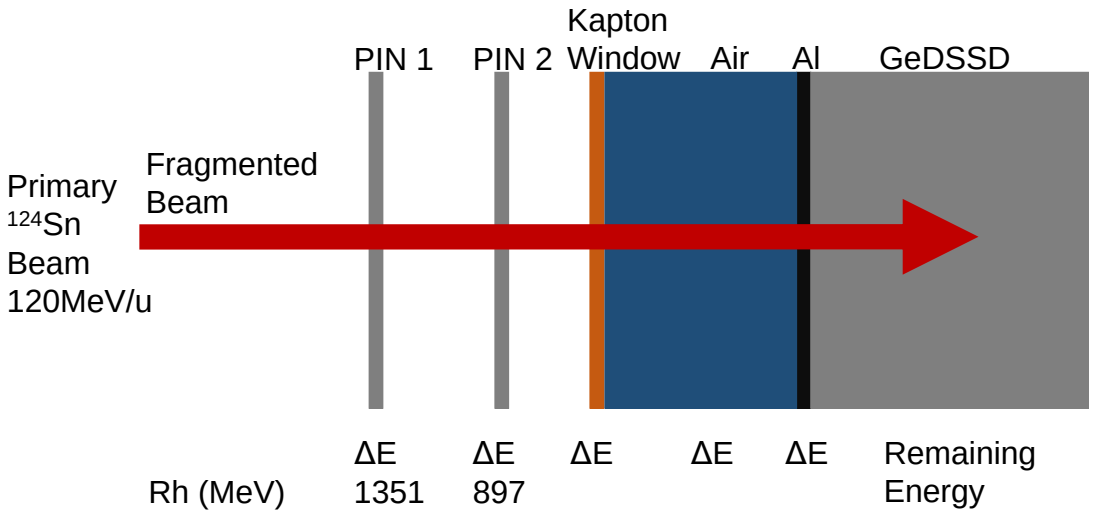

Figure 4.6 Cartoon depicting the deposition of energy as ions move through the experimental setup. As an example, the energy deposition in the PIN detectors of the produced Rh isotopes are noted.

The β-delayed γ-ray spectrum observed within 500 ms of the arrival of a ^{115}Rh^{44+} or ^{118}Rh^{45+} ion is shown in Fig. 4.9. Previously known γ rays from both isotopes [72–74] can be observed and are labeled with their respective energies. The same spectrum obtained with the edge strips of the GeDSSD is shown in Fig. 4.10, and the same transitions were observed. Figs. 4.11 and 4.12 illustrate the separation of the two charge states by comparing the β-delayed clover spectra from

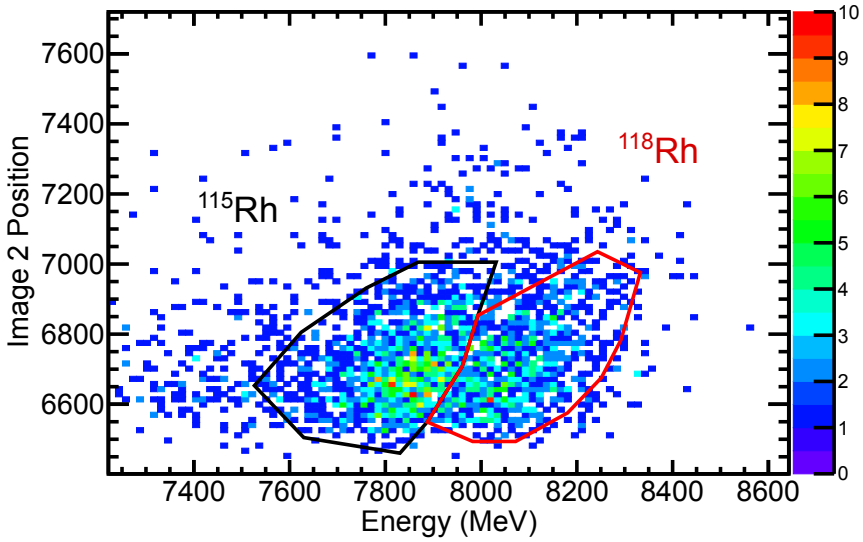

Figure 4.7 The TKE vs. the position of the ions within the Image 2 Scintillator that demonstrate the separation of charge states. This figure shows events only for the edge strips in the detector.

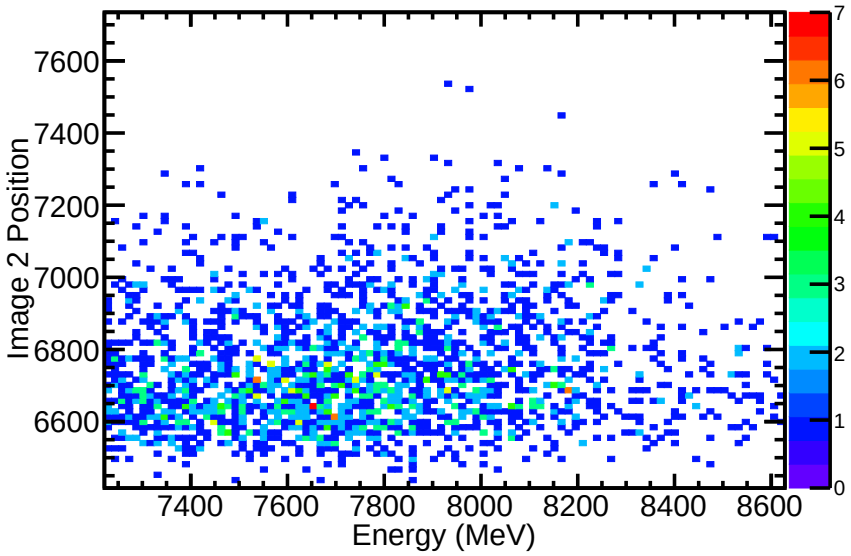

Figure 4.8 The TKE vs. the position of the ions within the Image 2 Scintillator that demonstrate the lack of separation of charge states shown only for the middle strips in the detector.

the two gates shown in Fig. 4.7. The total number of counts in each TKE gate from Fig. 4.7 is given for reference in Table 4.3. The observed number of counts at 126 keV and 378 keV are compared to the expected number of counts if there was no TKE separation (i.e. scaling the peaks in Fig. 4.10 by the percentage of ions in each TKE gate in Fig. 4.7). The peaks in the ^{118}Rh gate clearly do not have a linear scaling with the total counts within the gates, while those for the ^{115}Rh are much closer to the values expected by scaling.

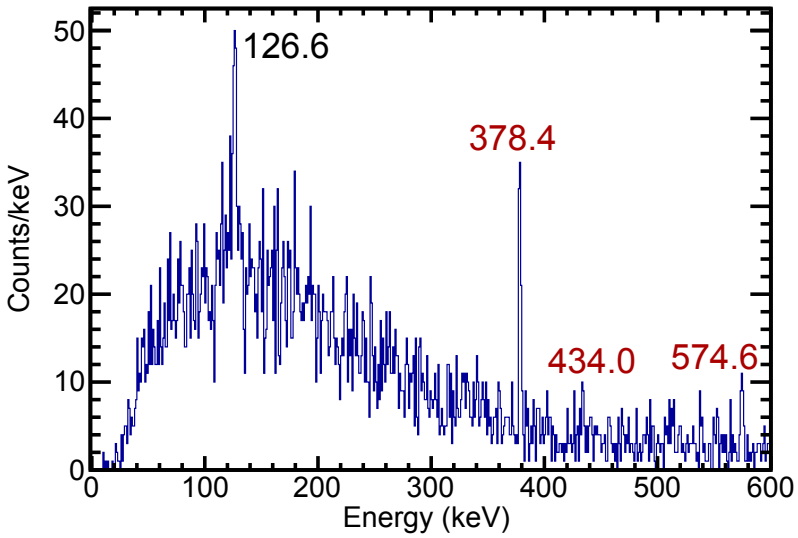

Figure 4.9 β-delayed γ-ray spectrum correlated with $^{115/118}$Rh. Previously identified ^{118}Rh γ rays [72,73] are labeled in red and previously identified ^{115}Rh γ rays [74] are labeled in black. The peak at 126 keV (^{115}Rh) is the sum of two very close in energy peaks at 125 and 127 keV (both ^{115}Rh), and the correlation time was 500 ms.

There are several additional ways the TKE measurement and the PID could be improved. Better energy resolution (lower radiation damage) would help increase separation between charge states. Secondly, less intervening material would also help the TKE measurement. With less material to pass through, the resulting width of the TKE deposited in the GeDSSD would be reduced as the result of decreased energy straggling. One way to accomplish this would be through the creation of a GeDSSD that can be attached directly to the beam line vacuum, eliminating the Al entrance window, Kapton window and air through which the ions must travel.

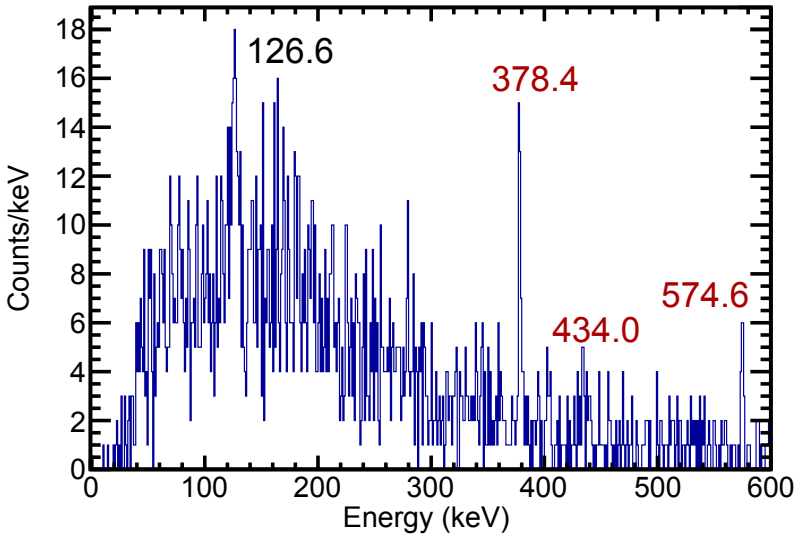

Figure 4.10 β-delayed γ-ray spectrum correlated with $^{115/118}$Rh and confined to the edge strips. γ rays populated by the decay of ^{118}Rh [72, 73] are labeled in red and γ rays from ^{115}Rh [74] are labeled in black. The peak at 126 keV (^{115}Rh) is the sum of two very close in energy peaks at 125 and 127 keV (both ^{115}Rh), and the correlation time was 500 ms.

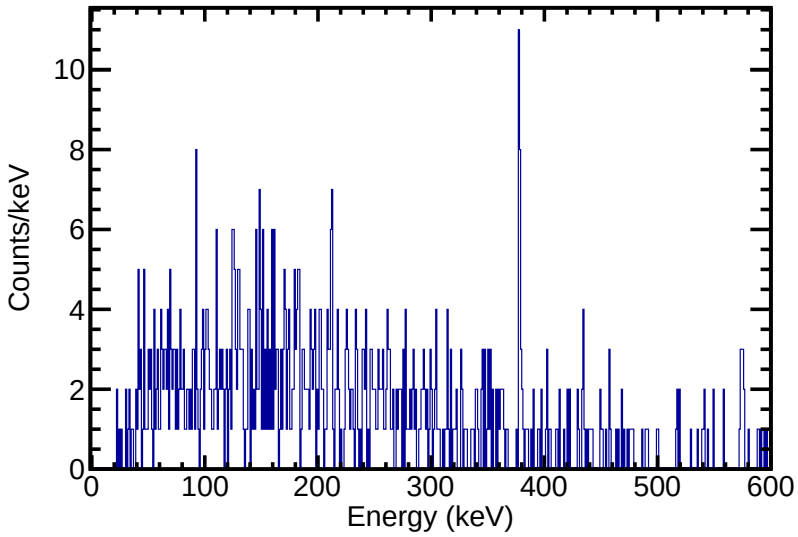

Figure 4.11 β-delayed γ-ray spectrum correlated with ^{118}Rh and confined to the edge strips. An additional requirement on the TKE of the ions expected to enhance the decays of ^{118}Rh was applied to the figure. See text for details.

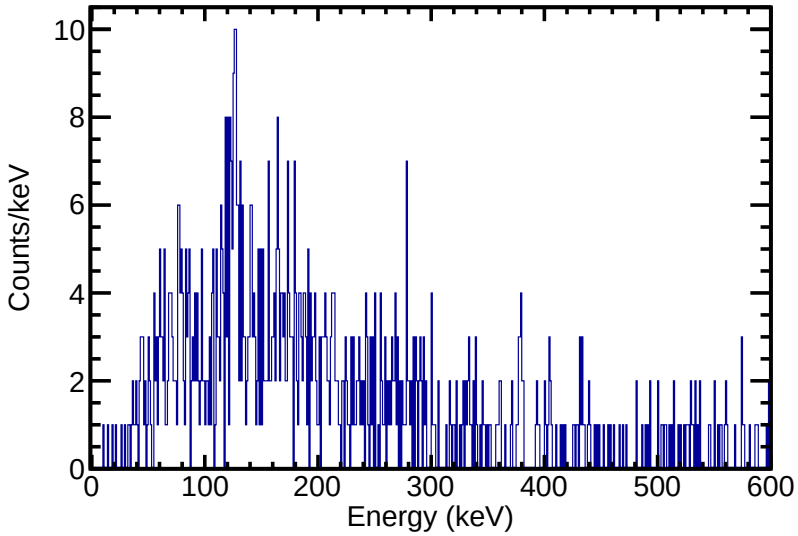

Figure 4.12 β-delayed γ-ray spectrum correlated with ^{115}Rh and confined to the edge strips. An additional requirement on the TKE of the ions expected to enhance the decays of ^{115}Rh was applied to the figure. See text for details.

Table 4.3 Observed counts for transitions in ^{115}Rh and ^{118}Rh decays compared to the expected number of counts if there were no TKE separation. The expected number of counts were determined by scaling the number of counts of each γ ray by the total number of implants for the number within each gate.

Gate	Total in TKE Gate	Number of Observed 126 keV Counts	Scaled 126 keV Counts	Number of Observed 378 keV Counts	Scaled 378 keV Counts
All Edge Events	4150	52±23	-	34±13	-
^{115}Rh (left)	1735	20±14	22±10	13±6	14±5
^{118}Rh (right)	1345	6±2	17±7	20±8	11±4

4.4 Ge calibration

The calibration and efficiency simulations of the GeDSSD were discussed in Section 3.3 for both the low-gain and high-gain strips in the detector, and the calibration and efficiency of the clover detectors used in experiment e11003 will be discussed in this section. Four clovers were placed upstream of the GeDSSD in a cross, four placed downstream in a second cross with the ninth detector placed at zero degrees downstream of the GeDSSD inside the square formed by the four other downstream clovers. A photograph of the setup is shown in Fig. 4.13. The upstream array was numbered 1-4, where clover 1 was located (facing upstream) at the 1 o'clock position with numbering increasing clockwise up to clover 4 at the 11 o'clock position. In the downstream ring (still facing upstream), clovers 5-8 were numbered similarly, starting with clover 5 in the 1 o'clock position and increasing in numbering clockwise to clover 8. Clover 9 was at the back of the array, in the center of the downstream group. There were two cryostat designs among the nine clover detectors. Clovers 1-5 and 8-9 had one cryostat design and clover 9 was used as a typical example. Clovers 6 and 7 were of a slightly different cryostat design, and clover 7 was used as a typical example. The nine clover detectors originated from the YRAST Ball array, for more information about the detectors please see Ref. [75].

4.4.1 Efficiency calibration

The efficiency of the clovers cannot be measured using a source at the ion implantation location within the GeDSSD. Therefore, data from a SRM source (here a $^{154/155}$Eu source, SRM 4275C-69.) was taken at several positions around the array as a whole, as well as near clovers 7 and 9 individually. The measured efficiencies were simulated and the simulation was matched to the data. Additionally, the effects of summing corrections were taken into account with the clover efficiency calibrations. These corrections account for any interference in measured counting rates due to the presence of other transitions, and are a factor to divide the measured efficiency. These corrections are tabulated below in Table 4.4 and are typically between 0.8 (as was the case with

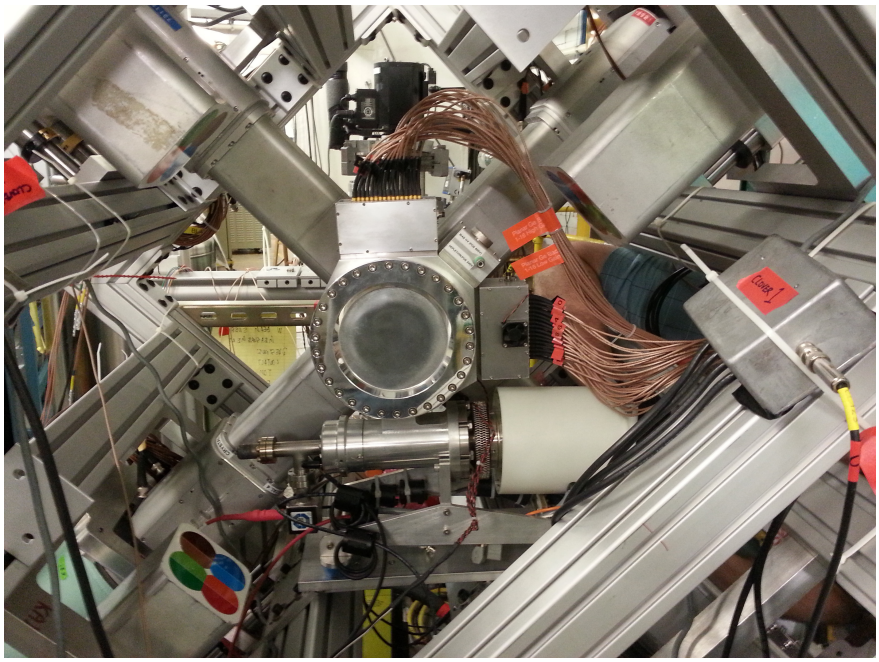

Figure 4.13 A photograph of the experimental setup with the downstream set of clovers pulled back to show the GeDSSD in front of the upstream cross. Beam exits the page toward the viewer. The ninth detector is place directly behind the GeDSSD at the center of the cross.

source positions on the sides of clover 9) and 1.

The SRM source was placed on the front face and on the side of clovers 7 and 9 for detailed comparisions to Geant4 simulations. The comparison between simulation and experiment when placing the source on the front face of the detectors is presented in Fig. 4.14. The simulation was slightly low at energies below 200 keV and this was likely due to more absorbing material present that is not in the detectors. However, removing some material worsens the match at higher energies, so the simulated cryostat thickness was chosen to balance the miss-match between low and high energies. Similarly, the match between simulation and experiment for a source placed on the side of the cryostat two inches from the front face of the detector is shown in Fig. 4.15 and Fig 4.16 for clover 9 and 7, respectively. These figures show a reasonable agreement between simulation and experiment at high energies which gradually gets worse at lower energies. The rest of the array was also simulated with the source position in front of clover 9 (Fig. 4.17)(a).

Since there are some deviations between the experiment and the simulation, an estimate of

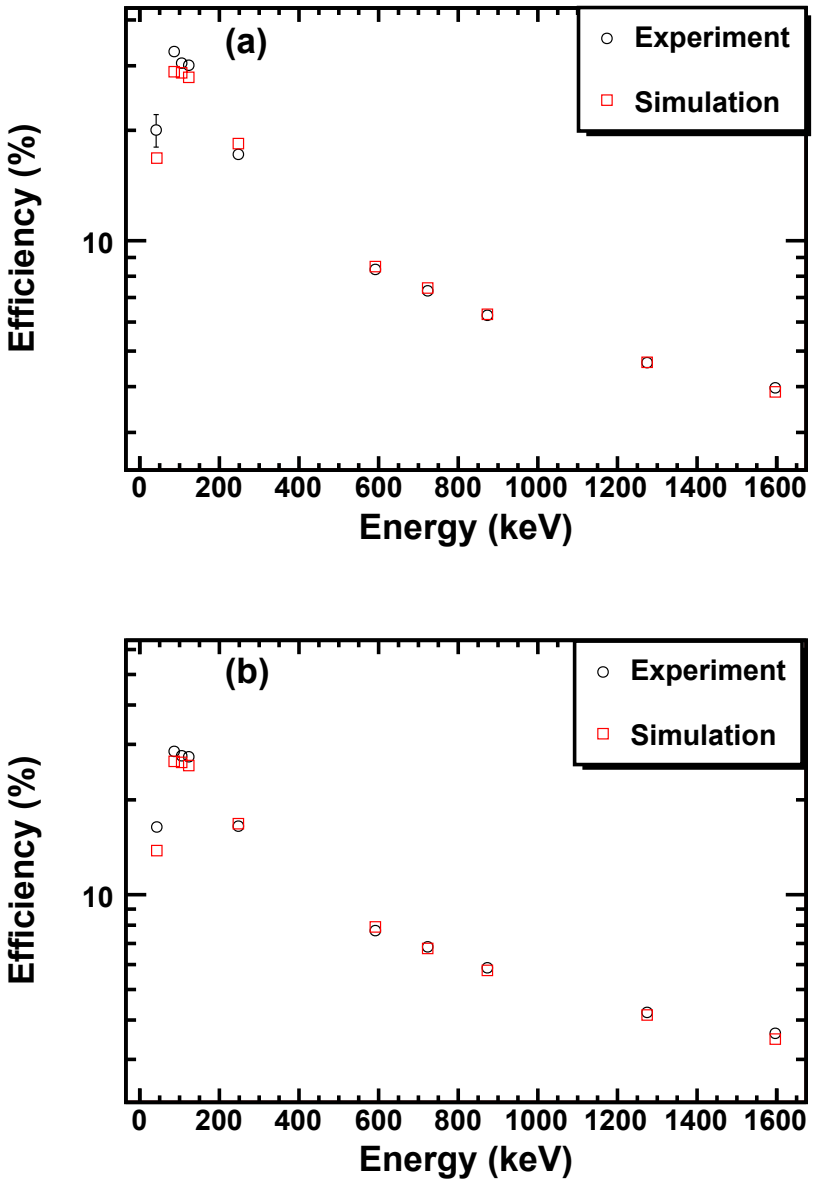

Figure 4.14 The comparison between experimentally determined (black circles) and simulated efficencies (red squares) from 0-1650 keV for a source placed on the front face of (a) clover 7 and (b) clover 9. The efficiency for each crystal within the clover detector was determined individually, and then the efficiencies from all four crystals were summed to give the efficiency in the figures.

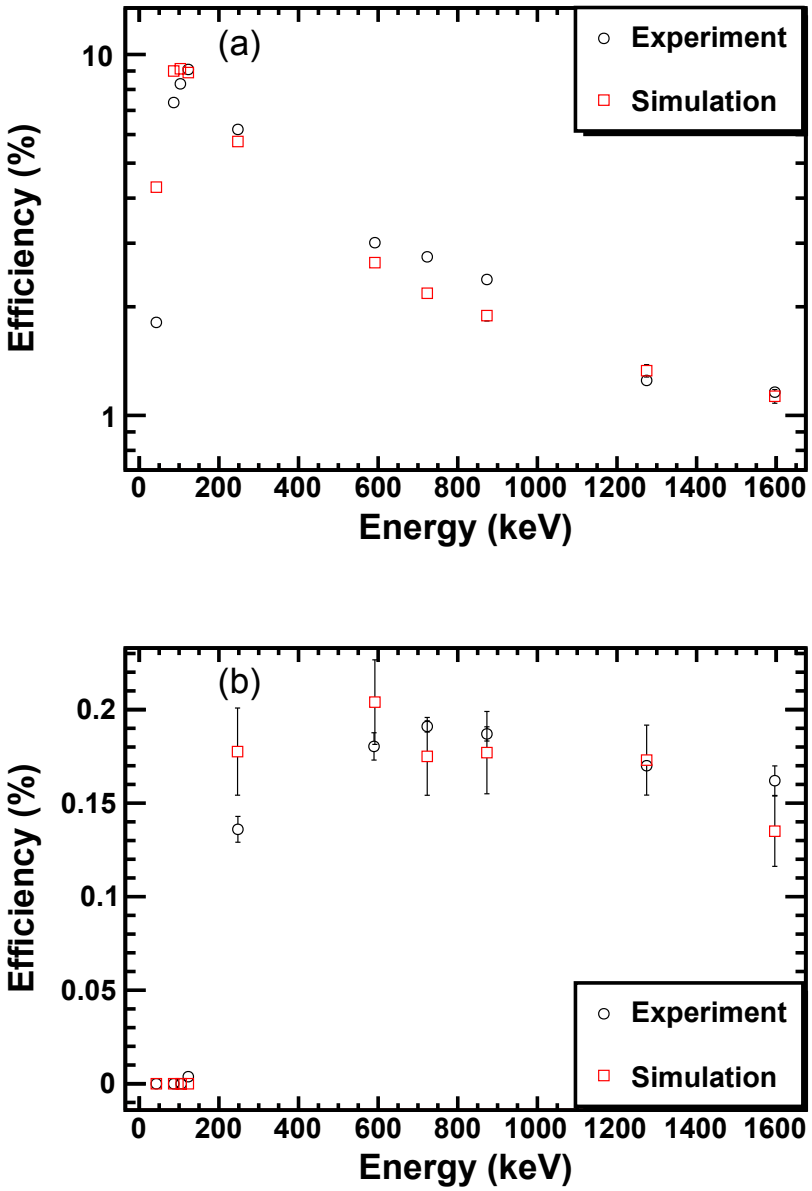

Figure 4.15 The comparison between experimentally measured (black circles) and simulated efficencies (red squares) for a source placed on the side of clover 9 for (a) a crystal closest to the source and (b) a crystal on the opposite side of the detector from the source.

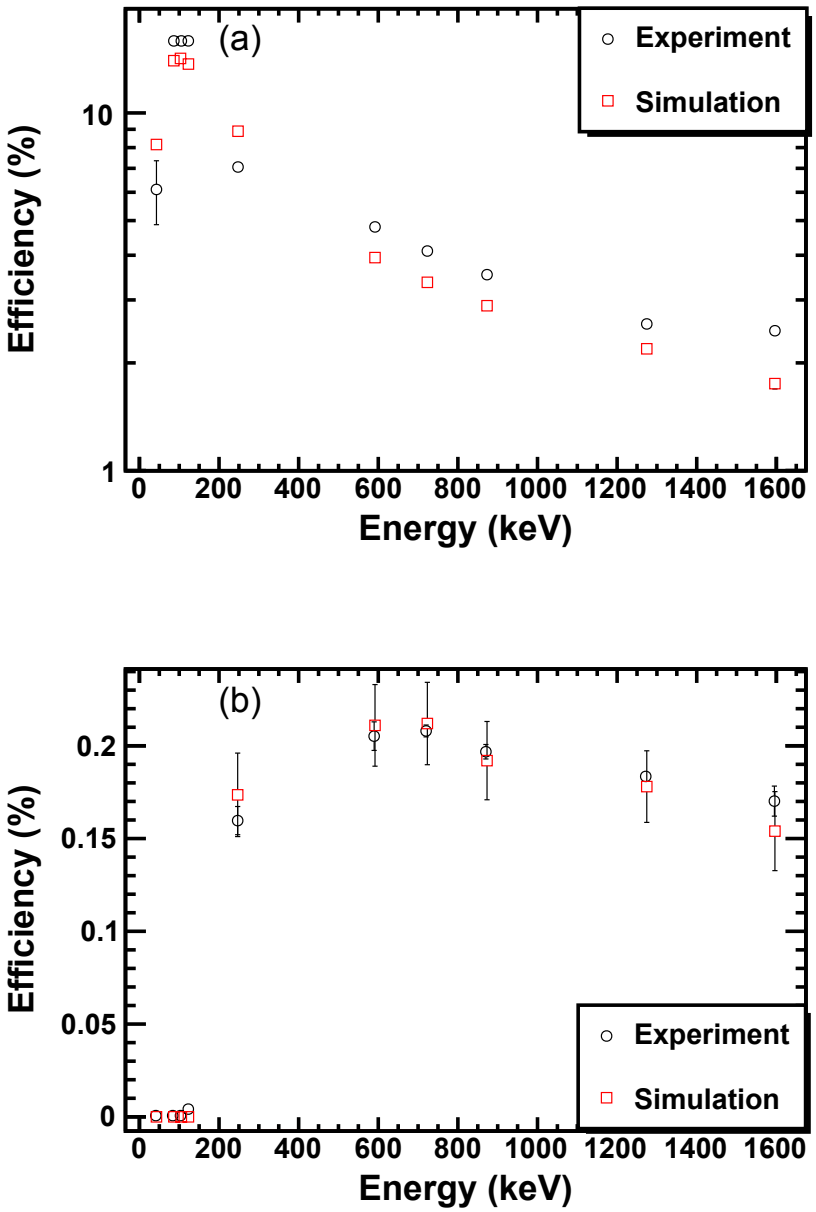

Figure 4.16 The comparison between experimentally determined (black circles) and simulationed efficiencies (red squares) for a source placed on the side of clover 7 for (a) a crystal closest to the source and (b) a crystal on the opposite side of the detector from the source.

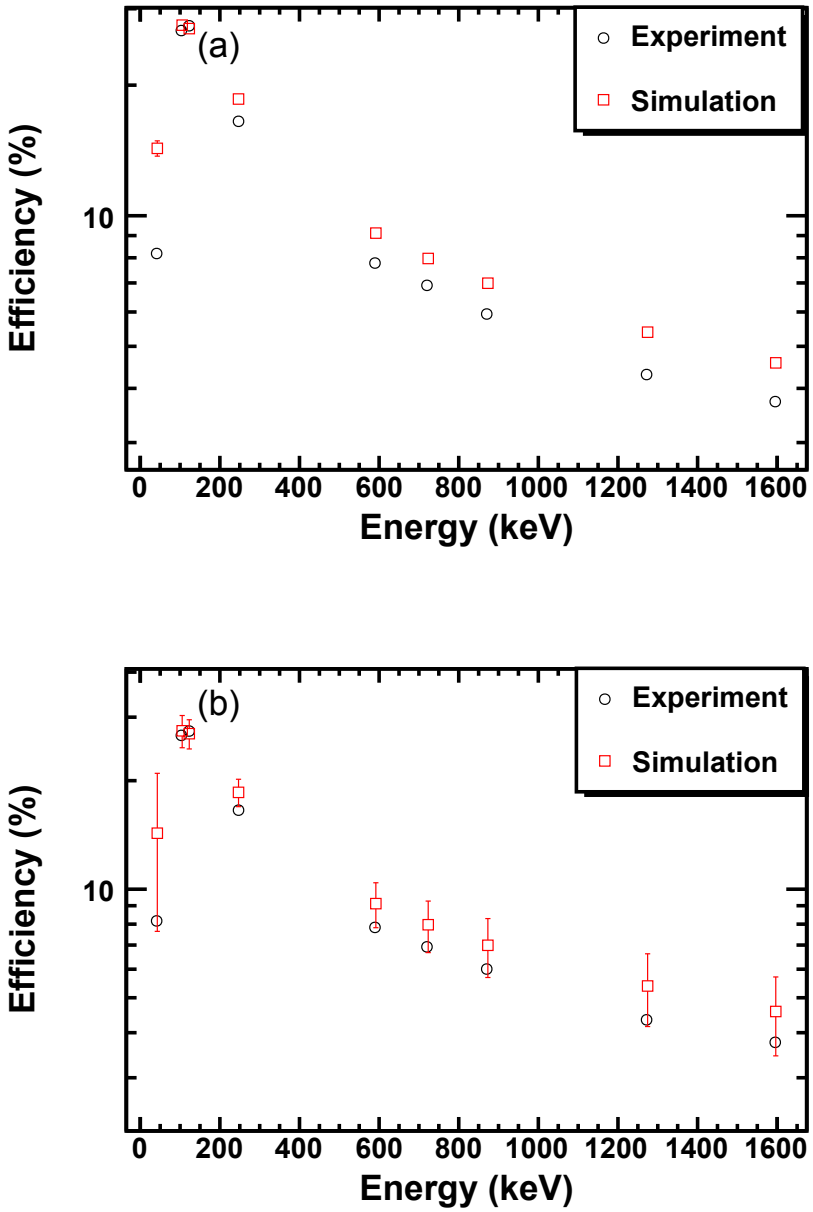

Figure 4.17 (a) The comparison between experimentally determined (black circles) and simulated efficiencies (red squares) for a source on the face of clover 9. The efficiencies shown are for the sum of the downstream clover ring using the fit error as the uncertainty. (b) The same plot as (a), including the degree of miss-match between simulation and clover within the uncertainty. See text for details. The efficiency for each crystal within the detectors was determined individually, and then the efficiencies of all crystals were added together to give the efficiency shown in the figures.

Table 4.4 Table of γ-ray efficiency summing corrections for the SRM source. [E] denotes the total efficiency at "E" keV (calculated from simulation), while {E} is the peak efficiency at "E" keV. Measured efficiencies are divided by the summing correction to account for the correction.

Energy (keV)	Summing Correction
42.8	1.0
86.6	1.0
105.3	1.0
123.1	1.0-0.072[248.0]-0.055[591.7]-0.120[723.3]-0.130[873.2] -0.20[1004.8]-0.401[1274.4]-0.02[1596.5]
247.7	1.0-0.287[42.8]-0.455[123.1]-0.134[591.7]-0.039[723.3]
591.8	1.0-0.297[42.8]-0.455[123.1]-0.178[248.0]-0.800[1004.8]
723.3	1.0-0.154[42.8]-0.243[123.1]-0.013[248.0]-0.518[873.2]-0.465[996.4]
873.2	(1.0-0.282[42.8]-0.455[123.1]-0.894[723.3]
996.3	(1.0+0.507{123.18}{73.2}/{996.4})(1.0-0.894[723.3])
1004.7	1.0-0.282[42.8]-0.455[123.1]-0.217[591.7]
1274.5	1.0-0.281[42.8]-0.455[123.1]
1596.4	(1.0+5.568{873.2}{723.3}/{1596.5}+2.094{1004.8}{591.7}/{1596.5}) (1.0-0.281[42.8]-0.455[123.1])

the error was made and added to the error from the fit of the simulation of the implantation location. For all source positions, the efficiency from simulation and experiment were summed for all crystals and the relative difference D was calculated:

$$D = \frac{e - s}{s} \tag{4.2}$$

where e is the experimental efficiency and s is the simulated value at a particular energy. For each energy, the largest disagreement between simulation and experiment from the 5 positions was selected, and these values were used to obtain an equation for the level of disagreement between simulation and experiment as a function of energy. Only the position in front of clover 9 had no energies with the greatest miss-match. The log of the average error was plotted against the log of the energy, and a third order polynomial was fit to the data. Thus, the expected miss-match between experiment and simulation may be calculated from the relationship determined by the fit:

$$log(Err) = -0.8474 \times log(E)^3 + 7.0819 \times log(E)^2 - 19.036 \times log(E) + 15.554 \tag{4.3}$$

where Err is the expected error, E is the energy of interest and the constants were determined by the this equation. Fig. 4.17(b) shows the comparison between simulation and experiment with the additional error from the miss-match between simulation and experiment for the simulated downstream clover ring.

Finally, the γ-ray efficiency for a source located at implantation depth within the GeDSSD was simulated. For experiment e11003, this depth was 1 mm into the GeDSSD, and the simulated source was a square the size of a pixel. Table 4.5 contains the efficiency for several energies, the uncertainty in the fit and the expected error between simulation and experiment from Eq. 4.3. The error from Eq. 4.3 is added in quadrature to the uncertainty from the results from a Gaussian fit of the peaks. The efficiency is shown in Fig. 4.18, with a fit to the simulation, and the bounds of the uncertainty of the simulation are shown. The efficiency of the clover detectors at an implantation depth of 1 mm may be represented with the following equation:

$$log(Eff) = -1.4214 \times log(E)^4 + 15.912 \times log(E)^3 - 66.456 \times log(E)^2 + 122.04 \times log(E) - 82.001 \quad (4.4)$$

where Eff is the efficiency, E is the energy and the constants were determined by the fit in Fig. 4.18.

Table 4.5 The simulated clover γ-Ray efficiency at implantation depth within the GeDSSD. The efficiencies of all individual crystals were calculated, and then summed together for the entire array to give the efficiency shown in the second column of the table.

Energy (keV)	Efficiency (%)	Fit Uncertainty (%)	Error (%)	Total Uncertainty (%)
50	0.513	0.0358	0.162	0.166
100	6.53	0.128	0.700	0.712
200	9.30	0.156	0.781	0.796
500	5.14	0.102	0.653	0.661
1000	3.33	0.0825	0.670	0.675
1500	2.55	0.0717	0.617	0.621
2000	2.03	0.0644	0.515	0.519

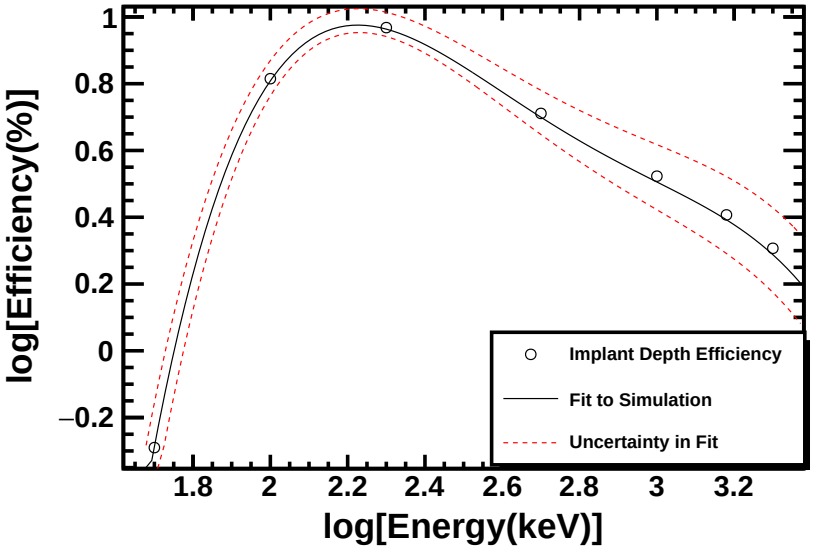

Figure 4.18 Simulated efficiencies within the clover detectors from the implant position of 1 mm deep into the GeDSSD. Also shown is the fit to those efficiencies and the uncertainty in the simulated efficiencies.

4.4.2 Energy calibration

The array was calibrated with respect to energy approximately every hour to measure any shifting detector gains over time. Occasionally, the calibration would shift within an hour for some of the detectors, those data files were calibrated more frequently for all detectors. Several background and source γ rays were used for the calibration: ^{212}Pb: 238.6 keV, ^{214}Bi: 609.3 keV, ^{60} Co: 1173 keV, 1332 keV, ^{40}K: 1460 keV. A quadratic calibration was used, where *clover* represents the number of the individual detector crystal being calibrated:

$$E(keV) = square[clover] \times E(ADCunits)^2 + slope[clover] \times E(ADCunits) + intercept[clover] \tag{4.5}$$

Typically, the value of $square[clover]$ was small, on the order of 10^{-7} to 10^{-9}.

The quality of the quadratic calibration is demonstrated by the residuals shown in Fig. 4.19 for the five calibration energies. The difference between the measured peak value after calibration and the expected value of the γ ray is plotted vs detector number. A value of 0 corresponds to an exact match. The figure includes data from all runs, where each run segment was calibrated individually,

and the total histogram from the entire time was fit at the end for the calibration results. For all calibration energies, the calibration is within 0.5 keV of the expected value.

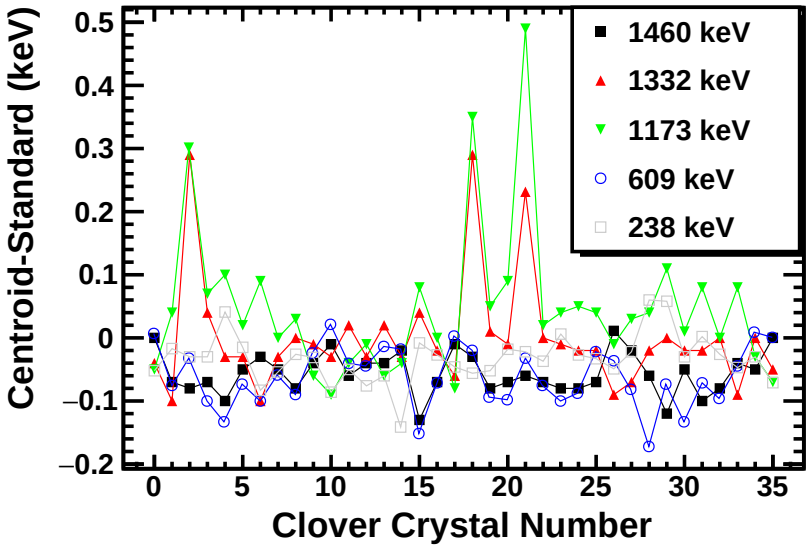

Figure 4.19 Energy residuals for 5 γ-ray transitions used for calibration, as a function of detector number. The data encompasses the entirety of the run time.

CHAPTER 5

RESULTS

5.1 Introduction

In this chapter, results from NSCL experiment e11003 will be presented and discussed. First, long-lived isomeric states analyzed through conversion electron spectroscopy will be detailed. The next section will focus on the results of the double-pulse processing analysis as introduced in Section 3.7, and the short-lived isomeric states found as a result of that analysis. Finally, β-delayed γ rays found in both the Ru and Nb beam settings will be presented.

5.2 Long-lived isomeric states

5.2.1 Introduction

Long-lived (millisecond) isomeric states can be correlated to the heavy ion from which they originated in much the same way as β-decay electrons. An isomer with an energy low enough that the emitted γ rays or conversion electrons would not leave the GeDSSD would appear as a peak in the GeDSSD energy spectrum. One such example is ^{115m}Ru. Previous work [5] found evidence of an isomeric state with a half-life of 76 ms and a γ-ray transition of 61.7 keV was associated with ^{115}Ru instead of the ^{115}Rh daughter. There were no coincident transitions observed with this γ ray. A conversion coefficient k_α=2.7$\pm$0.6 was determined for the 61.7-keV transition based upon the observation of the Ru k-shell X-rays and the assumption that all conversions were associated with the 61.7-keV transition; this indicated a mixed M1 and E2 character for the transition. The energies of Ru X-rays are given in Table 5.1.

The Weisskopf estimate for a 61.7-keV transition is too short compared to the known half-life and the authors of Ref. [5] suggest an unobserved γ ray depopulating the isomer and feeding the 61.7-keV level in ^{115}Ru. The half-life of the isomeric state could be consistent with a low energy

Table 5.1 Energies of Ru x-rays. In the table, Shell$_f$ denotes the final shell filled by the valence electron and Shell$_i$ denotes the initial valence shell. Values are from Ref. [76].

Shell$_f$	Shell$_i$	X-ray Energy (keV)
k	l_2	19.15
	l_3	19.28
	m_2	21.63
	m_3	21.66
	m_4	21.83
	m_5	21.83
	n_2	22.07
	n_3	22.07
	n_4	22.10
	n_5	22.10
l_1	m_2	2.741
	m_3	2.763
	n_2	3.181
	n_3	3.181
l_2	m_1	2.382
	m_4	2.683
	n_1	2.892
	n_4	2.965
l_3	m_1	2.253
	m_4	2.554
	m_5	2.559
	n_4	2.836
	n_5	2.838

M2 transition. The unobserved upper transition was placed with an energy 20 keV or less above the 61.7-keV transition, since it was assumed that all α_k X-rays were attributed to the 61.7-keV transition.

The $(3/2^+)$ ground state spin and parity of ^{115}Ru was chosen based on systematics of the other Ru isotopes and the β-feeding pattern into ^{115}Rh [12]. The spin and parities of the two excited states were chosen based on the M2 into an M1/E2 sequence along with systematics, tentatively placing an unobserved $(9/2^-)$ level below 82 keV.

5.2.2 Identifying ^{115}Ru

^{115}Ru was produced in both the second and third A1900 settings, in two different charge states (fully-stripped and H-like) in each setting. The PIDs for each setting are shown in Fig. 5.1, where the spots expected to contain ^{115}Ru are marked. The expected contaminants in the PID gates were ^{118}Ru^{44+} and ^{112}Ru^{43+}. This identification was confirmed by investigating the β-delayed γ-ray spectra, and searching for known daughter transitions. The summed β-delayed γ-ray spectrum for all four highlighted PID spots is shown in Fig. 5.2. A transition at 292.5 keV is clearly seen, which corresponds to the most intense Rh daughter γ ray [12].

5.2.3 Conversion electron spectroscopy

The decay energy spectrum observed in the GeDSSD correlated to ^{115}Ru implanted in the same or neighboring pixel and within 250 ms is shown in Fig. 5.3. A clear peak is seen at 123.8 keV and this peak appears in all ^{115}Ru gates and no others. Fig. 5.3 also shows a scaled background from the decay of ^{113}Tc, which was chosen since it was produced at a high rate and does not feed any known long-lived isomeric states, resulting in a spectrum which should be predominately due to β-decay electrons. The ^{113}Tc spectrum was scaled by 0.626 according to the ratio of ions delivered to the experimental system.

The relationship in time between the arrival of the ^{115}Ru ion at the experimental end-station, the 123.8-keV signal in the GeDSSD, and the β-delayed γ ray at 292.5 keV was explored. In Fig. 5.4(a), the β-delayed clover spectrum is shown for events occurring after the the arrival of a ^{115}Ru ion and before the 123.8-keV signal in the GeDSSD. The β-delayed γ ray at 292.5 keV was not apparent in the spectrum. In Fig. 5.4(b), the β-delayed clover spectrum is shown for events occurring after a 123.8-keV signal in the GeDSSD, up to 1 s after the ^{115}Ru implant. Both spectra could be measured for up to 1 s if a signal at 123.8 keV occurred very soon or very far after the ^{115}Rh implantation time. With such a range of the accumulation time, the number of counts of the ^{115}Rh daughter γ ray did not simply scale with the counting time. Since there was no evidence

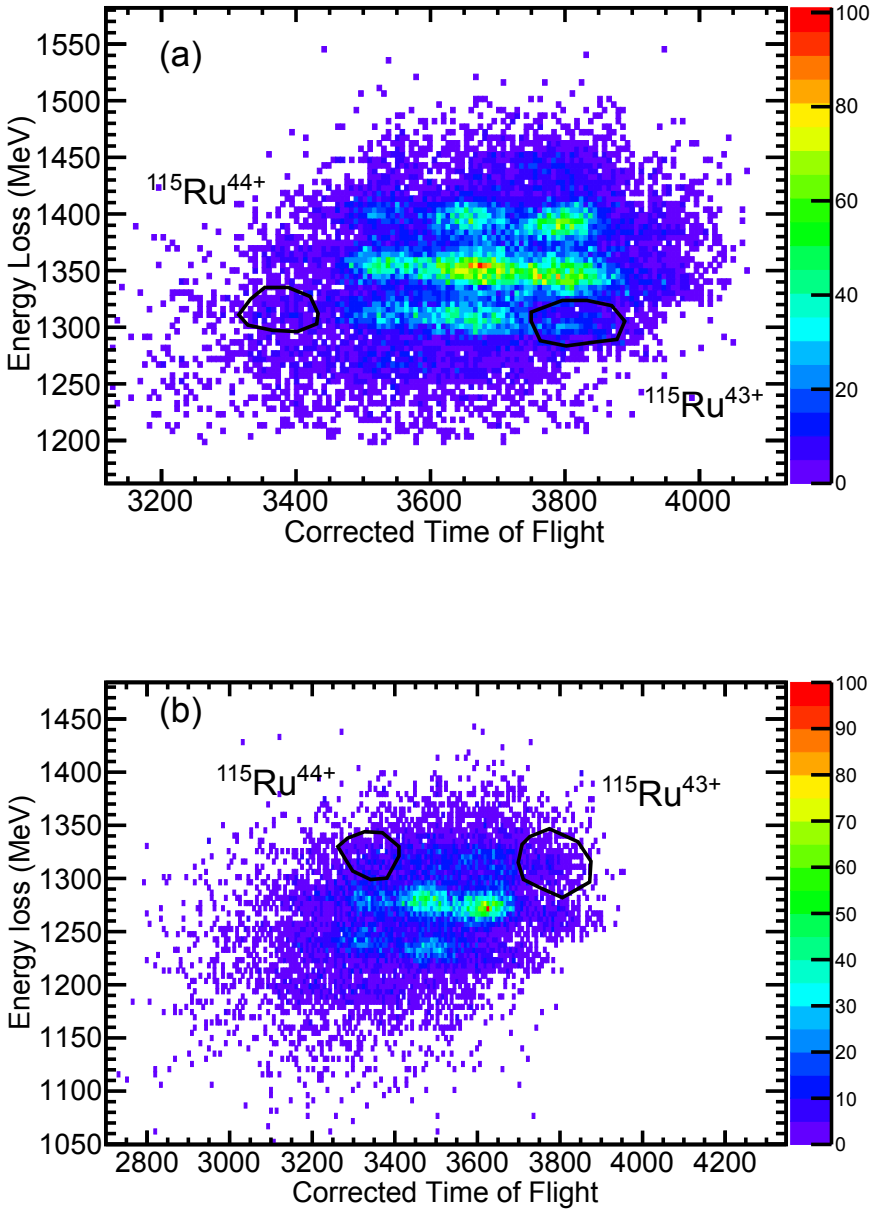

Figure 5.1 PID for (a) Ru setting and (b) Nb setting. The locations in the PID expected to contain ^{115}Ru are marked, along with their expected charge states.

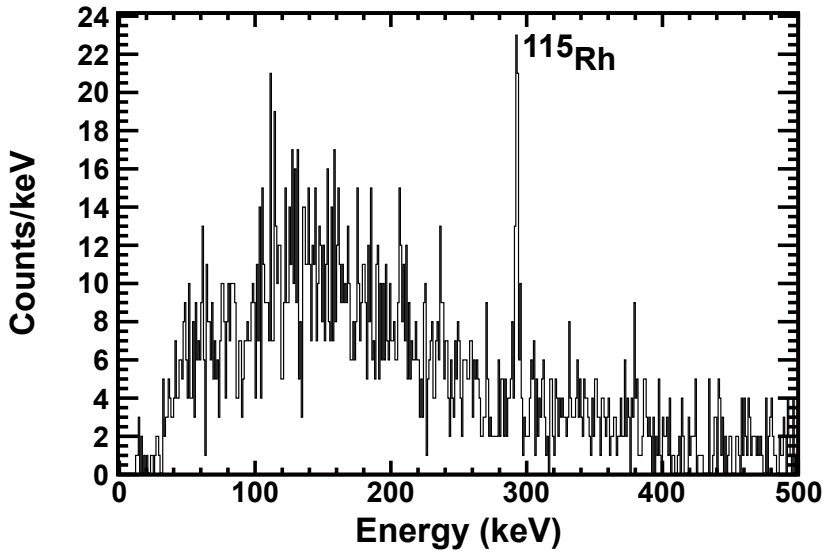

Figure 5.2 β-delayed γ ray energy spectrum for all events correlated to the decay of ^{115}Ru within 250 ms in both A1900 settings. The strong 292.5-keV transition associated with the β decay of ^{115}Ru is clearly seen.

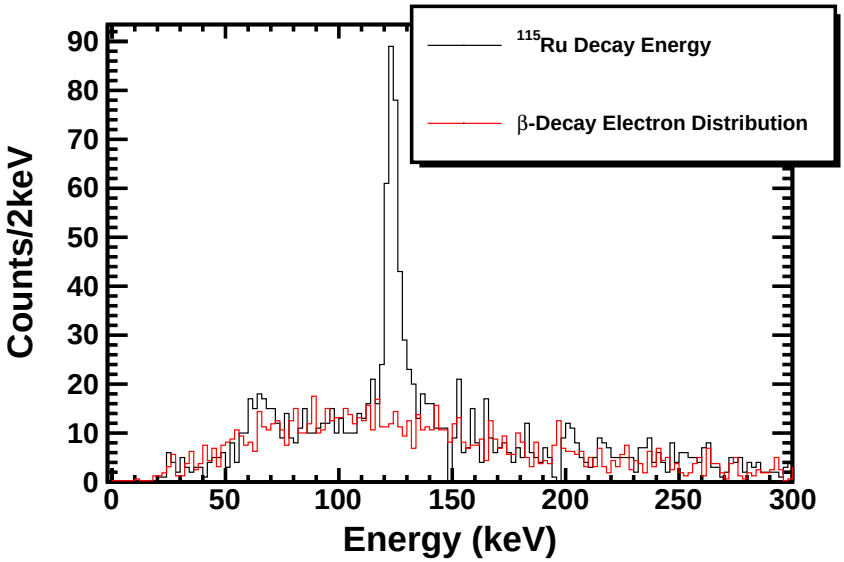

Figure 5.3 GeDSSD maximum strip energy spectrum following the implantation of ^{115}Ru (black), for a correlation field of 9 pixels. For comparison, a scaled spectrum of the β-decay electron distribution, taken from the β decay of ^{113}Tc, is superimposed (red).

of the β-delayed γ ray occurring before the 123.8-keV peak, this signal was associated with the ^{115}Ru parent rather than with the ^{115}Rh daughter, and could be the previously identified isomeric state.

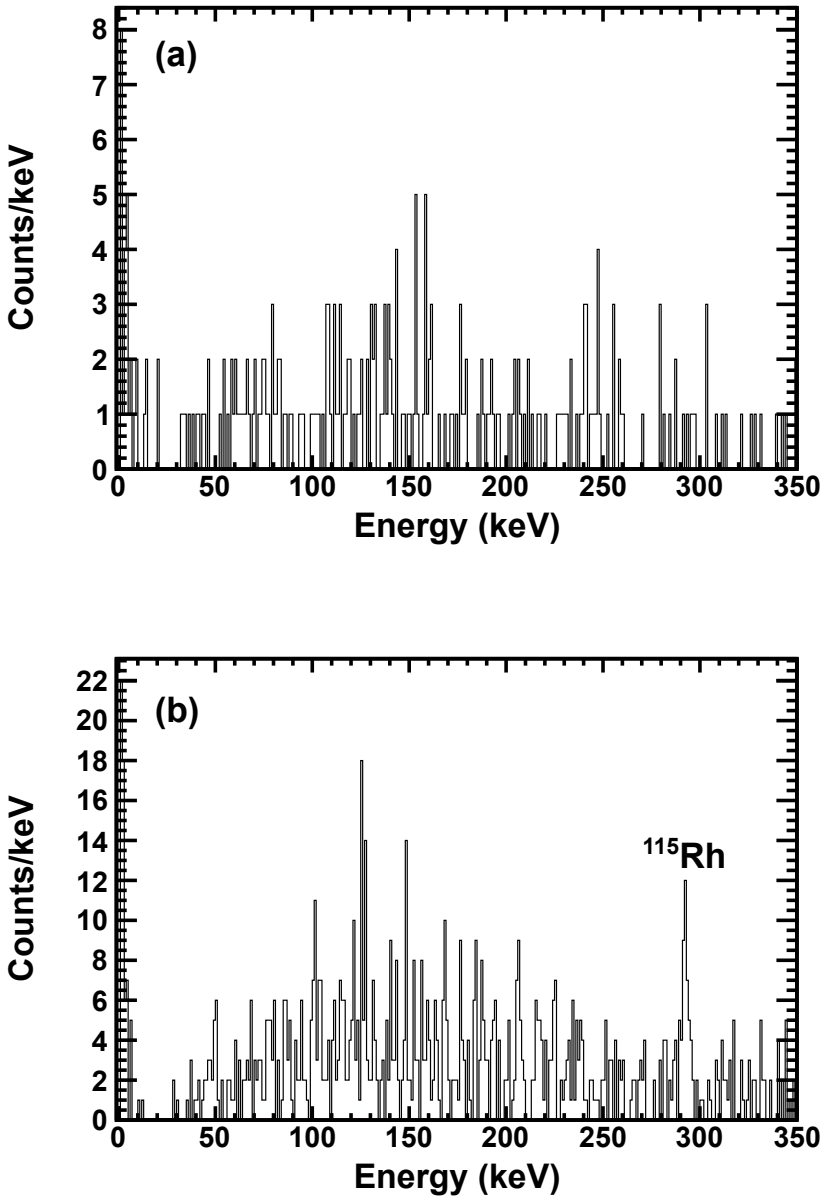

Figure 5.4 (a) β-delayed γ-ray energy spectrum occurring after the implantation of ^{115}Ru but before the 123.8-keV signal in the GeDSSD. (b) Events occurring after the 123.8-keV signal in the GeDSSD up to 1 s after the ^{115}Ru implant.

Fig. 5.5(a) shows the GeDSSD energy spectrum of decay events occurring in the same pixel

as the ^{115}Ru implant. With a smaller contribution from the β-decay electron, a second, smaller peak at 62 keV became apparent. Fig. 5.5(b) shows the GeDSSD energy spectrum for the 8 pixels surrounding the ^{115}Ru ion. Due to high efficiency for electrons and γ rays at low energies in the GeDSSD, it was not immediately obvious if the peak at 123.8 keV is a single transition or the sum of two separate transitions at 61.7 and 62.1 keV. The efficiency of detecting an isolated 123.8-keV γ ray in its initial pixel was 24.2$\pm$0.2%, and 20.2$\pm$0.2% for the neighboring pixels (see Section 3.4). Therefore, if the 123.8-keV signal were due to an isolated γ ray transition, 215$\pm$24 counts should have been present in Fig. 5.5(b). If the peak at 123.8 keV were from a single conversion electron, Table 5.2 gives the number of γ rays that would be expected for various multipolarities. For the peak to be a single conversion electron, the multipolarity would have to have a conversion coefficient greater than that of an E3 transition to be larger than that of the current data set, and most likely larger than E5 or M5 for the previous results to have observed none of the competing 123.8 keV γ ray.

Table 5.2 Number of expected γ rays to be detected if the peak at 123.8 keV were a single conversion electron transition given the total number of observed counts and detector efficiency.

Multipolarity	α_{tot}	Number of γ Rays
E1	0.07516	164
M1	0,1710	126
E2	0.6037	62
M2	1.474	30
E3	4.674	11
M3	11,411	4
E4	41.26	1
M4	91.74	0.6
E5	407.7	0.1
M5	775.8	0.07

More likely, the 123.8-keV peak corresponded to the detection of both the previously observed 61.7-keV transition and a new 62.1-keV transitions, thus the peak at $\sim$62 keV was due to events where one of the transitions escaped its initial pixel in the GeDSSD. γ rays at 62 keV in Ge are

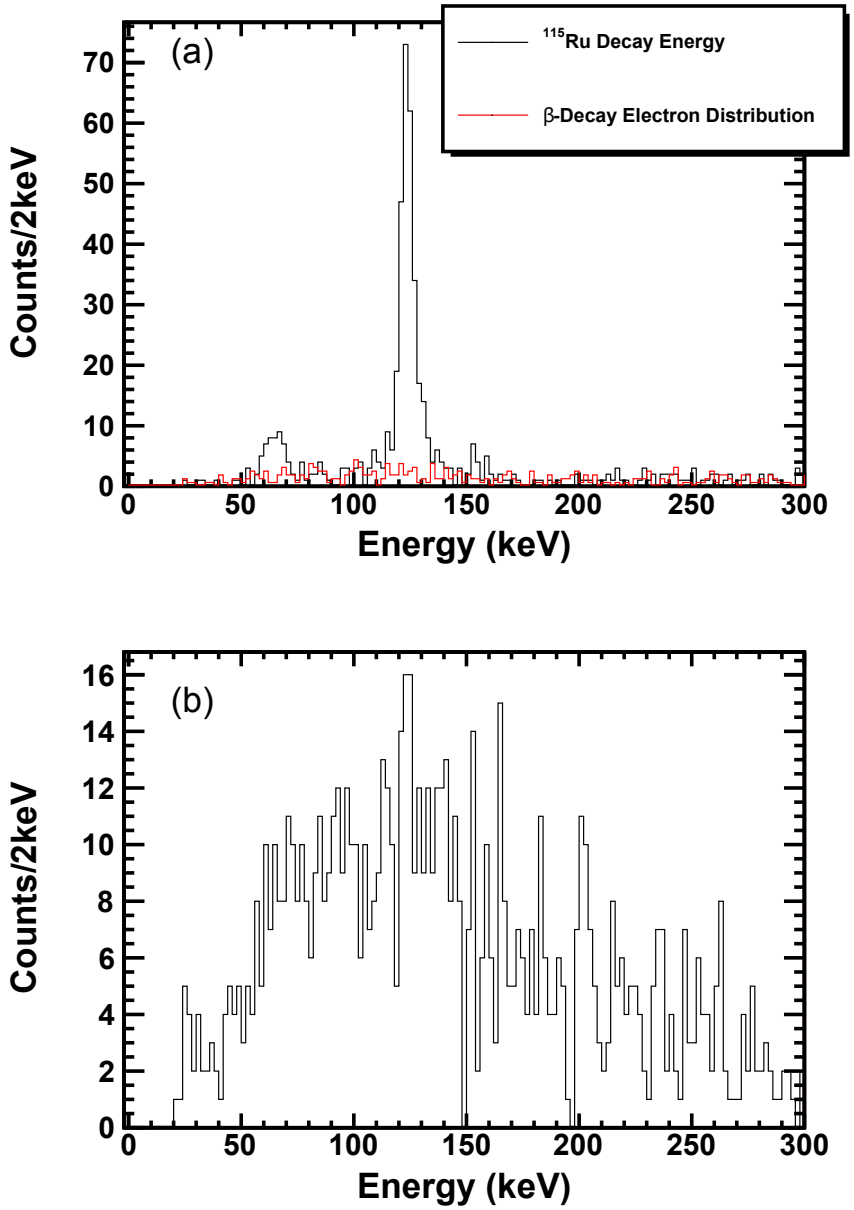

Figure 5.5 (a) ^{115}Ru decay events observed in the GeDSSD within the same pixel as the ^{115}Ru ion within 250 ms. (b) ^{115}Ru decay events in an adjacent GeDSSD pixel to the ion within the same correlation time as (a).

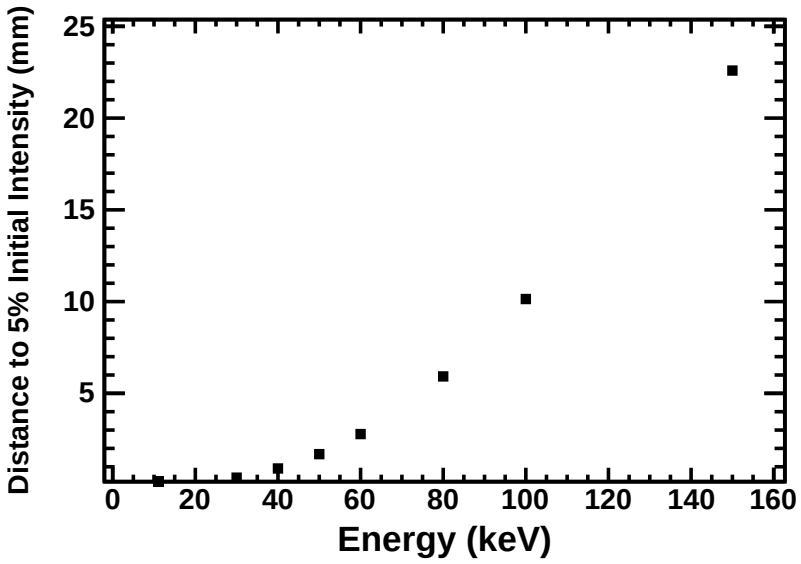

Figure 5.6 The distance low energy γ rays travel in Ge to have 5% of their initial intensity remaining.

unlikely to travel beyond the pixel of origin before interacting, as is demonstrated by the simulated GeDSSD efficiency. For example, the distance γ rays must travel to have 5% of their initial intensity remaining, shown in Fig. 5.6, is given by the exponential function:

$$Range = \frac{I_0}{I} = 0.05 = e^{-\mu x} \tag{5.1}$$

where I_0 and I are the initial and final intensities, x is the thickness of the material and μ is the total linear absorption coefficient. For Ge, the mass attenuation coefficient, μ/ρ, is given in tables published by NIST [77]. Given the density of Ge, 5.32 g/cm^3, the linear absorption coefficient as a function of energy can be calculated. Similarly, conversion electrons resulting from transitions near 62 keV are even less likely travel outside of a single pixel. Fig. 5.7 shows the range of electrons in Ge [78] as a function of their energy.

The decay curve in coincidence with the 123.8-keV peak in Fig. 5.5(a) is shown in Fig. 5.8. The decay curve was fit with a single exponential and constant background resulting in a half-life of 85(13) ms, which was consistent with the literature half-life value of 76(6) ms for the isomeric state in ^{115}Ru [5]. An isomeric half-life on this order would not be expected to appear in spectra

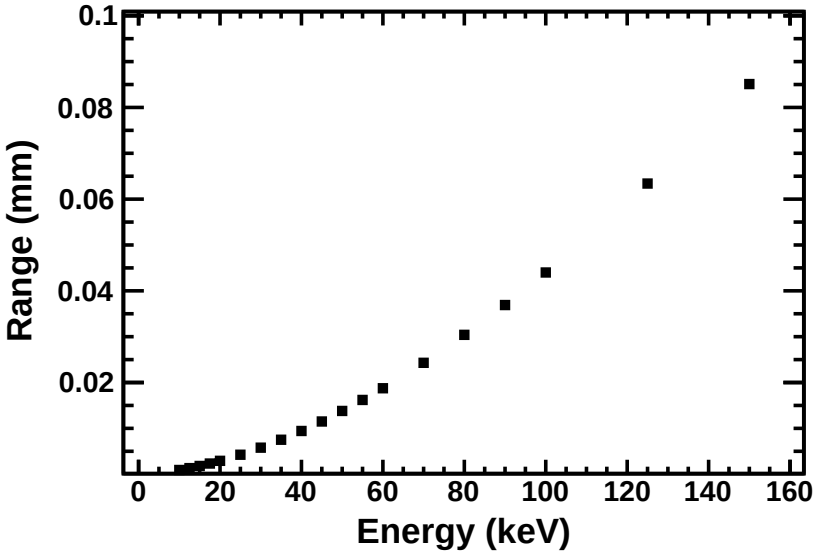

Figure 5.7 The range of low energy electrons in Ge. Strip width is 5 mm and the crystal is 1 cm thick.

created by the double-pulse processing technique as the half-life is too long (see sections 5.3.1 and 5.3.2).

5.2.4 Interpretation

The previous results for the ^{115}Ru isomer reported a ground-state with a tentative spin and parity of ($3/2^+$), with excited states of spin and parity of ($5/2^+$) and ($9/2^-$), with the ($9/2^-$) at an unknown excitation energy. The present results placed the isomeric state in ^{115}Ru at 123.8 keV, see Fig. 5.9. This discrepancy from the previous results can be reconciled. First, two transitions less than a 1 keV apart in energy can be difficult to resolve. In the previous work, the FWHM of the peak at 61.7 keV was on the order of 1-2 keV. In the present experiment the resolution was about 1.5 keV at 62 keV. Second, if the upper transition is highly converted, as would be expected for a high multipolarity, high-Z, low-energy transition, few γ rays would be emitted.

Assuming the previous spins and parities were correct, if the isomer were to transition directly to the ground-state, the multipolarity of the resulting 123.8-keV transition would be E3. Based upon Weisskopf estimates (Table 5.3 [79]), the branching ratio of the E3 transition relative to the

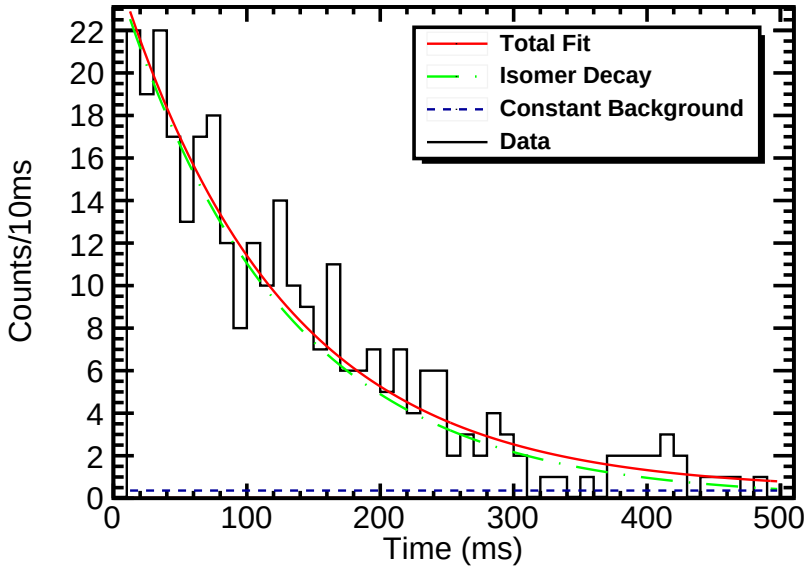

Figure 5.8 Decay curve in coincidence with the 123.8-keV signal in the GeDSSD following the decay of ^{115}Ru. The fit includes an exponential parent decay (green), and a constant background (blue) resulting in a half-life of 85(13) ms. The total fit is shown in red.

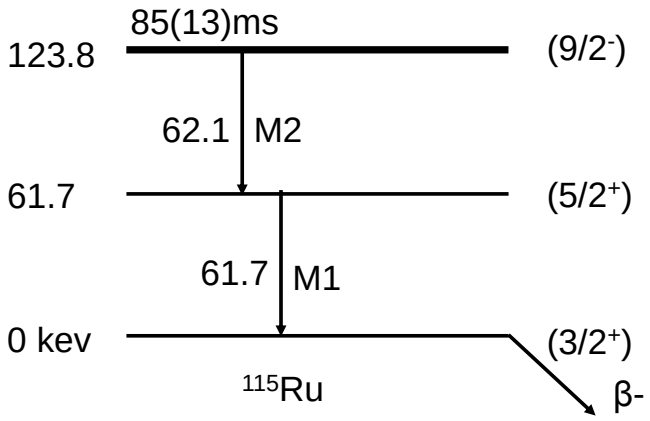

Figure 5.9 The level scheme for ^{115}Ru as suggested by this work.

M2 transition would be on the order of 10^{-5} and therefore unlikely to be observed. The previous non-observation [5] of a γ ray at 123.8 keV with orders of magnitude more statistics than the present results is in agreement with this interpretation, suggesting that this pathway (E3 single transition to the ground state) was unable to compete with the M2 transition to the 61.7 keV $5/2^+$ state and subsequent cascade to the ground-state.

Table 5.3 Multipolarities of the transitions discussed in the analysis of ^{115}Ru. The conversion coefficients in the table have an uncertainty of 1.4% [79].

Energy (keV)	Multipolarity	α_{tot}	Weisskopf λ	Weisskopf $T_{1/2}$ (ms)
61.7	M1	1.223	7.4×10^{9}	9.4×10^{-8}
62.1	M2	19.23	1.2×10^{4}	1.4
123.8	E3	4.674	2.0×10^{-1}	3.5×10^{3}

The conversion coefficient for a 62.1-keV M2 transition is 19.23, so most of the isomeric decays proceeded through electron emission. The detection efficiency of the GeDSSD for electrons of this energy was $\sim$100%. Since the energies from all X-rays regardless of electronic shell are low in energy, and therefore unable to travel farther than a single strip, X-ray emission from different shells (for example the k or l shells) would all result in a peak summing to $\sim$62 keV. The subsequent 61.7-keV γ ray would be detected in either the same or neighboring pixels of the GeDSSD, with a small amount escaping and possibly depositing its energy in the clover detectors. If the 61.7-keV γ ray escaped the pixel containing the ^{115}Ru ion, only the first transition would be observed, leading to the low energy peak observed in the GeDSSD and possible coincident γ ray detection in the clover detectors. Together with the consideration of the GeDSSD's detector response, the observed peak at 123.8 keV was likely not a single transition, but the sum of two transitions similar in energy, comprising of the sum of the energies of conversion electrons, X-rays, and γ rays.

Another competing process is the emission of Auger electrons. For Ru, the fluorescence yields for the k and l shells are approximately 0.82 and 0.02, respectively [39]. Thus, internal conversions from the k-shell will result in the emission of X-rays the majority of the time, while internal

conversions from the l-shell will result in the emission of Auger electrons most of the time. However, since these low-energy emissions will travel very short distances in the GeDSSD, the energies from any emitted Auger electrons will sum with the conversion electron, again yeilding detected energies of $\sim$62 keV.

Given the conversion coefficients, detector efficiencies (from a distributed source in simulation), and the number of counts in the GeDSSD, the expected number of coincident $\sim$62-keV γ rays in the clover detectors was calculated. In the GeDSSD single pixel energy spectrum (Fig. 5.5(a)), there were 258$\pm$29 counts in the peak at 123.8 keV and 44$\pm$14 counts within the smaller peak at 62 keV (representing events where one transition escaped the initial pixel) giving a total of 302$\pm$32 isomeric decays, assuming all cascades led to counts in one of the two peaks, which was reasonable given the near 100% efficiency of the GeDSSD at these energies. To find the total number of escaping γ rays (and thus with the efficiency of the clover detectors, determine the expected number of counts in the clover spectrum), the following system of equations may be solved:

$$1.223 = \frac{N_{61.7e}}{N_{61.7\gamma}} \tag{5.2}$$

$$19.23 = \frac{N_{62.1e}}{N_{62.1\gamma}} \tag{5.3}$$

$$N_{62.1e} + N_{62.1\gamma} = N_{61.7e} + N_{61.7\gamma} = 302 \tag{5.4}$$

in which 302 is the total number of cascades, and N is the number of emitted particles of a specific energy and type. Eq. 5.2, and 5.3 are the conversion coefficients from Table 5.3. Finally, Eq. 5.4 states that since the two transitions are in a cascade, the total number of counts from each transition should be equal. Solving, one finds $N_{62.1\gamma} = 15$ and $N_{61.7\gamma} = 136$. Combined with the clover array efficiency of 1.58$\pm$0.71%, 2 62-keV γ rays were expected compared with the experimental spectrum shown in Fig. 5.10.

Taking everything together, the level scheme shown in Fig. 5.9 is suggested. In comparison to the the Weisskopf estimate, the experimental half-life is hindered by more than an order of magnitude. Fig. 5.11 compares the experimental decay constant to the Weisskopf estimate for

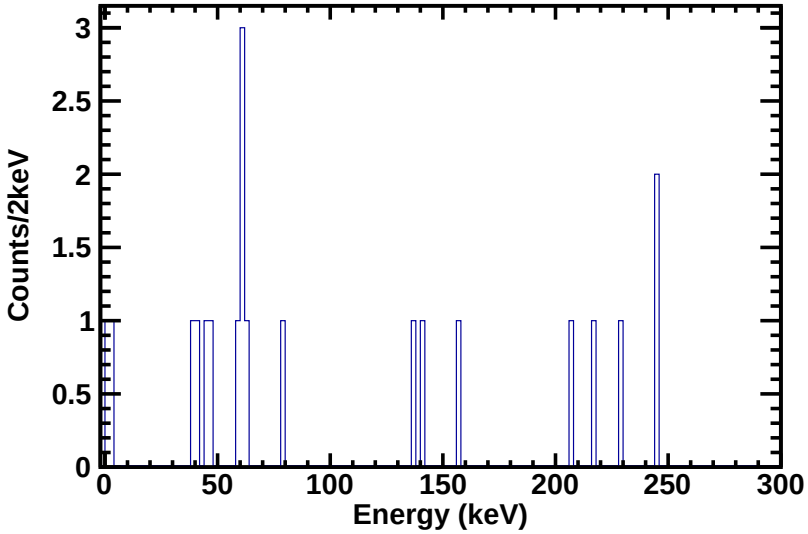

Figure 5.10 Clover energy spectrum in coincidence with the ∼62-keV peak in the single pixel GeDSSD spectrum (Fig. 5.5(a).

several M2 transitions in the A∼115 region, including a transition in stable ^{115}Sn, where the match is quite good. For all other nuclei, the Weisskopf estimate is hindered by a minimum of one order of magnitude.

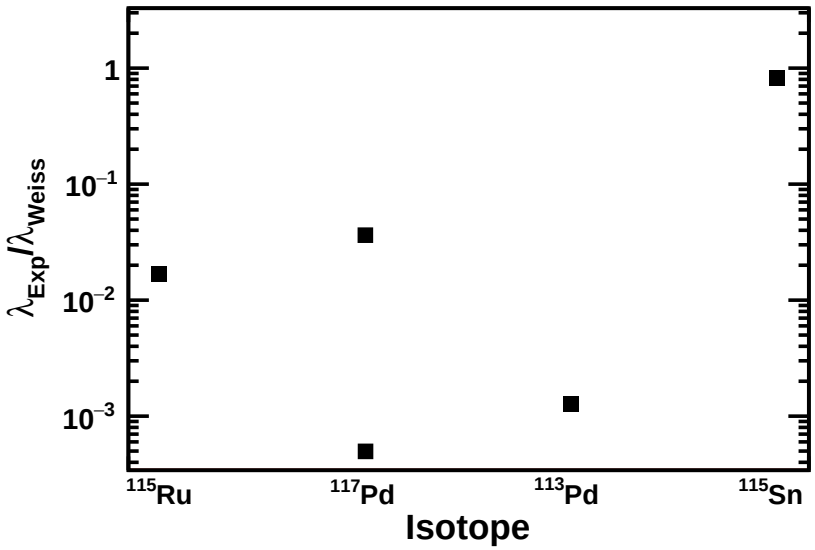

Figure 5.11 The ratio of experimentally observed [3,9,80,81] (λ_{exp}) to Weisskopf estimate (λ_{Weiss}) for the decay constants of some isomeric M2 transitions near A∼115.

Additionally, with a second, unobserved γ-ray transition in the previous work, the number of k_α X-rays associated with the 61.7-keV transition would decrease, with some of the previously observed X-rays corresponding to the unobserved, highly converted 62.1-keV transition. Thus, the multipolarity of the 61.7 keV should be shifted from a mixed M1 and E2 transition closer to a pure M1 transition. The spins and parities were left the same here as in the previous work. The upper transition has an updated energy, from an unknown energy less than 20 keV to 62.1 keV, and the lower transition's multipolarity was updated from a mixed M1 and E2 transition to M1.

5.2.5 Simulation

Finally, this decay may be simulated in Geant4 to verify that the above assumptions and interpretations can produce a spectrum consistent with the observed signals. A ^{115}Ru nucleus with two levels and two allowed γ rays without subsequent β decay was input to the simulation at a depth of 1 mm into the crystal. The simulated GeDSSD energy spectrum is compared to that of experiment in Fig. 5.12. There seems to be slightly less of the single transition near 62 keV in the simulation compared to experiment, with 14$\pm$5 counts. In simulation, there were 285$\pm$25 counts within the 123.8-keV peak, which was consistent within the uncertainties in the experimental data. Additionally, there appeared to be a similar number of 62-keV transitions in the clover histograms as well (Fig. 5.13). Modifying the parameters of the simulated levels to allow the 61.7-keV transition to have E2 or mixed M1+E2 character resulted in a reduction in counts in the 62-keV peak in the GeDSSD spectrum. A simulated 61.7-keV E1 transition did not result in any appreciable difference in the simulated spectrum. The simulated $\sim$20 keV Ru k-shell X-rays sum with their corresponding conversion electrons, matching that seen in the experiment to create only two peaks within the GeDSSD.

There was no peak in simulation in the neighboring strips at 123.8 keV. Furthermore, changing the level scheme in the simulation to allow for a competing 123.8-keV branch did not introduce a peak in the neighboring strips, nor did any other changes to the simulated level scheme introduce a signal in the neighboring strips.

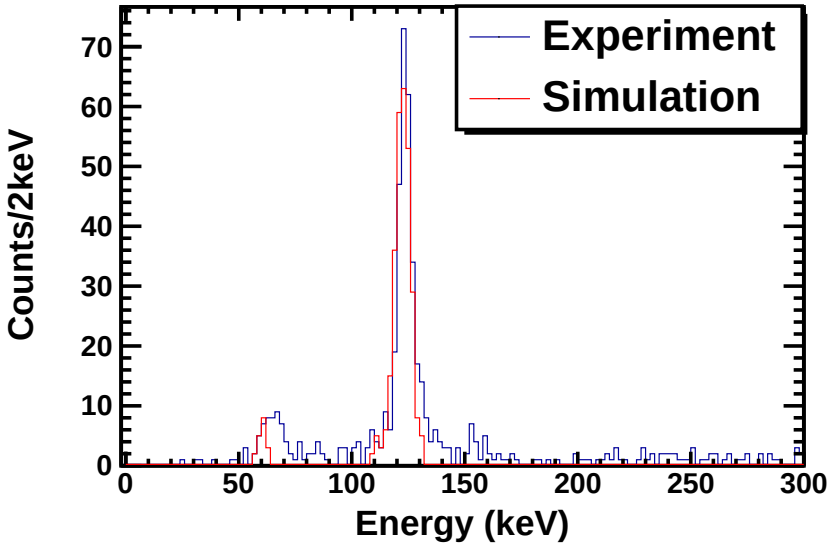

Figure 5.12 Comparison of the simulated strip spectra (red) of the decay of the isomeric state in ^{115}Ru and the experimental spectra (blue).

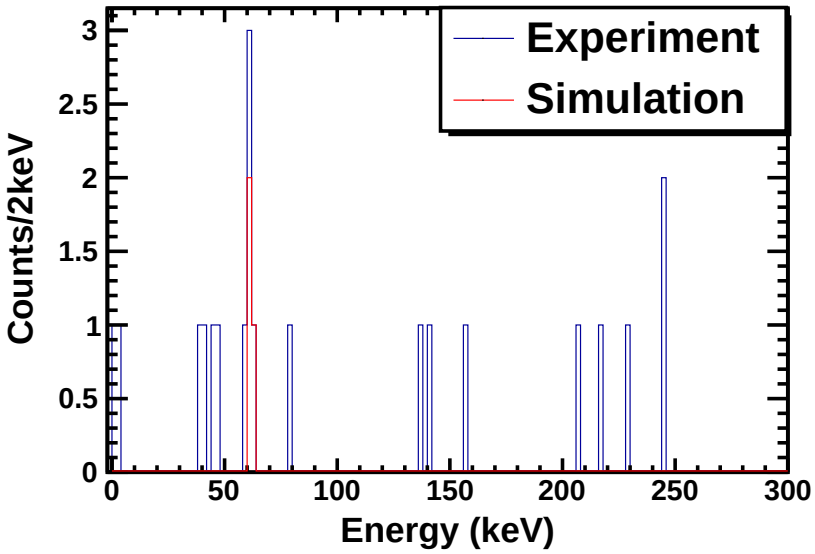

Figure 5.13 Comparison of the simulated spectra (red) of the decay of the isomeric state in ^{115}Ru and the experimental spectra (blue) for the coincident clover energy depositions.

5.2.6 Concluding remarks

To conclude, the experimental data and simulated results both supported the updated level scheme shown in Fig. 5.9. The upper transition has an energy of 62.1 keV, keeping the previous M2 multipolarity. The 61.7-keV transition multipolarity is changed from an M1/E2 mixed transition closer to a pure M1 transition. The transition from the isomeric 123.8-keV state is not able to compete with the other deexcitation pathway, and thus the E3 crossover transition is not observed.

5.3 Short-lived isomeric states

The double-pulse analysis discussed in Section 3.7 can be carried out on the data from both the Ru and Nb settings to search for short-lived isomeric states. This section will discuss the short-lived isomeric states found in these two beam settings. The data shown were from the analysis of the back strips in the GeDSSD because the back strips had fewer single- and noisy-pulses mixed in with the passing double-pulses compared to the front strips.

5.3.1 Double-pulses in Ru setting

Fig. 5.14 shows the energy spectrum of all signals identified as the second-pulse in the characteristic double-pulse-shape (see Section 3.7). Two peaks were clearly present in this energy spectrum at 49.3$\pm$3.6 and 155.7$\pm$4.1 keV (Fig. 5.14), while there were no apparent peaks in the histogram of the first-pulse energies (Fig. 5.15). Very few counts existed in the second-pulse spectrum above 500 keV. This did not appear to be due to large amplitudes of the first-pulse filling most of the ADC range, artificially constraining the energy range for the second-pulse. Higher energy pulses that would saturate the ADC simply do not appear to exist. Note that based upon the assigned transitions, there could be up to a 4-keV offset in the peak energies.

The γ ray spectrum observed in the clover detectors in coincidence with the 49.3-keV peak in the second-pulse energies is shown in Fig. 5.16. There were a few counts near 124, 223, and 380 keV. In ^{118}Ag [83], there exist 125.4 and 379.7-keV transitions in coincidence with the 45.8-

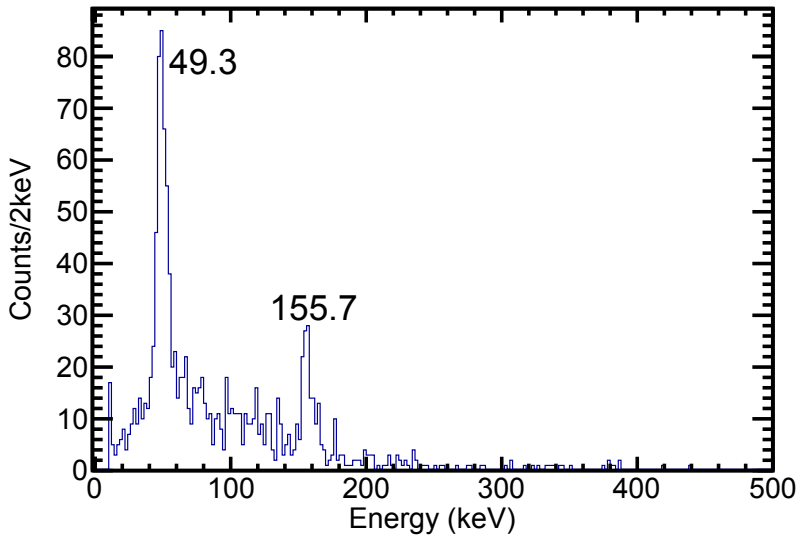

Figure 5.14 Energy spectrum of the second-pulse of double-pulse signals identified in the Ru setting.

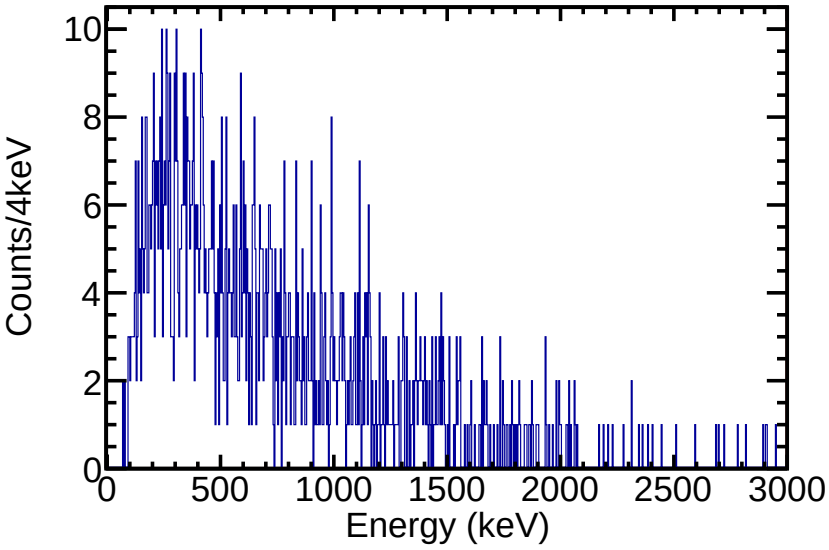

Figure 5.15 Energy spectrum of the first-pulse of a double-pulse identified in the Ru setting. The spectrum is consistent with energetic β-decay electrons. For reference, the Q-value of the decay discussed in this section, ^{118}Pd, is 4100(200) keV [82].

keV state, with a 224.2-keV transition elsewhere in the level scheme (Fig. 5.17). Therefore, one possibility for this 49.3-keV peak was a 45.8-keV transition with a half-life on the order of 0.1 μs in ^{118}Ag [83]. However, given the relative intensities in Ref. [83], the number of counts expected in the possible coincident transitions (125, 224, 380 keV) would be an order of magnitude greater.

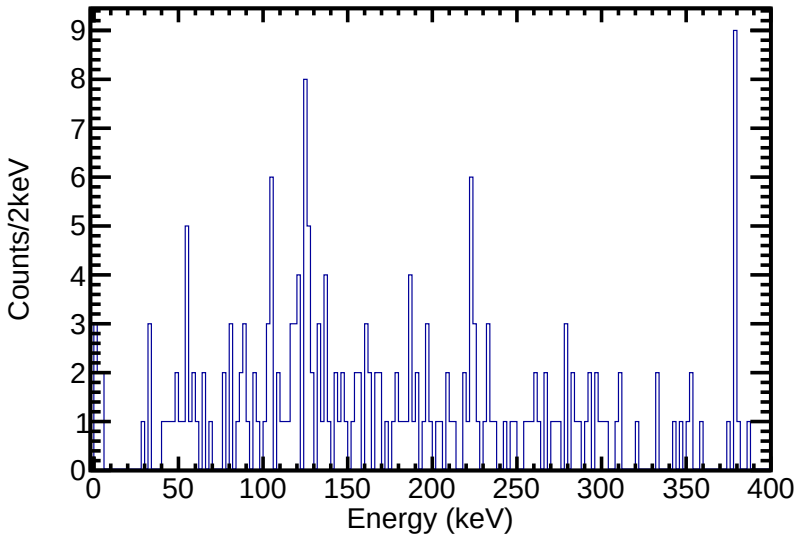

Figure 5.16 Clover γ ray energy spectrum in coincidence with the 49.3-keV peak in the second-pulse energy spectrum.

If the assignment to ^{118}Ag was correct, the peak should appear in the decay-correlated energy spectrum of lower Z, mass 118 nuclei. The peak at 49.3 keV was correlated with PID positions containing ^{118}Rh (granddaughter ^{118}Ag) and ^{118}Pd (daughter ^{118}Ag). The half-life of ^{118}Rh was 310(30) ms [73], while that of the daughter, ^{118}Pd, was 1.9(1) s [84]. For a correlation time of 2 s, the GeDSSD second-pulse spectrum for ^{118}Rh and ^{118}Pd is displayed in Fig. 5.18. The 49-keV peak is correlated with both implanted ions with slightly more intensity in the ^{118}Pd correlated spectrum. The time between the first- and second-pulse is plotted in Fig. 5.19. The half-life curve appears to be a growth and decay curve, though there is no clear peak in the first-pulse energy spectrum to indicate which transitions may be populating the isomeric state. A good fit to the decay curve was not obtained. There was a small number of counts in other implant gates, but the

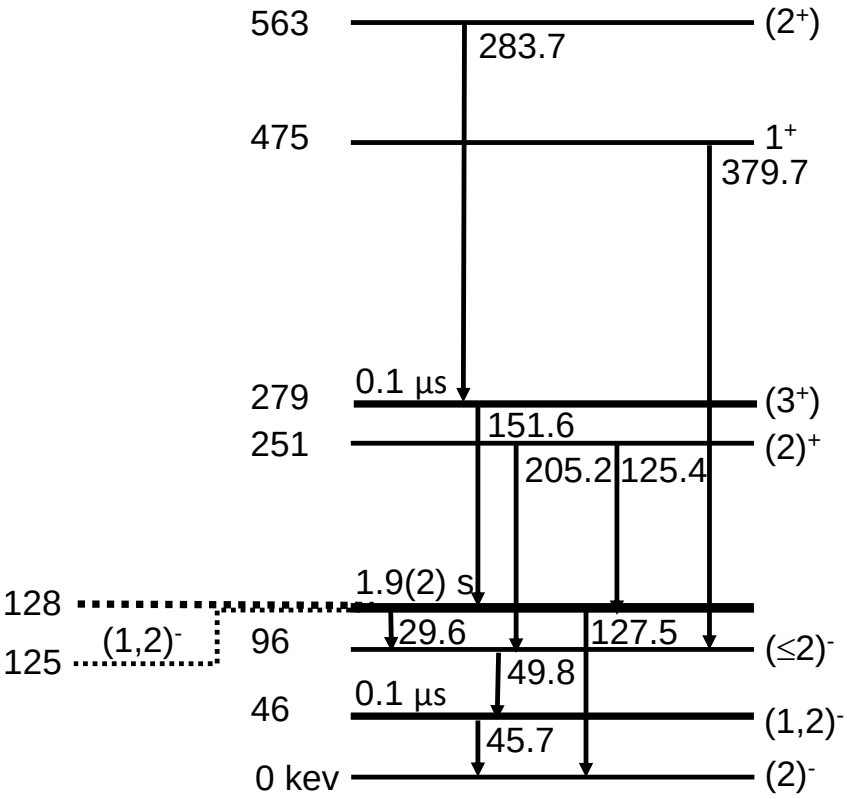

Figure 5.17 Partial level scheme of ^{118}Ag. Data are taken from Refs. [83, 84].

number of counts in the peak at 49 keV was proportional to the total number of implants within each gate, at a percentage between 0.2% to 0.4% of the total number of implants. The A=118 gates contained nearly twice that of all other ion gates.

Likewise, the coincident γ-ray spectrum can be viewed in coincidence with the 155.7-keV transition (Fig. 5.20). A signal several counts high was seen at 283 keV in coincidence with the signal in the planar detector. A candidate for this transition was also ^{118}Ag, with a 151.6-keV isomeric transition and half-life on the order of 0.1 μs [84] in coincidence with a 283.7-keV transition. Given the detector efficiencies and previously determined relative intensities in Ref. [84], from the number of counts in the peak at 156 keV, 16$\pm$4 counts at 283 keV would be expected, with was higher than the 5 to 6 counts at 283 keV in Fig. 5.20. As is demonstrated in Fig. 5.18, the 156-keV transition was also correlated with ^{118}Pd implants. The timing difference between the two pulses is displayed in Fig. 5.21. The peak at 155 keV did not exist in any other

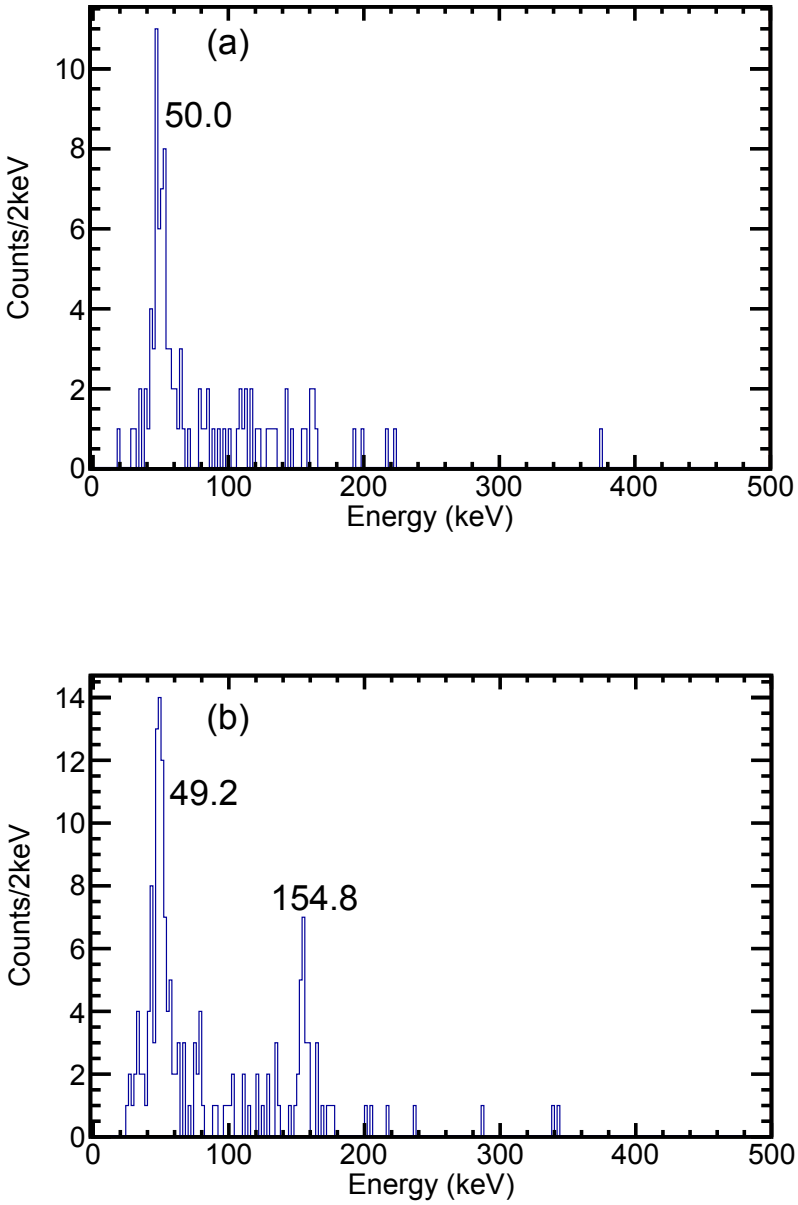

Figure 5.18 GeDSSD second-pulse energy spectrum gated on (a) ^{118}Rh implants and (b) ^{118}Pd implants using a correlation time of 2 s.

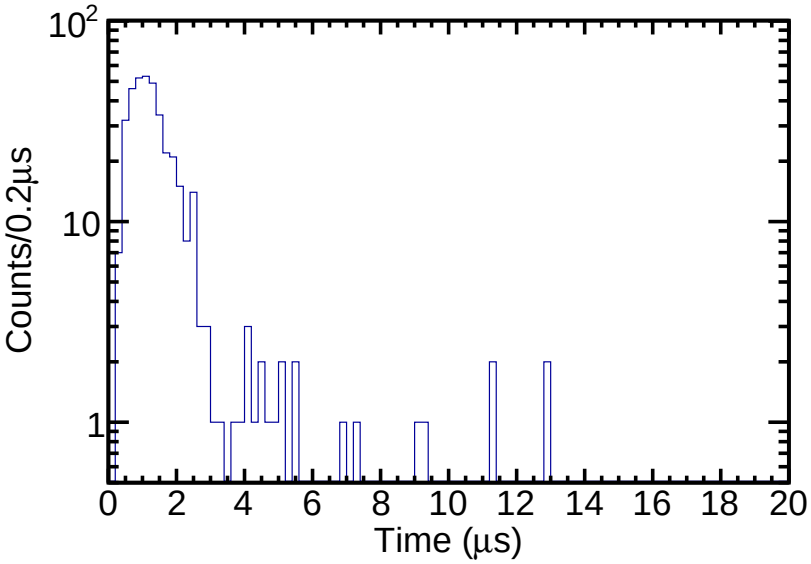

Figure 5.19 Timing difference between the first- and second-pulse in a double-pulse signal gated on the 49.3-keV peak in the second-pulse energy spectrum in Fig. 5.14.

decay correlated spectra.

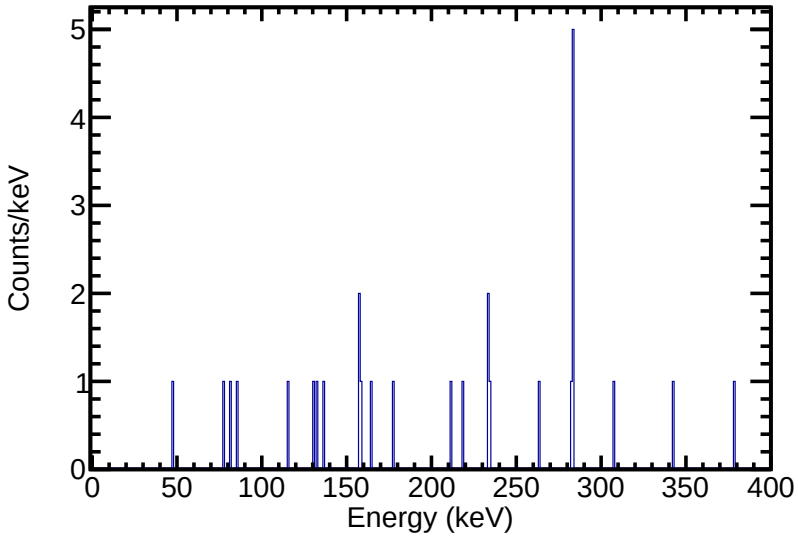

Figure 5.20 Clover γ-ray energy spectrum in coincidence with with the 155.7-keV peak from Fig. 5.14.

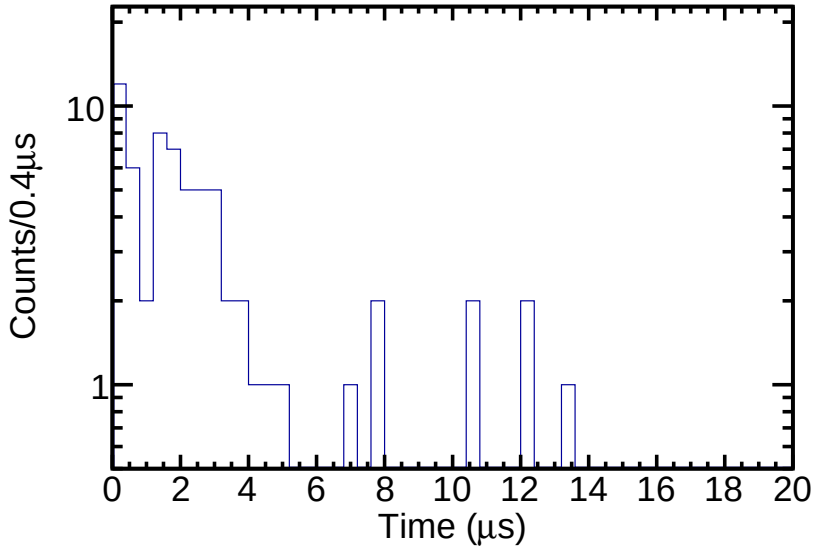

Figure 5.21 Timing difference between the first- and second-pulse gated on the 155.7-keV peak.

5.3.2 Double-pulses in Nb setting

As with the Ru setting, the Nb setting data may be filtered with the double-pulse algorithm. Fig. 5.22 shows the energy of the second-pulse for this setting, where peaks at 32.5, 57.1, 71.2, 94.5, and 114.9 keV may be seen. Very few counts existed in the spectrum above 500 keV and, as mentioned before, this was not due to an artificial cut due to on large amplitude first energy signals. There did not appear to be any peaks in the energy of the first-pulse gated around any of the second-pulse peaks. Fig. 5.23 shows the first-pulse energy gated on the 57.1-keV peak as a representative example. The coincident γ-ray spectrum with the 57.1-keV peak is presented in Fig. 5.24 and contains a possible peak at 152 keV, and a larger peak at 510.7 keV. With a lack of counts in the second energy spectrum above 500 keV, this appeared unlikely to arise from pair production, however, after correcting for the clover efficiency, there would be 530 ± 172 counts at 511 keV, which did overlap within the fit uncertainties with two 511 counts for each of the 153 ± 38 counts in the 57.1-keV peak in the GeDSSD spectrum.

The 57.1-keV transition was correlated with all isotope gates at long correlation times ($\sim$2 s or greater) in an amount proportional to the number of implants of each ion, at a rate of approximately

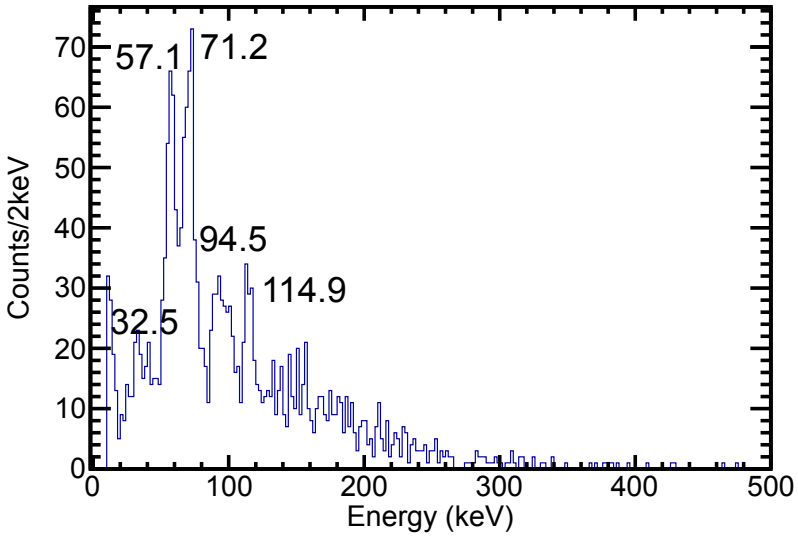

Figure 5.22 Energy of the second-pulse for isotopes in the Nb setting.

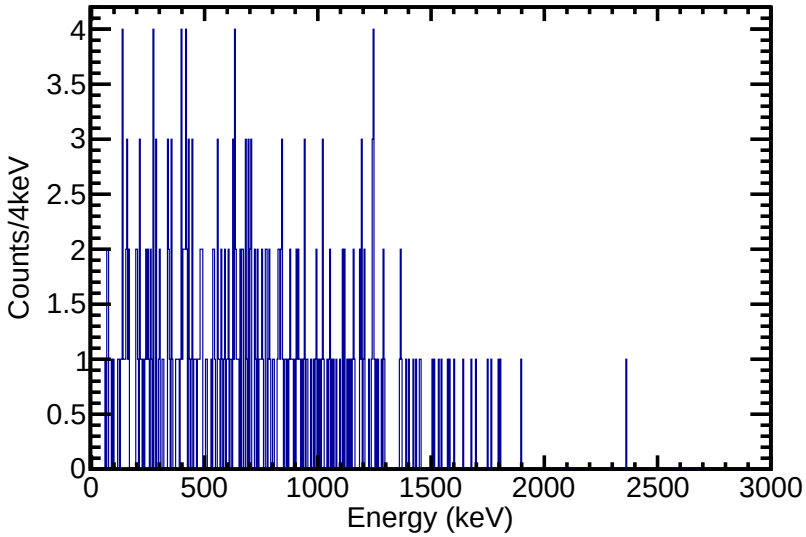

Figure 5.23 Energy for the first-pulse gated on the 57.1-keV peak for isotopes in the Nb setting.

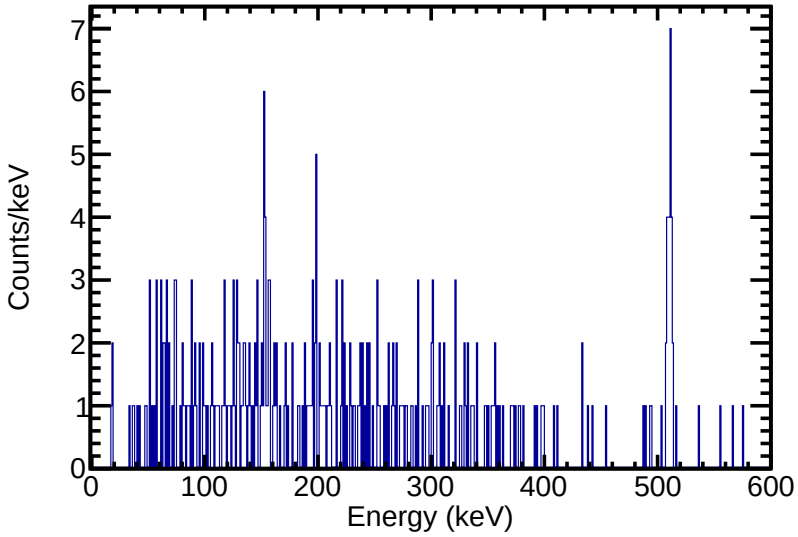

Figure 5.24 Coincident clover spectrum for the peak at 57.1 keV in the GeDSSD.

0.68%. Therefore, the 57.1-keV transition likely exists within an isotope far down the decay chains of one of the implanted ions. This was in contrast to the 49-keV peak in the Ru setting, where there was a strong correlation with four PID gates with A=118 in 2 s, with a weaker correlation to all other gates. Here, the 57.1-keV transition was correlated to all PID spots equally, at very long times after ion implantation. The timing difference between the the first and second-pulse of the double-pulse is shown in Fig. 5.25, where a half-life of 1.9(2) μs is found.

One isomeric state that could account for the 57.1-keV transition lies at 3108 keV in ^{118}Sn, with a half-life of 2.52(6) μs [85]. However, given the statistics of the experiment and the efficiencies of the detectors, there would likely be several coincident γ rays (for example, 477 and 254 keV) with enough statistics to be visible in coincidence (Fig. 5.24), however they were not clearly present. Given the slight miss-match between the ^{118}Sn half-life and the observed half-life and the lack of coincident transitions, this was likely an unknown transition that is unable to be identified in the current work.

The coincident clover spectra for the peaks other than the 57.1-keV peak did not appear to have any coincident transitions. A second peak that was correlated in isotope gates lies at 71.2-keV. This peak was present in PID gates containing ^{109}Nb and ^{109}Mo (Fig. 5.26). Previous work [31]

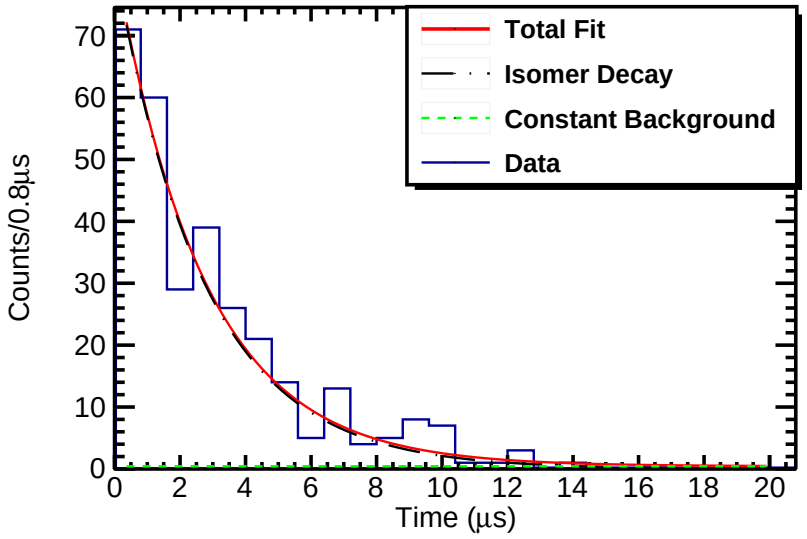

Figure 5.25 Decay curve gated on the 57.1-keV peak. A half-life of 1.9(2) μs is found from the fit, with 280(40) decays.

established an isomeric state in ^{109}Mo at 69.7 keV with a half-life of $0.194^{+0.076}_{-0.049}$ μs. The half-life curves in this work for each of the two isotope gates in Fig. 5.26 are shown in Fig. 5.27. While there did appear to be slight differences between the two spectra in Fig. 5.27 due to the different ways in which the isomeric state was populated (in panel (a), a growth and decay curve populated from a higher excited state in ^{109}Mo and in panel (b), from the β decay of ^{109}Nb into the isomeric state), there is not enough statistics in either gate to satisfactorily fit the curves.

Finally there was a peak at 67.8 keV correlated with $^{107/110}$Nb implantation. The second-pulse energy spectrum is displayed in Fig. 5.28 for a correlation time of 1 s. Previous work found an isomeric state at 65 keV with a half-life of 420 ns in ^{107}Mo [86]. The half-life curve for this transition is illustrated in Fig. 5.29. As with the other low-statistics half-life curves, the plot in Fig. 5.29 was difficult to fit.

The spectrum in Fig. 5.22 has a few other peaks, though the 33-keV, 95-keV, and 115-keV peaks did not appear to be associated with any PID gate within the beam setting, nor did these peaks appear in the double-pulse spectrum from the data taken immediately after the experiment ended. These peaks did not appear to have any coincident γ rays in the clover spectra or in the first

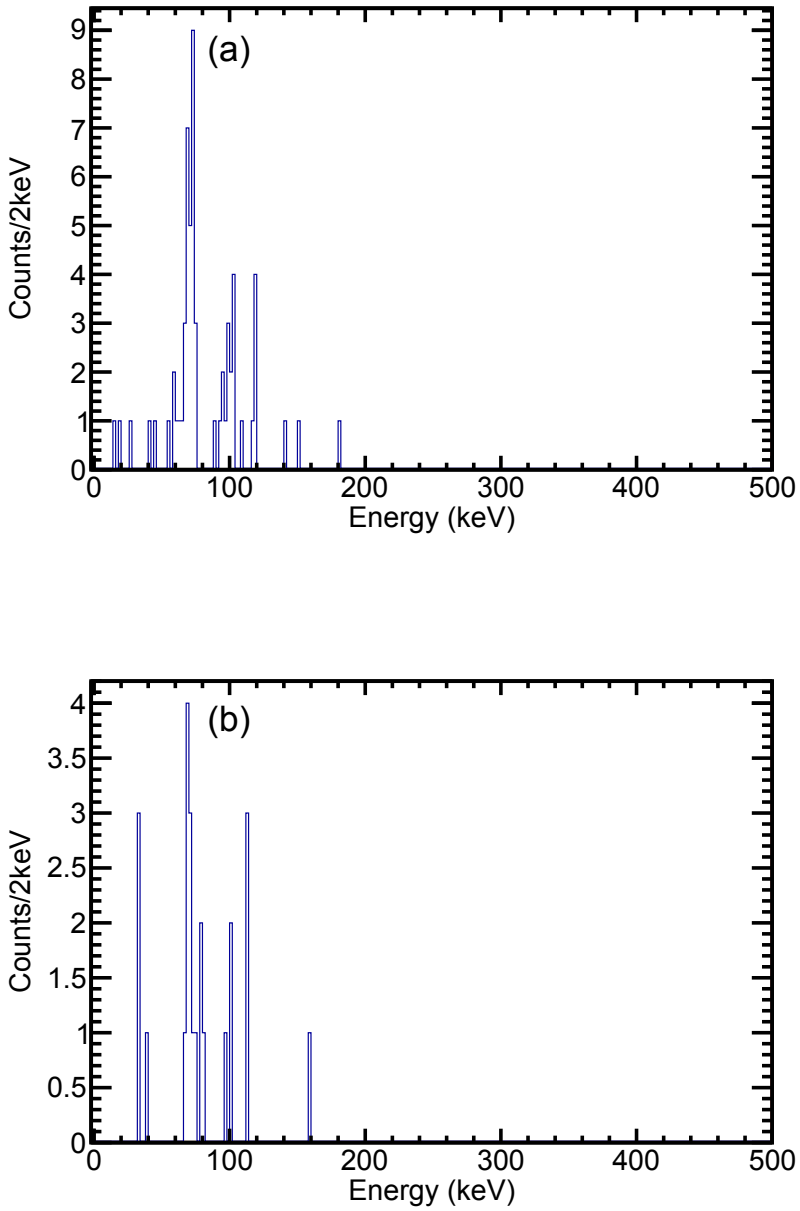

Figure 5.26 Energy of the second-pulse for (a) $^{109/112}$Mo implants and (b) $^{106/109}$Nb implants. Both spectra are shown for a 5 s correlation time.

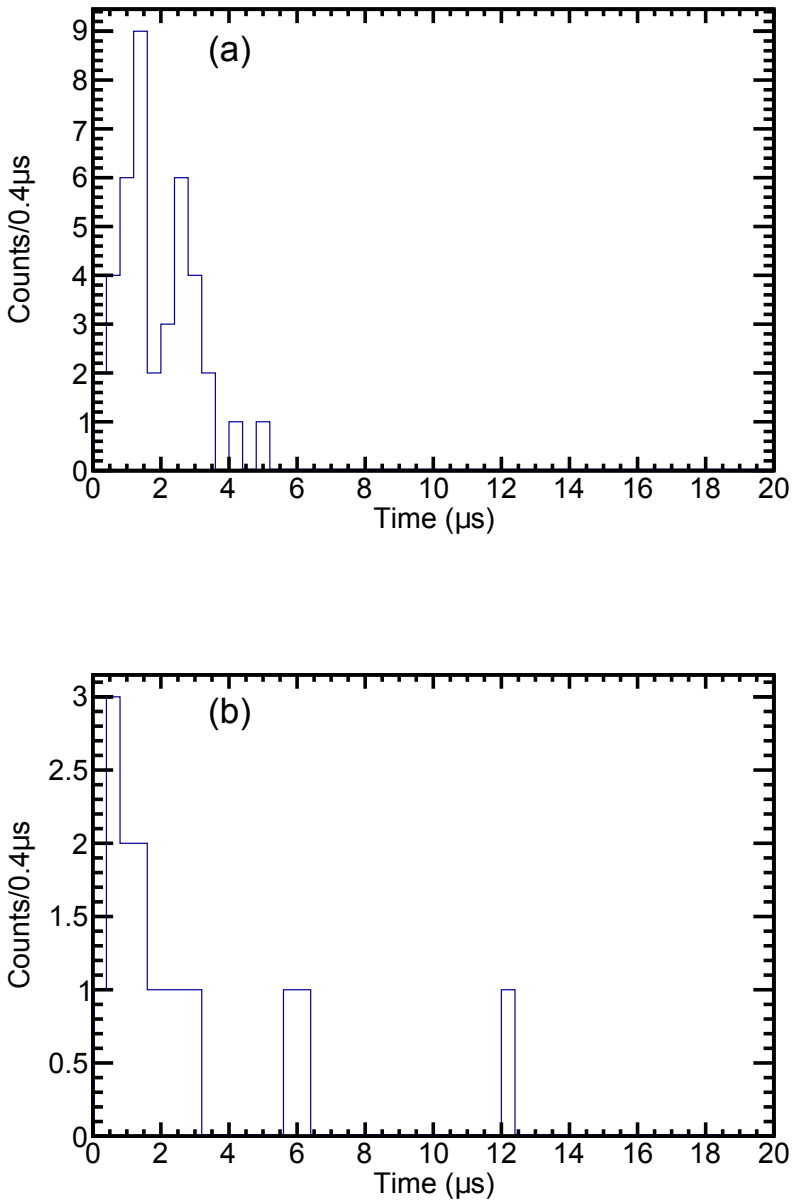

Figure 5.27 Timing difference between the two pulses for (a) $^{109/112}$Mo implants and (b) $^{106/109}$Nb implants.

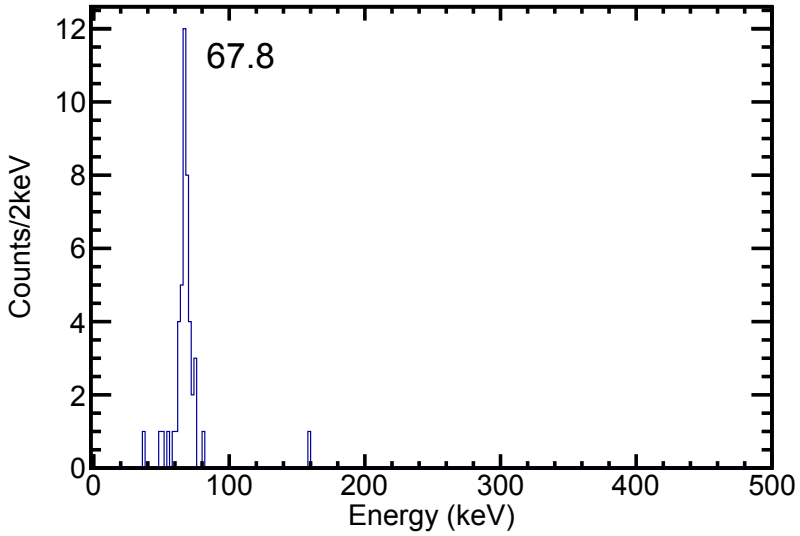

Figure 5.28 Second-pulse energy correlated to $^{107/110}$Nb implants within 1 s.

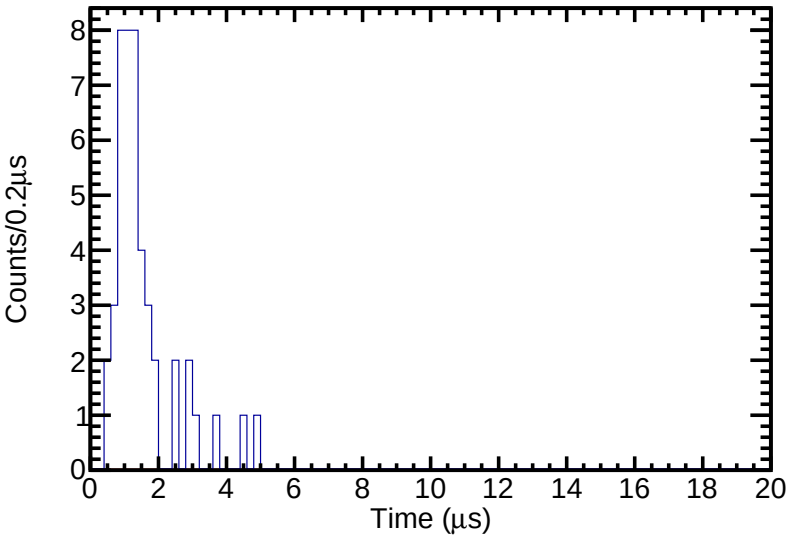

Figure 5.29 Timing difference between the first and second-pulse for the peak at 67 keV correlated to $^{109/112}$Mo implants within 1 s.

energy pulse spectra. The half-life curves for these three peaks are shown in Fig. 5.30. In panel (a), the 33-keV peak was small, so it was likely that many of the counts within the half-life curve correspond to background. With no coincident transitions and no clear correlation to particular implants, it was difficult to identify these remaining transitions. No clear candidates were found.

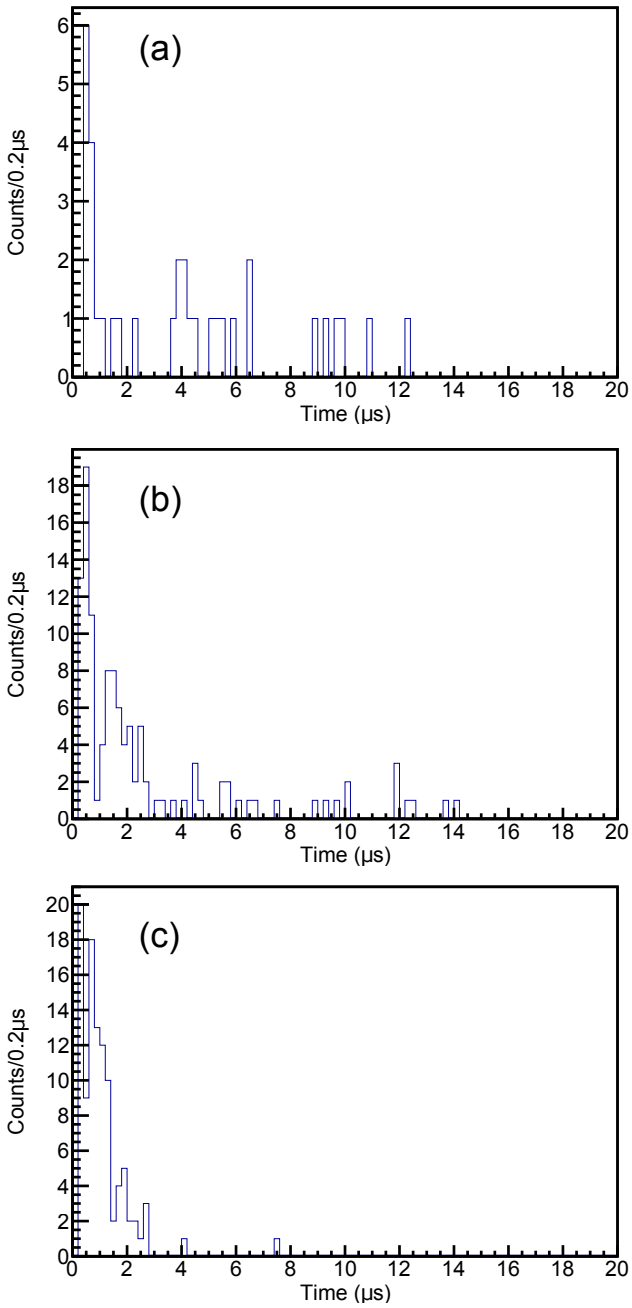

Figure 5.30 Timing difference between the first and second-pulse gated for the (a) 33-keV (b) 95-keV (c) 115-keV peaks.

5.4 β-delayed γ rays

In this section, β-delayed γ rays with the various PID gates are presented. Where multiple β-delayed γ rays were observed, relative intensities are calculated. For isotopes with sufficient counts within their spectra, the TKE separation technique discussed in Section 4.3.2 was applied. No new β-delayed γ rays were identified in either production setting. The observed β-delayed γ rays are summarized in Table 5.4. For isotopes where relative intensities were able to be determined, these are summarized in Table 5.5.

Table 5.4 Summary of the β-delayed γ rays observed in this work.

Produced Isotope	Daughter	Literature Energy	Reference	This Work
^{115}Rh	^{115}Pd	127.8, 125.8	[74]	126.6
^{118}Rh	^{118}Pd	378.6, 434.0, 574.6	[73]	378.4, 434.0, 574.6
^{116}Rh	^{116}Pd	340.3, 397.7	[70]	340.3, 397.8
^{115}Pd	^{115}Ag	125.5	[69]	125.7
^{118}Pd	^{118}Ag	125.4, 379.7	[83]	125.7, 378.1
^{118}Pd	^{118}Ag	256.6, 326.1	[87]	256, 326.9
^{114}Ru	^{114}Rh	127, 179.7	[88]	126.1, 178.3
^{113}Tc	^{113}Ru	98.5, 164.3	[4]	98.4, 164.8
^{114}Tc	^{114}Ru	265.1, 298.0, 443.0, 563.4	[71]	264.9, 298.3, 442.5, 563.2
^{112}Tc	^{112}Ru	236.8, 511.5	[89]	236.0, 510

5.4.1 Ru setting

There were 11 clear gates in the PID for the Ru setting, which are shown in Fig. 5.31. While the previous section discussed the γ rays associated with the implantation of $^{115/118}$Rh and was used to confirm the PID and demonstrate the TKE separation, other PID groups also contained previously known γ rays. Table 5.6 show the total number of implants for each group in the PID, where F denotes a fully-stripped ion, H denotes an H-like ion, and He denotes a He-like ion. Unless otherwise noted, the correlation time in these images was 500 ms.

Table 5.5 Summary of γ ray relative intensities observed in this work.

Produced Isotope	Daughter	Energy	Literature Relative Intensity	Reference	This Work
^{118}Rh	^{118}Pd	378.4 434.0 574.6	100, 100 10.0(4), 15(2) 21.4(12), 42(5)	[73], [88]	100 23(13) 49(21)
^{116}Rh	^{116}Pd	340.3 397.8	100 32.6(41)	[70]	100 32.7(16)
^{113}Tc	^{113}Ru	98.4 164.3	100 54	[4]	100 60(38)
^{114}Tc	^{114}Ru	264.9 298.3 442.5 563.2	100 25(3) 25(3) 29(5)	[71]	100 22(15) 27(16) 55(24)

Table 5.6 Number of implanted ions and decays in the Ru beam setting using a correlation time of 500 ms.

Isotope	Charge states	Number of Implants	Number of Decays
$^{118/121/124}$Ag	He, H, F	1421	2412
$^{115/118}$Pd	He, H	5504	8992
$^{116/119}$Pd	He, H	3890	6719
$^{117/120}$Pd	He, H	1427	2700
$^{115/118}$Rh	H, F	6183	11075
$^{116/119}$Rh	H, F	7506	5997
$^{117/120}$Rh	H, F	3266	6270
$^{112/115}$Ru	H, F	1321	2402
$^{113/116}$Ru	H, F	3584	6856
$^{114/117}$Ru	H, F	2315	4391
$^{115/118}$Ru	H, F	302	668

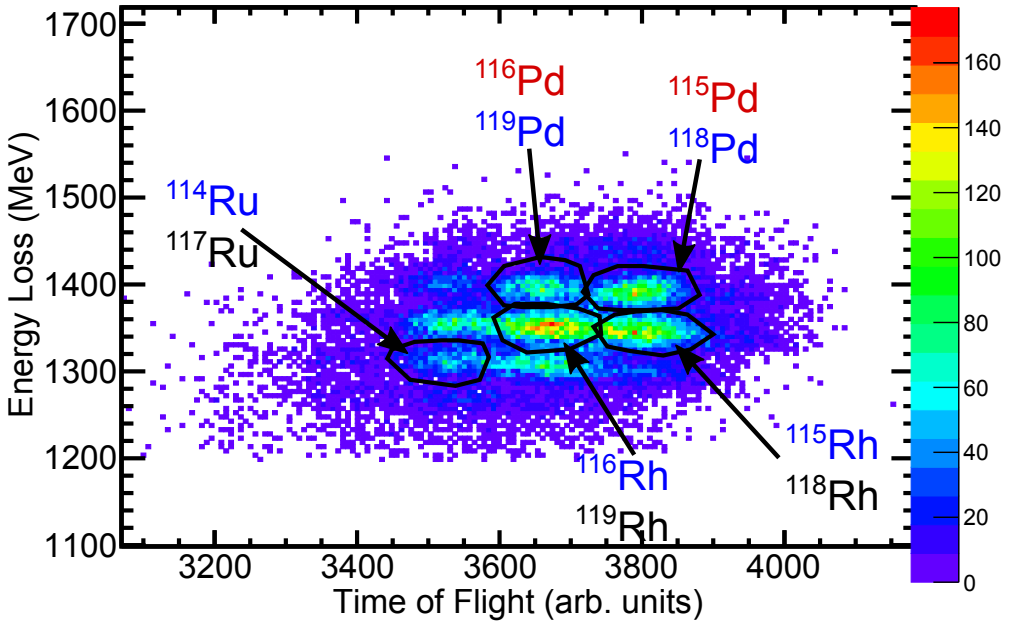

Figure 5.31 PID with some of the groups labeled with the identified charge state contaminants. Labels in black are fully-stripped ions, blue corresponds to H-like ions, and red is for He-like ions.

5.4.1.1 $^{115/118}$Rh

The relative intensities of the isotopes used to develop the TKE separation technique may be calculated for the ^{118}Rh β-delayed γ rays (Fig. 4.9). Two previous results gave differing relative intensities, which were compared to the present work in Table 5.7. The relative intensities in this work agreed with the values from the previous works.

Table 5.7 Tabulated relative intensities for the γ rays observed in the decay of ^{118}Rh.

Energy (keV)	This work	Ref [88]	Ref [73]
378.4	100	100	100
434.0	23(13)	15(2)	10.0(4)
574.6	49(21)	42(5)	21.4(12)

5.4.1.2 $^{116/119}$Rh

The most intense group in the PID contained the $^{116/119}$Rh ions. There were two previously known ^{116}Rh [70] β-delayed γ rays clearly observed in the data at 340 and 398 keV. The relative intensities of the 340-keV and 398-keV transitions, after correcting for the efficiency, were 100 and 32.7(16), respectively. This compared very favorably with previous literature results of 100 and 32.6(41) [70].

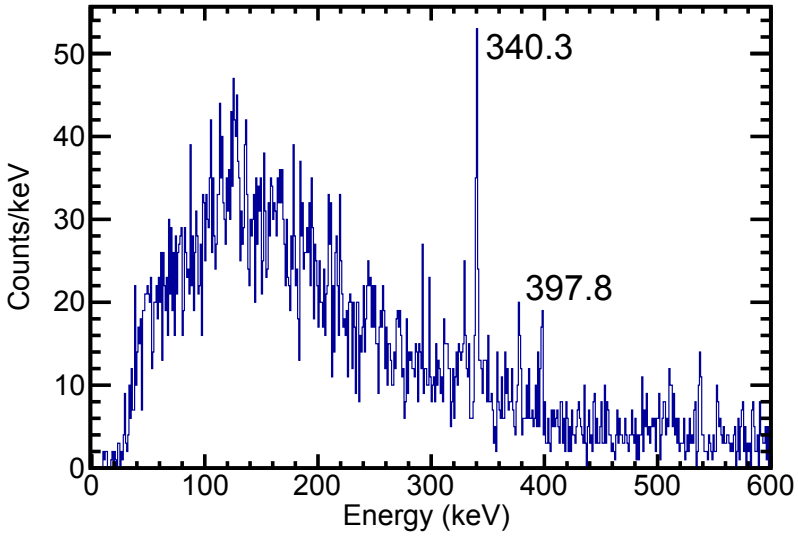

Figure 5.32 β-delayed γ-ray spectrum correlated to $^{116/119}$Rh within 500 ms. Previously identified ^{116}Rh [70] γ rays are marked.

The TKE separation techniques for the edge strips in the detector discussed in Section 4.3.2 can be used with this PID gate to separate out the ^{116}Rh γ rays. The subset of events from in Fig. 5.32 where the ion was located in the edge strips of the GeDSSD is displayed in Fig. 5.33. Two gates were applied to the Image 2 position vs energy spectrum shown in Fig. 5.34. The left gate was expected to have an enhanced contribution from ^{116}Rh whereas the right gates was expected to have an enhanced contribution from ^{119}Rh. The γ ray spectra gating on the left and right TKE gates are given in Fig. 5.35 and 5.36 respectively. The 340-keV transition was, again, very clearly seen in Fig. 5.35 (^{116}Rh), while it was non-apparent in Fig. 5.36 (^{119}Rh), indicating a reasonable separation between charge states. Unfortunately, no β-delayed γ rays became apparent in the

^{119}Rh β-delayed spectrum. Of the total number of events observed in the edges of the detector, 45.5% lie within the (left) ^{116}Rh gate and 23.9% lie within the (right) ^{119}Rh gate. The observed number of counts at 340 and 398 keV were compared to the expected number of counts if there was no TKE separation determined by taking the peak intensities in Fig. 5.33 and scaling by the percentage of ions in the TKE gate. This is summarized in Table 5.8, which further demonstrates the TKE charge state separation technique.

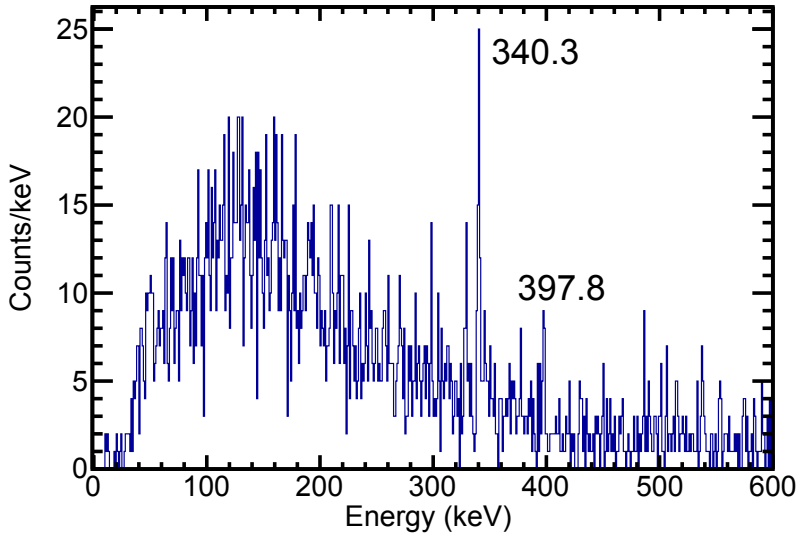

Figure 5.33 β-delayed γ-ray spectrum correlated with $^{116/119}$Rh for events confined to the edge strips of the GeDSSD. Previously measured ^{116}Rh γ rays [70] are labeled with their energies in keV.

Table 5.8 Observed counts for transitions in ^{116}Rh and ^{119}Rh decays compared to the expected number of counts if there were no TKE separation. The expected number of counts were determined by scaling the total number of implants for the number within each gate.

Gate	Total in TKE Gate	Number of Observed 340 keV Counts	Scaled 340 keV Counts	Number of Observed 398 keV Counts	Scaled 398 keV Counts
All Edge Events	5744	42±23	-	16±7	-
^{116}Rh (left)	2614	31±10	19±6	13±8	7±3
^{119}Rh (right)	1345	0±0	10±2	0±0	4±2

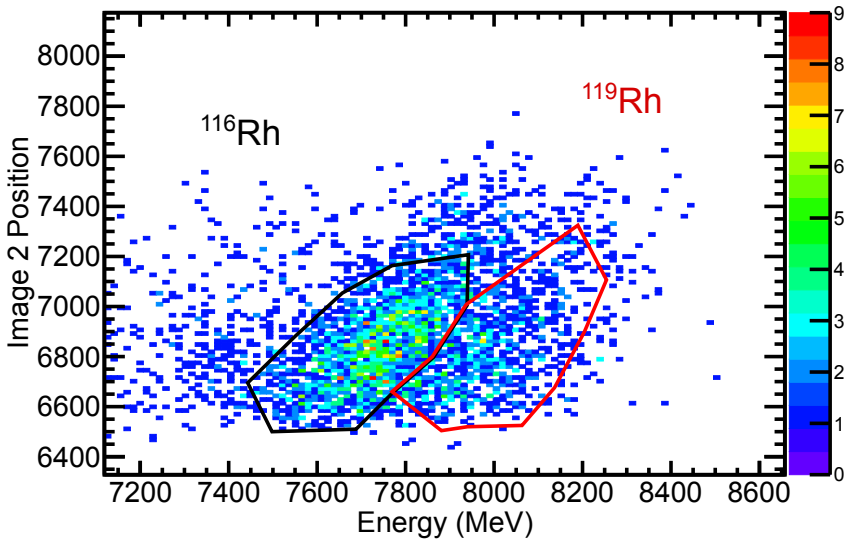

Figure 5.34 Image 2 position vs. the sum of the PIN and GeDSSD energies gates on the $^{116/119}$Rh implants. On the left is ^{116}Rh and on the right is ^{119}Rh.

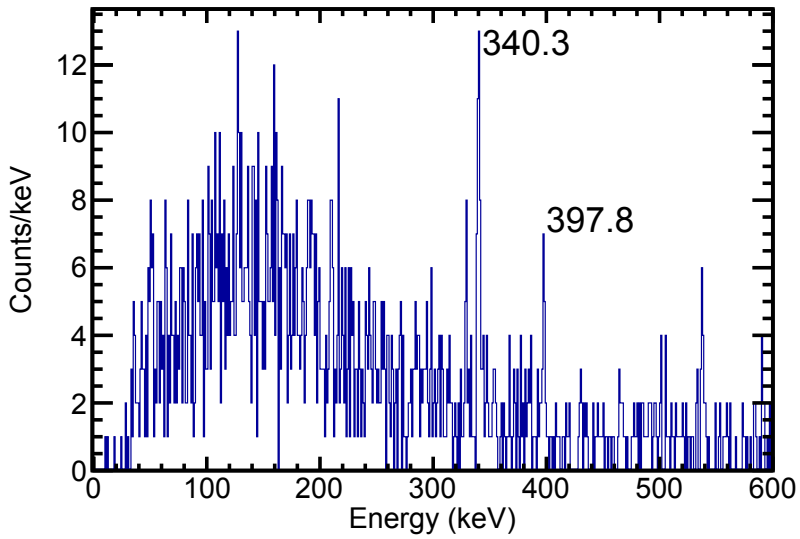

Figure 5.35 β-delayed γ-ray spectrum correlated with $^{116/119}$Rh and confined to the edge strips. An additional requirement on the TKE of the ions expected to enhance the decays of ^{116}Rh was applied to the figure. See text for details.

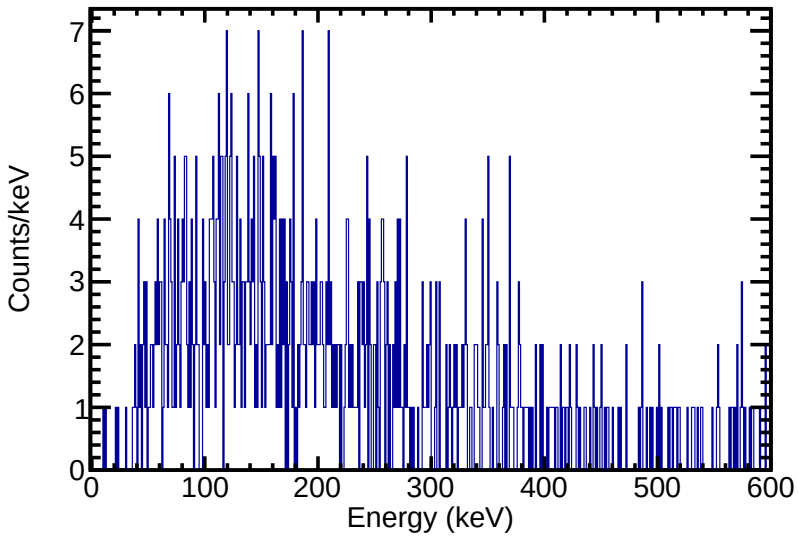

Figure 5.36 β-delayed γ-ray spectrum correlated with $^{116/119}$Rh and confined to the edge strips. An additional requirement on the TKE of the ions expected to enhance the decays of ^{119}Rh was applied to the figure. See text for details.

5.4.1.3 $^{115/118}$Pd

Fig. 5.37 shows the β-delayed γ rays correlated with $^{118/115}$Pd within 500 ms, where ^{118}Pd was the H-like charge state and ^{115}Pd was the He-like charge state. Both ^{118}Pd and ^{115}Pd have a previously reported [69, 83, 84] γ ray transition at 125 keV. The ^{118}Pd β decay also leads to a 379-keV transition, though the peak in Fig. 5.37 was at a slightly lower energy. However, based upon previous results [69] a non-coincident 255-keV transition should be more intense than the 125-keV transition from the ^{115}Pd decay. A transition at 255 keV was not apparent in the PID-gated β-delayed γ-ray spectrum in Fig. 5.37.

The TKE gating technique can be applied to the edges of the detector in this case as well. For the subset of events confined to the edges of the GeDSSD from Fig. 5.37, Fig. 5.38 shows the β-gated clover spectrum. Two gates were applied to the Image 2 position vs. energy plot in Fig. 5.39. The left gate was expected to enhance the contribution from ^{115}Pd whereas the right gate was expected to have an enhancement from ^{118}Pd. Fig. 5.40 shows the histogram gated for ^{115}Pd (left). The 125-keV γ ray remained, but there was no appearance of a 255-keV γ ray. Based

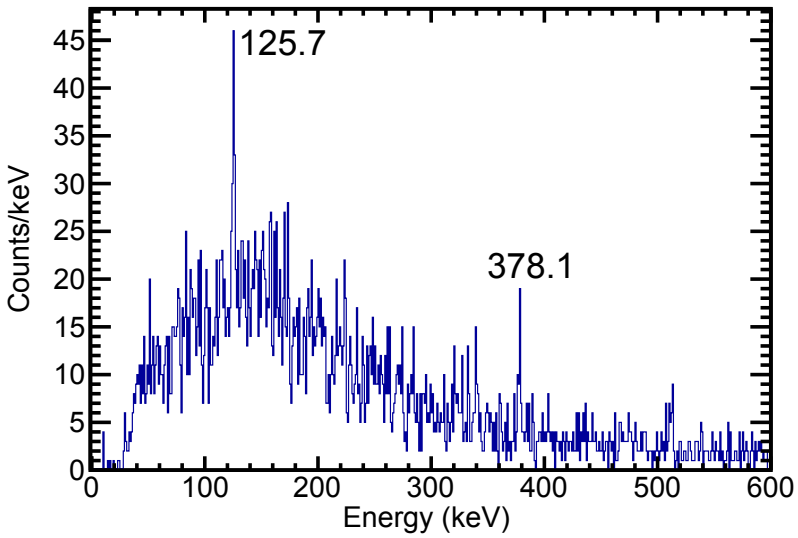

Figure 5.37 β-decay γ-ray spectrum correlated to $^{115/118}$Pd within 500 ms. Refs. [83, 84] previously reported 125-keV and 379-keV transitions in the decay of ^{118}Pd. Ref. [69] reported at 125-keV transition in the decay of ^{115}Rh.

upon previous relative intensities, 17 counts at 255 keV would be expected. In Fig. 5.41 (the right gate), the β-delayed γ-ray spectrum gated on ^{118}Pd is shown. While the 378-keV transition was clear, the 125-keV γ ray was less obvious, despite previous results [83, 84] indicating the 125-keV transition as the most intense γ ray. Based upon the number of counts within the 378-keV peak in Fig. 5.41, 38 counts of the 125-keV peal in ^{118}Pd gate on the edge strips would be expected.

5.4.1.4 $^{116/119}$Pd

The β-delayed γ-ray spectrum correlated to $^{116/119}$Pd is presented in Fig. 5.42. There were a few previously identified γ rays present in the H- and He-like $^{116/119}$Pd gate. Previous ^{116}Pd β decay results [83] reported a transition at 114 keV, which was difficult to identify in the figure. Previous results for ^{119}Pd [87] indicated transitions at 256 and 326 keV, the latter may be seen in Fig. 5.42, and the former appears to have a few counts above the background. The most intense transition identified in the literature previously occurred at 130 keV and was not observed in the spectrum. There were not enough counts when confining the events to the edges of the GeDSSD to apply the

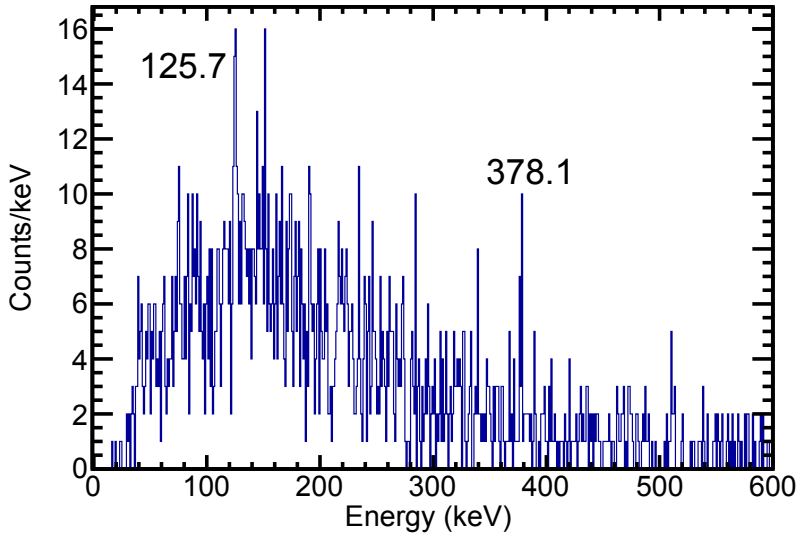

Figure 5.38 β-delayed γ-ray spectrum correlated with $^{115/118}$Pd for events confined to the edge strips of the GeDSSD. Previously measured γ rays are marked.

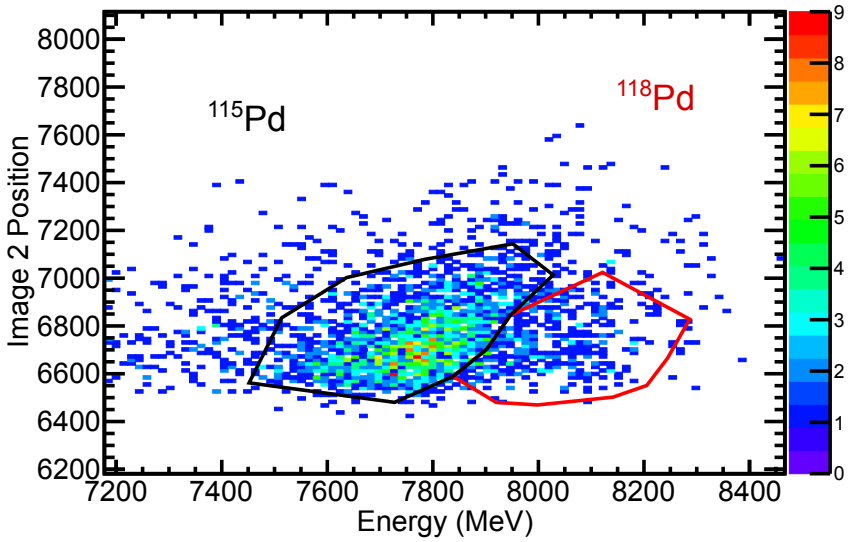

Figure 5.39 Image 2 position vs. the sum of the PIN and GeDSSD energies gates on the $^{115/118}$Pd implants. On the left is ^{115}Pd and on the right is ^{118}Pd.

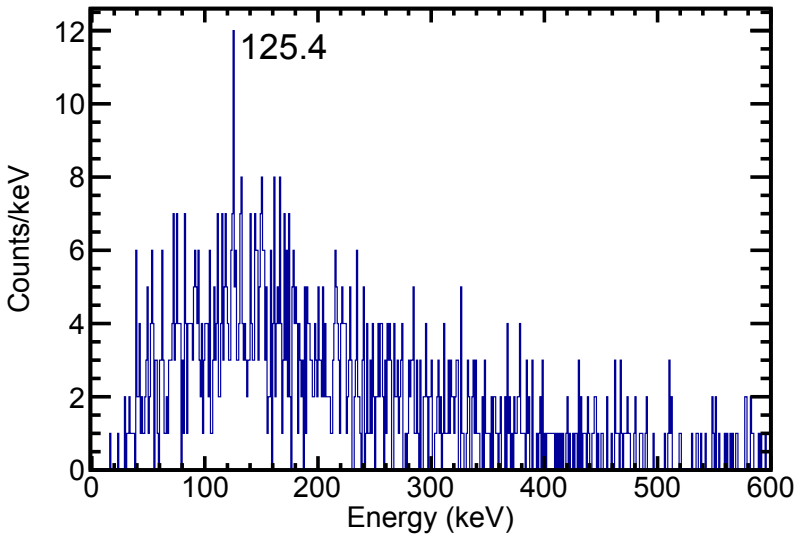

Figure 5.40 β-delayed γ-ray spectrum correlated with $^{115/118}$Pd and confined to the edge strips. An additional requirement on the TKE of the ions expected to enhance the decays of ^{115}Pd was applied to the figure. See text for details.

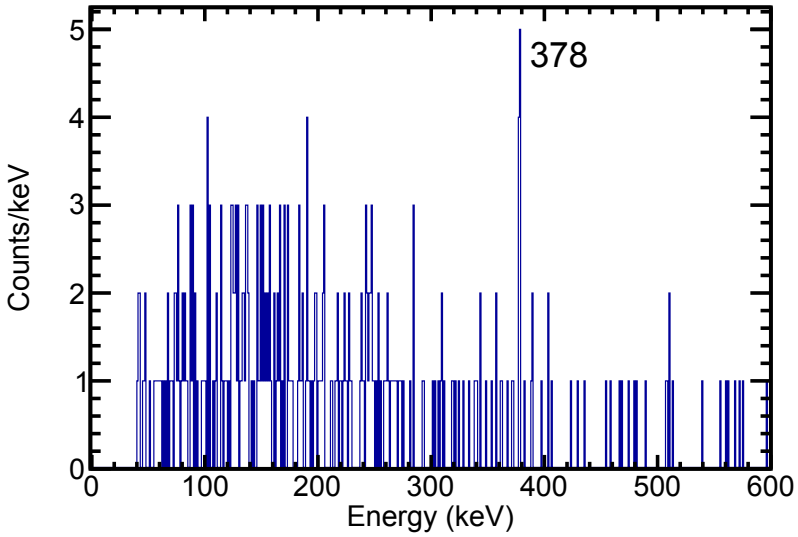

Figure 5.41 β-delayed γ-ray spectrum correlated with $^{115/118}$Pd and confined to the edge strips. An additional requirement on the TKE of the ions expected to enhance the decays of ^{118}Pd was applied to the figure. See text for details.

TKE technique.

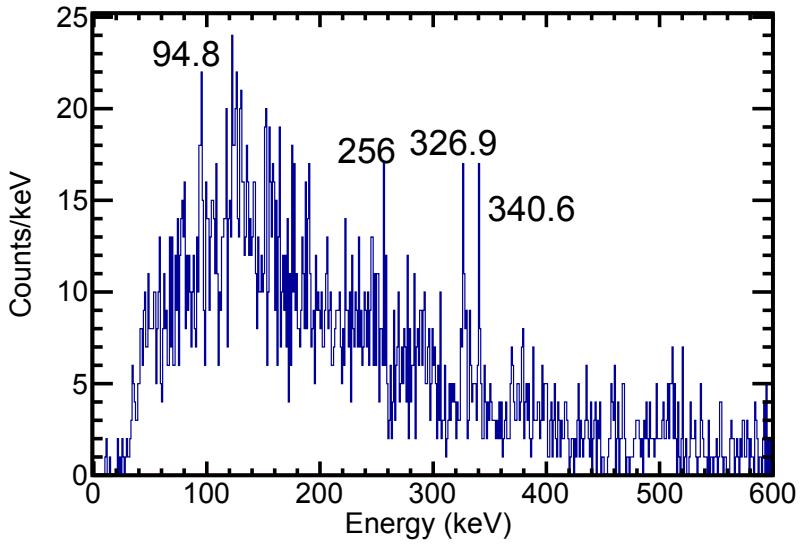

Figure 5.42 β-decay γ-ray spectrum correlated to $^{116/119}$Pd within 500 ms. Ref. [83] reports a 91.0 keV transition in the decay of ^{116}Pd. A few γ rays known from the decay of ^{119}Pd are seen here: 256.6, and 326.1 keV as reported in [87]. There is also what may be a peak at 340 keV.

5.4.1.5 $^{114/117}$Ru

The β-decay γ-ray spectrum correlated to ^{114}Ru and ^{117}Ru implants is displayed in Fig. 5.43. A few γ rays were previously identified in the decay of ^{114}Ru [88]. The three most intense γ rays were at energies of 127, 128 and 180 keV, of which peaks appear in Fig. 5.43. There were not enough counts when confining the events to the edges of the GeDSSD to apply the TKE technique.

5.4.1.6 All other PID gates

All of the other PID gates did not have any obvious β-delayed γ rays. A representative spectrum is shown in Fig. 5.44.

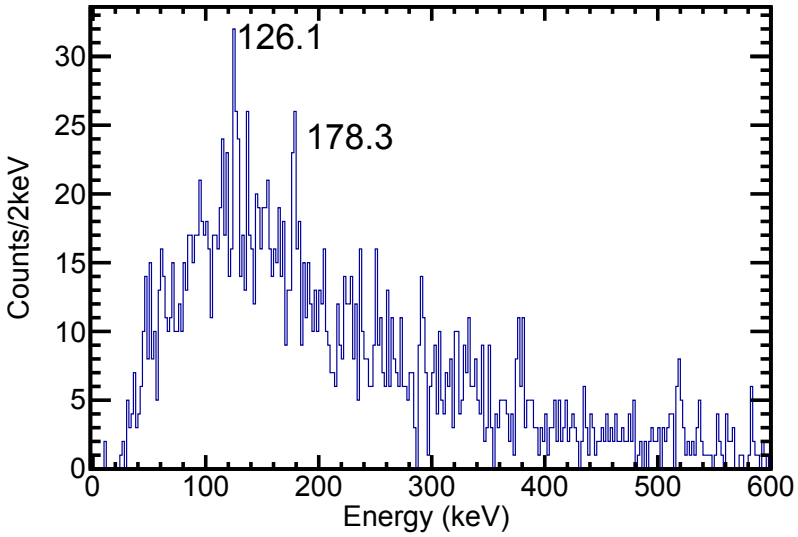

Figure 5.43 β-decay γ-ray spectrum correlated to $^{114/117}$Ru within 500 ms. Peaks near 125 and 179 keV likely arise from the decay of ^{114}Ru [88].

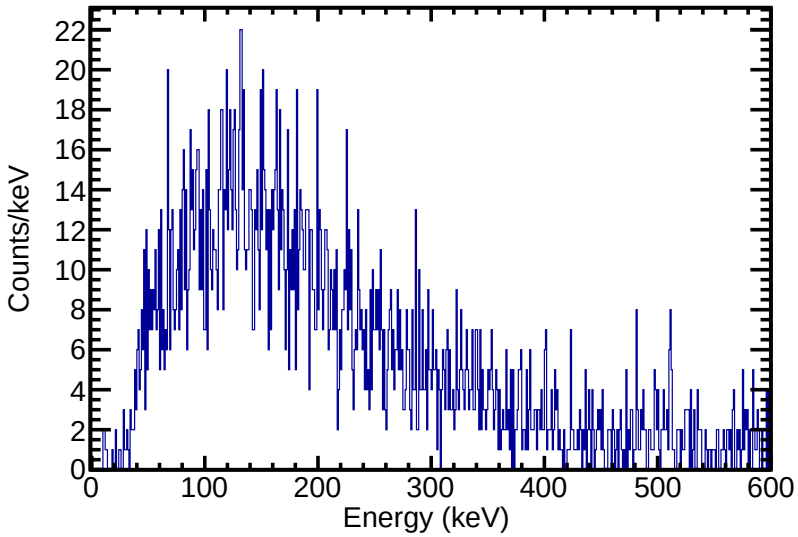

Figure 5.44 β-delayed γ-ray spectrum corresponding to the $^{117/120}$Rh PID gate illustrating the lack of clearly visible γ rays.

5.4.2 Nb setting

In the Nb setting, there are 15 clear groups in the PID figure. Table 5.9 summarizes the number of events for each isotope gate. The labeled PID for this setting is displayed in Fig. 5.45. All entries in the table have the heavier mass ion in the fully-stripped charge state and the lighter ion in the H-like charge state. For the gates containing ^{115}Ru, the number of implantation and decays are shown for two correlation times, as the longer correlation time was used for half-life determination and the shorter correlation time was used to generate the energy spectra discussed in Section 5.2. The number of decays relative to the number of implants in the 250 ms correlation time was small due to the β-decay half-life of the ground state of ^{115}Ru being 318 ms [12].

Table 5.9 Number of implants and decays with the Nb beam setting.

Isotope	Correlation Time	Number of Implants	Number of Decays
$^{112/115}$Ru	250 ms	664	613
	500 ms	664	1033
$^{113/116}$Ru	500 ms	1716	2640
$^{114/117}$Ru	500 ms	1246	1936
$^{115/118}$Ru	250 ms	510	559
	500 ms	510	931
$^{109/112}$Tc	500 ms	549	825
$^{110/113}$Tc	500 ms	4464	7670
$^{111/114}$Tc	250 ms	4087	3973
$^{112/115}$Tc	500 ms	1718	3026
$^{113/116}$Tc	500 ms	588	1110
$^{107/110}$Mo	500 ms	657	968
$^{108/111}$Mo	500 ms	2371	3687
$^{109/112}$Mo	500 ms	1610	2860
$^{110/113}$Mo	500 ms	628	1134
$^{106/109}$Nb	500 ms	641	938
$^{107/110}$Nb	500 ms	525	886

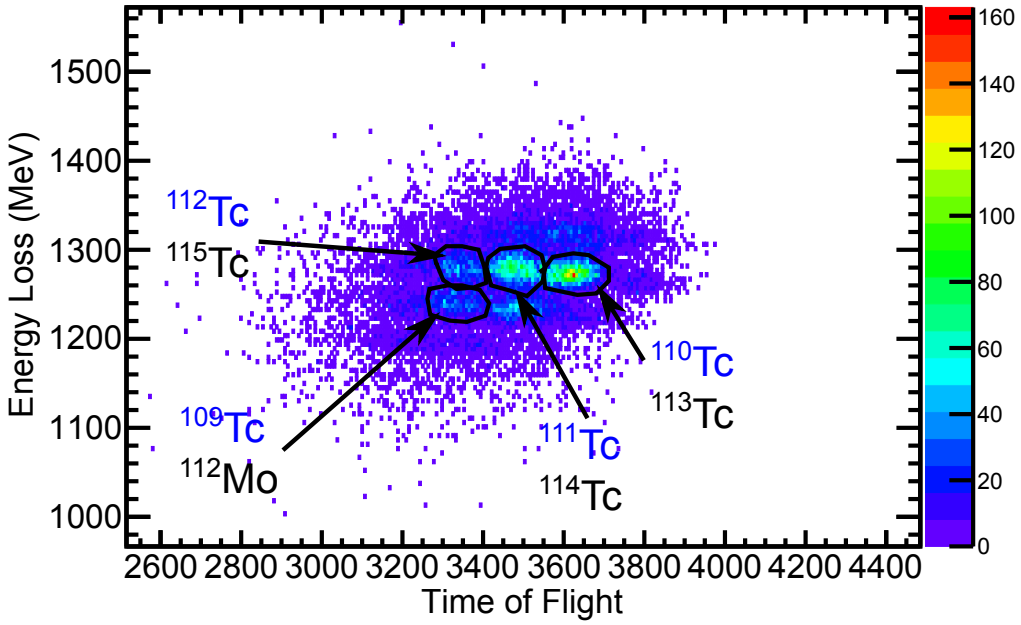

Figure 5.45 PID plot for the Nb setting with the isotope gates labeled. Black labeled isotopes are fully-stripped and blue labeled isotopes are H-like.

5.4.2.1 $^{110/113}$Tc

The $^{110/113}$Tc PID group was one of the most strongly populated groups in this setting. For this isotope, a correlation time of 500 ms was used. The β-delayed γ-ray spectrum is shown in Fig. 5.46. Two previously identified [4] β-delayed γ rays from the decay of ^{113}Tc were visible at 98 and 164 keV. Additionally, the most intense transition from the decay of the ^{113}Ru daughter was also visible at 263 keV [90]. With a longer correlation time, the peak at 263 keV was more apparent, strengthening the argument that this was a transition resulting from the decay of the daughter. Previous work indicated a relative intensities of 100 and 54% for the 99-keV and 164-keV transitions, respectively [4]. After correcting for efficiency, the relative intensities of the two transitions in the current work are 100 and 60(38)%. Very few counts were observed for the lighter charge state; therefore the effects of the TKE separation technique are not discussed here.

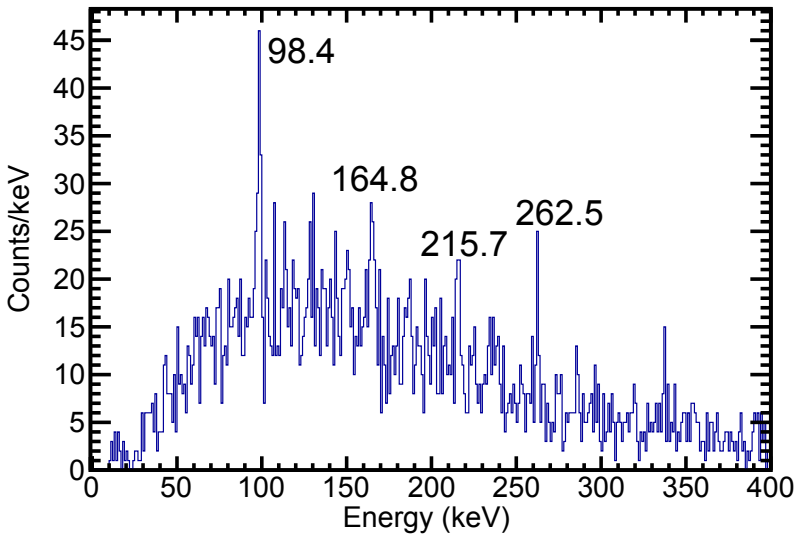

Figure 5.46 β-decay γ-ray spectrum correlated to $^{110/113}$Tc within 500 ms. The 98.5-keV and 164.3-keV γ rays populated in the decay of ^{113}Tc are readily apparent [4]. Additionally, the 263.2-keV transition in the daughter decay is also visible [90].

5.4.2.2 $^{111/114}$Tc

For the $^{111/114}$Tc group, a 250 ms correlation time was utilized. The half-lives found in previous studies of ^{114}Tc for the two β-decaying states were 88 and 100 ms [71]. The previously observed half-life for ^{111}Tc was 290 ms [33]. Several previously-identified [71] ^{114}Tc γ rays were apparent at 265, 298, 443, and 563 keV. The relative intensities of the 265-keV, 298-keV, 443-keV, and 563-keV transitions were 100, 25(3), 25(3), and 29(5) respectively in the literature [71]. In the present data, the intensities were found to be consistent, being 100, 22(15), 27(16), and 55(24), respectively.

Again, the TKE gates may be applied to the GeDSSD to separate the two charge states. The β-decay γ-ray spectrum displayed in Fig. 5.47 is constrained to events at the edges of the GeDSSD in Fig. 5.48. The Image 2 position vs. TKE is given in Fig. 5.49, where the gate on the left was expected to enhance events associate with ^{111}Tc, while the right gate was expected to enhance ^{114}Tc events. Fig. 5.50 shows the clover spectrum for the ^{111}Tc (left) gate. There may be a small number of 563 keV transitions from the decay of ^{114}Tc in this gate. Fig. 5.51 illustrates the TKE

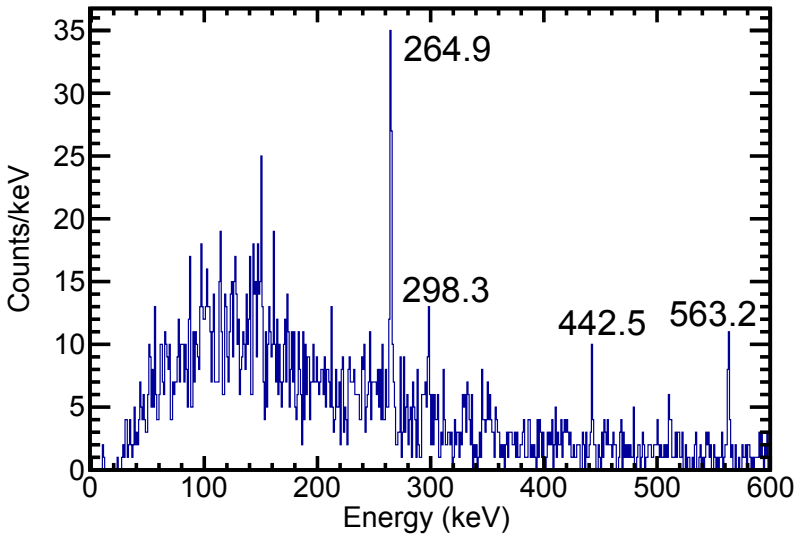

Figure 5.47 β-decay γ-ray spectrum correlated to $^{111/114}$Tc within 250 ms. Several of the ^{114}Tc γ rays are apparent. As reported in Ref. [71], the γ ray energies are at 265.1, 298.0, 443.0, 563.4 keV.

for the heavier ^{114}Tc (right) ion. Several of the β-delayed γ rays were apparent in the spectrum, including the previously known 265-keV, 298-keV, and 443-keV transitions [71]. The 563-keV γ ray was harder to clearly pick out from the background. Table 5.10 summarizes the number of expected counts in the absence of TKE separate compared to the number of observed counts within the observed transitions.

5.4.2.3 $^{112/115}$Tc

A third PID gate to produce β-delayed γ rays associated with the decay of $^{112/115}$Tc was applied to the data. The β-delayed γ-ray spectrum with a correlation time of 500 ms is shown in Fig. 5.52. A γ ray at 236 keV in Fig. 5.52 matched a known γ ray in the H-like ^{112}Tc decay [89], as well as perhaps a γ ray at 511 keV. However, the higher energy transition was not the second most intense transition previously reported. There were too few statistics to perform the TKE separation analysis.

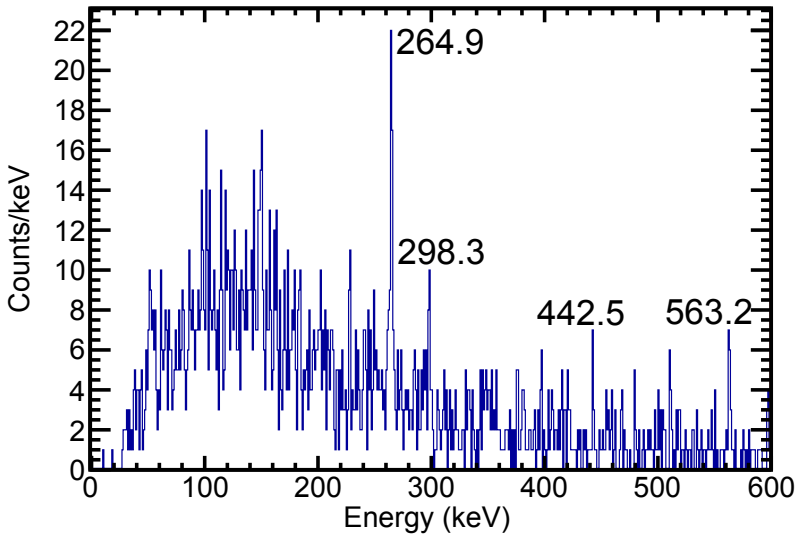

Figure 5.48 β-delayed γ-ray spectrum correlated with $^{111/114}$Tc for events confined to the edge strips of the GeDSSD. Previously measured γ rays are labeled by energy in keV.

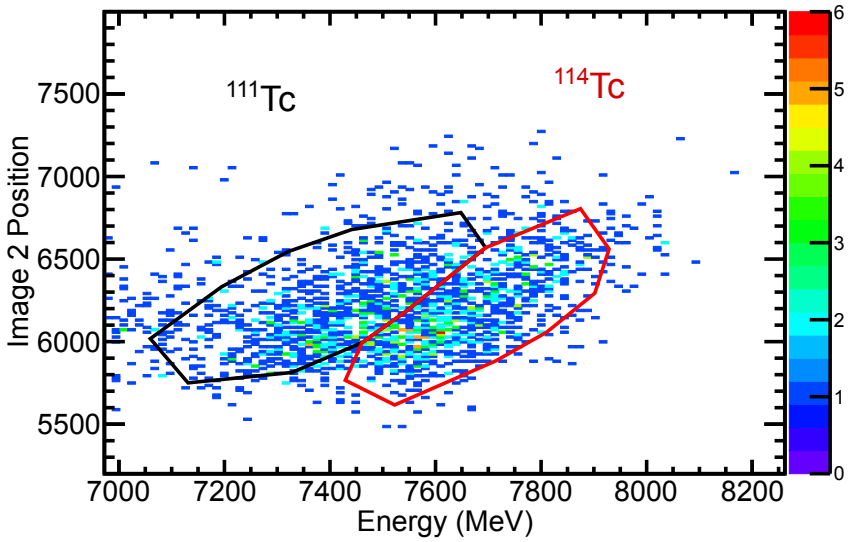

Figure 5.49 Image 2 position vs. the sum of the PIN and GeDSSD energies gates on the $^{111/114}$Tc implants. On the left is ^{111}Tc and on the right is ^{114}Tc.

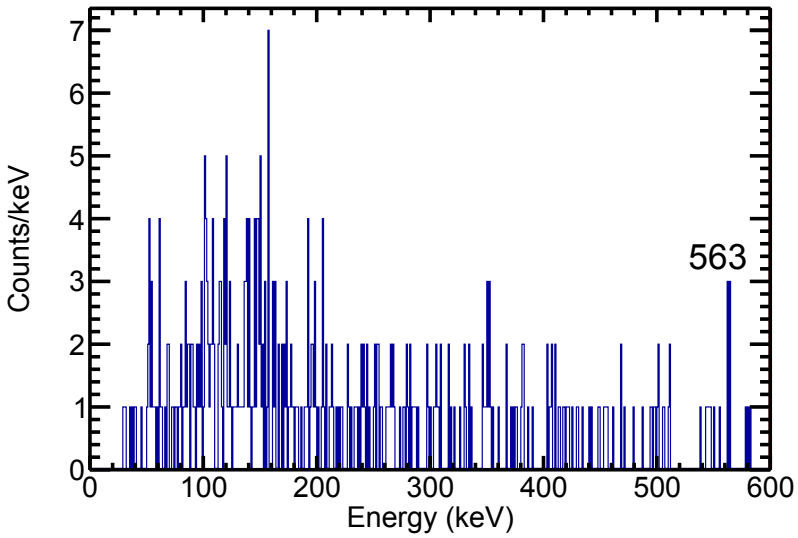

Figure 5.50 β-delayed γ-ray spectrum correlated with $^{111/114}$Tc and confined to the edge strips. An additional requirement on the TKE of the ions expected to enhance the decays of ^{111}Tc was applied to the figure. See text for details.

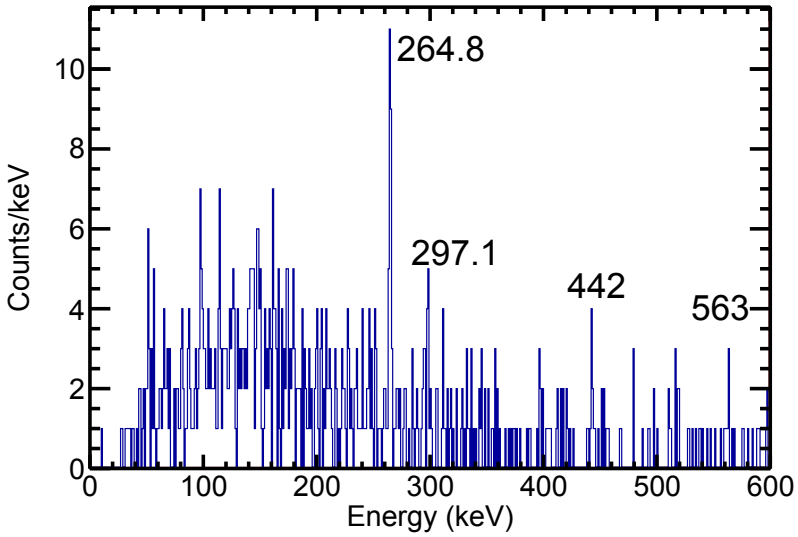

Figure 5.51 β-delayed γ-ray spectrum correlated with $^{111/114}$Tc and confined to the edge strips. An additional requirement on the TKE of the ions expected to enhance the decays of ^{114}Tc was applied to the figure. See text for details.

Table 5.10 Observed counts for transitions in ^{111}Tc and ^{114}Tc decays compared to the expected number of counts if there were no TKE separation. The expected number of counts were determined by scaling the total number of implants for the number within each gate.

Gate	Total in TKE Gate	Number of Observed 265 keV Counts	Scaled 265 keV Counts	Number of Observed 298 keV Counts	Scaled 298 keV Counts
All Edge Events	2016	43±18	-	15±10	-
^{110}Tc (left)	668	0±0	14±6	0±0	5±3
^{113}Tc (right)	880	34±20	19±8	10±4	6±4
Gate	Total in TKE Gate	Number of Observed 443 keV Counts	Scaled 443 keV Counts	Number of Observed 563 keV Counts	Scaled 563 keV Counts
All Edge Events	2016	9±6	-	16±12	-
^{110}Tc (left)	668	0±0	3±2	4±2	5±4
^{113}Tc (right)	880	7±4	4±3	6±3	7±5

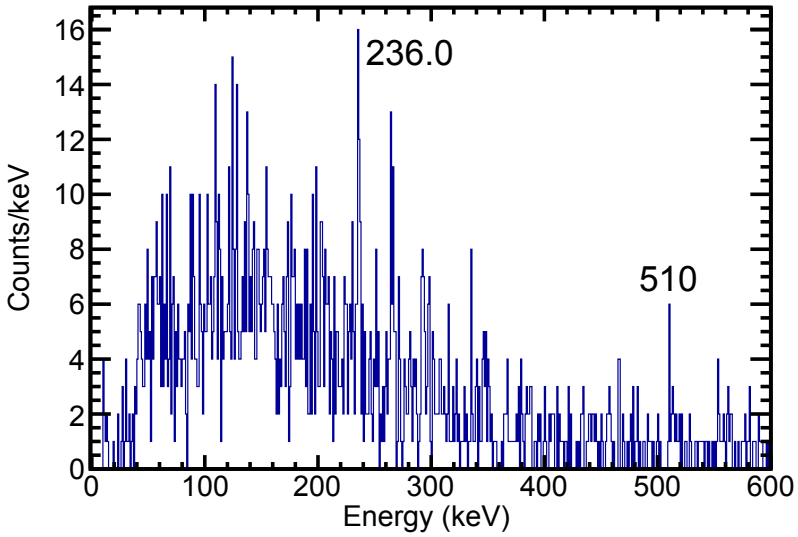

Figure 5.52 β-decay γ-ray spectrum correlated to $^{112/115}$Tc within 500 ms. The 236.8-keV, and possibly a small amount of the 511.5-keV transition in the decay of ^{112}Tc is visible [89].

5.4.2.4 $^{109/112}$Mo

Continuing to the $^{109/112}$Mo, PID group, the 236-keV transition from the decay of the ^{112}Tc daughter, ^{112}Ru, was apparent in Fig. 5.53. The β-delayed γ-ray spectrum in Fig. 5.53 was generated with a correlation time of 500 ms. There were too few counts to perform the TKE separation technique.

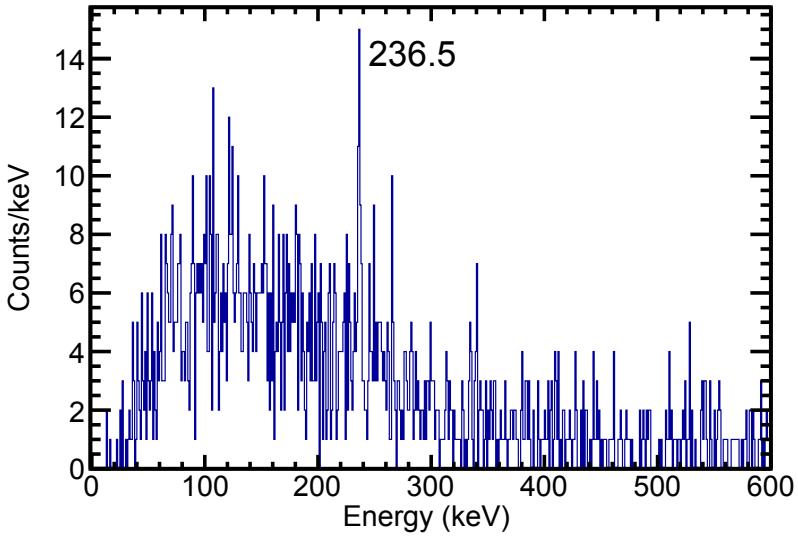

Figure 5.53 β-decay γ-ray spectrum correlated to $^{109/112}$Mo within 500 ms. The 236.8-keV transition in the decay of the daughter ^{112}Tc is visible [89].

5.4.2.5 All other PID gates

Utilizing the γ rays presented thus far, the gates in the PID plot may be unambiguously labeled. With the exception of PID groups containing ^{115}Ru (see Section 5.2), there were no apparent β-delayed γ rays in the other gates. A representative spectrum is shown in Fig. 5.54.

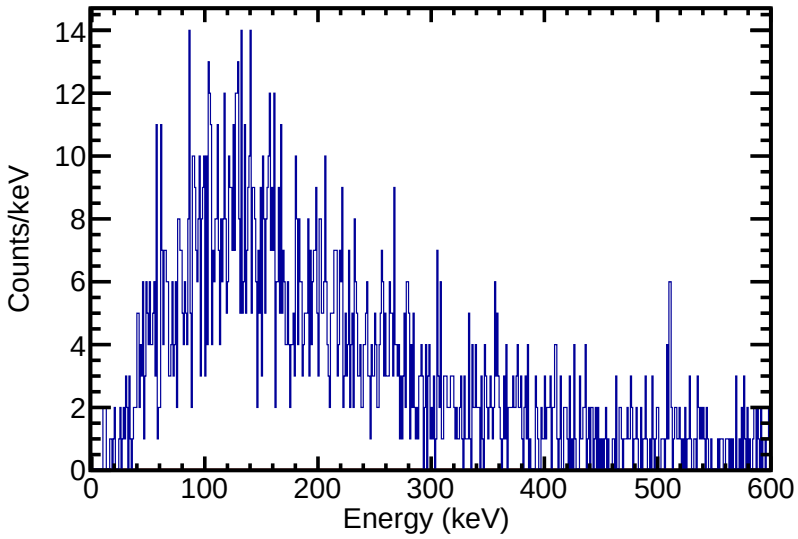

Figure 5.54 β-decay γ-ray spectrum correlated to $^{108/111}$Mo within 500 ms. No β-delayed γ rays are apparent.

CHAPTER 6

CONCLUSIONS AND OUTLOOK

6.1 Conclusions

A variety of different nuclear structure experiments have been successfully carried out utilizing the GeDSSD. The present study focused on the A$\sim$110 neutron rich region of the nuclear chart, in particular on Tc and Ru isotopes. Nuclei with A$\sim$110 have been long thought to exhibit large prolate deformations, with the open question of whether the nuclear shape shifts to a more spherical or an oblate shape at higher A. In addition to ground state spins and parities, isomeric states are an important test of the nuclear structure in the region. In particular, γ-ray and conversion electron spectroscopy are tools that may be used in the discovery and quantification of isomeric states. The GeDSSD discussed within this document is particularly well suited for these studies, as its high detection efficiency for low-energy γ rays and conversion electrons provide a method to quantify internal transitions deexciting isomeric states.

Several isomeric transitions were investigated. In particular, an isomeric state of ^{115}Ru was firmly placed in the ^{115}Ru levels scheme via conversion electron and γ-ray spectroscopy at 123.8 keV with a half-life of 85(13) ms. This isomeric state decayed viz a cascade of two γ rays less than 1 keV apart in energy. Previous results established the presence of a decaying isomer, but did not place the state at an energy. The present work suggests that the multipolarity of the 61.7 keV transition is M1. The transition out of the isomeric state is therefore 62.1 kev in energy, and the previously M2 multipolarity was kept in this work. With the presence of negative parity isomeric states in the heaviest Ru isotopes, the $h_{11/2}$ orbital likely plays a role in their nuclear structure. It is difficult to explain the tentative spins and parities of the ground-states, with prolate configurations, suggesting perhaps a transition to more spherical or even oblate nuclei. In other isotopic chains, previously measured isomeric states in ^{118}Ag at 49 and 155 keV were measured by the double-pulse processing technique, as were previously-measured isomeric states in ^{107}Mo and ^{109}Mo at

67.8 and 71.2 keV respectively.

Several technical and analytical developments were discussed. The GeDSSD was very efficient for both β-decay electrons and β-delayed γ rays. This work characterized the GeDSSD, establishing the expected correlation efficiency, as well as the detectors response to the implantation of heavy ions. While advantageous for detecting a variety of decay modes and low-intensity transitions, the high efficiency for electrons and γ rays led to an increased complexity of analysis due to the possibility of β-γ summing. Thus, the development of an algorithm to re-create the energy deposited on a pixel-by-pixel basis from the strip readout was investigated, and first results were promising. Another technical issue that arose in experiments was the production of multiple charge states of the ions implanted in the detector that created ambiguities within the particle identification. One widespread technique to separate charge states is through a Total Kinetic Energy measurement. After correcting for the effects of charge sharing and cross-talk within the GeDSSD, the total energy of the implanted ions was measured, and used for a TKE measurement. β-delayed γ ray spectra indicate the technique was able to give separation for the outer edges of the GeDSSD.

6.2 Outlook

For future work in the region of A$\sim$110, the next investigation should be the isomeric states of odd-A Ru isotopes. An isomeric state was previously identified in ^{113}Ru, though this state has not been placed at a definitive energy. The excited states known in ^{117}Ru do not have even tentative spin and parity assignments, and it is of interest to investigate whether the pattern of negative parity isomeric states continues into heavier nuclei. Conversion electron spectroscopy performed by detectors like the GeDSSD can help to infer multipolarities and therefore the identification of isomeric states. Finally, data from odd-A nuclei in this region is needed to help in the understanding of the evolution of nuclear structure in the region, and to investigate where the predicted transitions in shape between prolate and either oblate or spherical nuclei occurs in the isotopic chains in the region.

The successful commissioning of the GeDSSD paves the way for the development of future detectors of this type. The experimental advantages of Ge over more traditional Si have been demonstrated, manifesting in increased efficiency and sensitive isomer spectroscopy. There are several changes that would improve the TKE measurement technique. Minimizing non-active material in front of the GeDSSD crystal would result in fewer energy losses, and less energy straggling, making the TKE measurement easier. The amount of material could be reduced by the creation of a similar detector that is connected directly to the vacuum of the beam pipe, eliminating the Kapton window, cryostat, Al radiation shield, and air the beam must pass through. Additionally, the preamplifiers on the back low-gain strips were hound to saturate, preventing an accurate energy determination. Restoring the capability to use two sets of strips for independent energy determination would aid analysis. Another possibility to improve analysis would be to readout energies in pixels rather than in strips, removing the need to reconstruct events from the strip energies. This would, of course, come at the cost of requiring many more DDAS modules and cabling. It was also more difficult to determine the efficiency of the detectors via standardized sources than anticipated. One alternate possibility would be to develop a beam with well-known γ-ray activity and calibrate the efficiency that way, reducing or eliminating the need to rely on simulation. Finally, greater strip segmentation would improve the analysis. Greater segmentation means a more precise location determination, which in turn would allow for higher implantation rates. Greater segmentation would also reduce the effects of β-γ summing, as smaller pixels give the particles greater solid angle in which to separate.

The GeDSSD is a powerful spectroscopic tool, but it is more expensive and is less hardy to radiation damage compared to its Si counterparts. However, the Si detectors do not have the same low-energy γ-ray efficiency. Another option sometimes used in β-decay studies is a segmented plastic scintillator. However, this comes at a cost of the energy resolution. Inorganic scintillators, such as YAP, are sometimes used, though their resolution is comparable to NsI detectors, which is less than that of Ge. One could implant into a $LaBr_3$ detector, but $LaBr_3$ has a large internal activity, which would make correlation more difficult, and no manufacturers are segmenting detectors of

this type. One alternative would be to move to $CeBr_3$, as the $CeBr_3$ detectors have less internal activity compared to $LaBr_3$, although the cost may be prohibitive. In order to replace the GeDSSD for this application, a detector would have to have good energy resolution for both electrons and γ rays, must be able to determine the position of events for correlation, and there must be a low incidence of internal activity.

BIBLIOGRAPHY

BIBLIOGRAPHY

[1] W. Loveland, D. J. Morrissey, and G. T. Seaborg. *Modern Nuclear Chemistry*. John Wiley & Sons, Inc., New Jersey, 2006.

[2] P. Walker and G. Dracoulis. Energy traps in atomic nuclei. *Nature*, 399:35–40, 1999.

[3] W. Urban, A. Złomaniec, G Simpson, J. A. Pinston, J. Kurpeta, T. Rząca-Urban, J. L. Durell, A. G. Smith, B. J. Varley, N. Schulz, and I. Ahmad. New spins for ground states and isomers in ^{115}pd and ^{117}pd. *The European Physical Journal A*, 22:157–161, 2004.

[4] J. Kurpeta, G. Lhersonneau, J. C. Wang, P. Dendooven, A. Honkanen, M. Huhta, M. Oinonen, H. Penttilä, K. Peräjäarvi, J. R. Persson, A. Płochocki, and Äystö J. First decay scheme of ^{113}tc and identification of ^{113}ru^{m}. *The European Physical Journal A*, 2:241–243, 1998.

[5] J. Kurpeta, J. Rissanen, A. Płochocki, W. Urban, V. V. Elomaa, T. Eronen, J. Hakala, A. Jokinen, A. Kankainen, P. Karvonen, T. Małkiewicz, I. D. Moore, H. Penttilä, A. Saastamoinen, G. S. Simpson, C. Weber, and Äystö J. New isomer and decay half-life of ^{115}ru. *Physical Review C*, 82:064318, 2010.

[6] N. Larson, S. N. Liddick, M. Bennett, A. Bowe, A. Chemey, C. Prokop, A. Simon, A. Spyrou, S. Suchyta, S. J. Quinn, S. L. Tabor, Vandana Tai, P. L. Tripathi, and J. M. VonMoss. High efficiency beta-decay spectroscopy using a planar germanium double-sided strip detector. *Nuclear Instrumenta and Methods in Physics Research A*, 727:59–64, 2013.

[7] S. Heyde and J. L. Wood. Shape coexistence in atomic nuclei. *Reviews of Modern Physics*, 83:1467–1521, 2011.

[8] V. R. Pandharipande, R. M. Singru, and R. P. Sharma. Decay of pd^{111} and pd^{111m}. *Physical Review*, 140:1488–1496, 1965.

[9] H. Penttilä, T. Enqvist, P. P. Jauho, A. Jokinen, M. Leino, J. A. Parmonen, and J. Äystö. β-decay of ^{113}rh and the observation of ^{113m}pd: Isomer systematics in odd-a palladium isotopes. *Nuclear Physics A*, 561:416–430, 1993.

[10] W. John, F. W. Guy, and J. J. Wesolowski. Four-parameter measurements of isomeric transitions in ^{252}cf fission fragments. *Physical Review C*, 2:1451–1469, 1970.

[11] W. Urban, T. Rząca-Urban, Ch. Droste, S. G. Rohoziński, J. L. Durell, W. R. Phillips, A. G. Smith, B. J. Varley, N. Schulz, I. Ahmad, and J. A. Pinston. New bands and spin-parity assignments in ^{111}ru. *The European Physical Journal A*, 22:231–239, 2004.

[12] J. Rissanen, J. Kurpeta, A. Płochocki, V. V. Elomaa, T. Eronen, J. Hakala, A. Jokinen, A. Kankainen, P. Karvonen, I. D. Moore, H. Penttilä, S. Rahaman, A Saastamoinen, W. Urban, C. Weber, and J. Äystö. Penning-trap-assisted study of ^{115}ru beta decay. *The European Physical Journal A*, 47:97–105, 2011.

[13] J. Kurpeta, W. Urban, A. Płochocki, J. Rissanen, V. V. Elomaa, T. Eronen, J. Hakala, A. Jokinen, A. Kankainen, P. Karvonen, I. D. Moore, H. Penttilä, A. Saastamoinen, C. Weber, and J. Äystö. Signatures of oblate deformation in the ^{111}tc nucleus. *Physical Review C*, 84:044304, 2011.

[14] P. Möller, J. R. Nix, W. D.. Myers, and W. J. Swiatecki. Nuclear ground-state masses and deformations. *Atomic Data and Nuclear Data Tables*, 59:185–381, 1995.

[15] S. Hilare and M. Girod. Large-scale mean-field calculations from proton to neutron drip lines using d1s gogny force. *The European Physical Journal A*, 33:237–241, 2007.

[16] P. Urkedal, X. Z. Zhang, and I. Hamamoto. Low-lying appreciable gammow-teller strength in deformed neutron-rich nuclei. *Physical Review C*, 64:054304, 2001.

[17] J. Skalski, S. Mitzutori, and W. Nazarewicz. Equilibrium shapes and high-spin properities of the neutron-rich a $\approx$ 100 nuclei. *Nuclear Physics A*, 617:282–315, 1997.

[18] G. A. Lalazissis, S. Raman, and P. Ring. Ground-state properties of even-even nuclei in the relativistic mean-field theory. *Atomic Data and Nuclear Data Tables*, 71:1–40, 1999.

[19] M. R. Oudih, M. Fellah, N. H. Allal, and N. Benhamouda. Systematic study of neutron-rich molybdenum isotopes. *Nuclear Physics A*, 834:479c–481c, 2010.

[20] Y. Aboussir, J. M. Pearson, A. K. Dutta, and F. Tondeur. Nuclear mass formula via an approximation to the hartree-fock method. *Atomic Data and Nuclear Data Tables*, 61:127–176, 1995.

[21] S. Goriely, F. Tondeur, and J. M. Pearson. A hartree-fock nuclear mass table. *Atomic Data and Nuclear Data Tables*, 77:311–381, 2001.

[22] A. Blazkiewicz, V. E. Oberacker, A. S. Umar, and M. Stoitsov. Coordinate space hartree-fock-bogoliubov calculations for the zirconium isotope chain up to the two-neutron drip line. *Physical Review C*, 71:054321, 2005.

[23] Crc handbook of chemistry and physics, 96th edition, 2016.

[24] M. Goeppert Mayer. Om closed shells in nuclei. ii. *Physical Review*, 75:1969–1970, 1949.

[25] F. R. Xu, P. M. Walker, and R. Wyss. Oblate stability of a$\approx$110 nuclei near the r-process path. *Physics Review C*, 65:021303(R), 2002.

[26] W. Urban, T. Rząca-Urban, J. L. Durell, W. R. Phillips, A. G. Smith, B. J. Varley, I. Ahmad, and N. Schulz. First observation of excited states in the ^{110}mo nucelus. *The European Physical Journal A*, 20:381–384, 2004.

[27] H. Hua, C. Y. Wu, A. Cline, A. B. Hayes, R. Teng, R. M. Clark, P. Fallon, A. Goergen, A. O. Macchiavelli, and K. Vetter. Triaxality and the aligned $h_{11\backslash 2}$ neutron orbitals in neutron-rich zr and mo isotopes. *Physical Review C*, 69:014317, 2004.

[28] H. Hua, C. Y. Wu, D. Cline, A. B. Hayes, R. Teng, R. M. Clark, P. Fallon, A. Goergen, A. O. Macchiavelli, and K. Vetter. The sudden onset of the band crossing for the aligned $\pi g_{9/2}$ orbitals: a possible transition of a triaxial shape from prolate to oblate? *Physics Letters B*, 562:201–207, 2003.

[29] C. Y. Wu, H. Hua, D. Cline, A. B. Hayes, R. Teng, D. Riley, R. M. Clark, P. Fallon, A. Goergen, A. O. Macchiavelli, and K. Vetter. Evidence for possible shape transitions in neutron-rich ru isotopes: Spectroscopy of ^{109,110,111,112}ru. *Physical Review C*, 73:034312, 2006.

[30] M. Lian, H. Ohm, B. De Sutter, K. Sistemich, B. Fazekas, and G. Molnár. The deformation of the neutron-rich isotopes ^{102}mo and ^{104}mo. *Zeitschrift für Physik A*, 340:223–224, 1991.

[31] D. Kameda, T. Kubo, T. Ohnishi, K. Kusaka, A. Yoshida, M. Ohtake, N. Fukuda, H. Takeda, K. Tanaka, N. Inabe, Y. Yanagisawa, Y. Gono, H. Watanabe, H. Otsu, H. Baba, T. Ichihara, Y. Yamaguchi, M. Takechi, S. Nishimura, H. Ueno, A. Yoshimi, H. Sakurai, T. Motobayashi, T. Nakao, Y. Mizoi, M. Matsushita, K. Ieki, C. Ishii, H. Yoshii, Y. Miyashita, N. Uematsu, Y. Shirai, T. Sumikama, J. Chiba, E. Ideguchi, A. Saito, T. Yamaguchi, I. Hachiuma, T. Suzuki, T. Moriguchi, A. Ozawa, T. Ohtsubo, M. A. Famiano, H. Geissel, A. S. Nettleton, O. B. Tarasov, D. Bazin, B. M. Sherrill, S. L. Manikonda, and J. A. Nolen. Observation of new microsecond isomers among fission products from in-flight fission of 345 mev/nucleon ^{238}u. *Physical Review C*, 86:054319, 2012.

[32] S. J. Zhu, J. H. Hamilton, A. V. Ramayya, J. K. Hwang, C. Y. Gan, X. Q. Zhang, C. J. Beyer, J. Kormicki, M. Sakhaee, L. M. Yang, L. Y. Zhu, R. Q. Xu, Z. Zhang, Z. Jiang, W. C. Ma, E. F. Jones, P. M. Gore, J. D. Cole, M. W. Drigert, I. Y. Lee, J. O. Rasmussen, T. N. Ginter, Y. X. Luo, S. C. Wu, C. Folden, P. Fallon, P. Zielinski, K. E. Gregorich, A. O. Macchiavelli, S. J. Asztalos, G. M. Ter-Akopian, Yu. Ts. Oganessian, M. A. Stoyer, J. P. Greene, R. V. F. Janssens, and I. Ahmad. Observation of rotational bands in the neutron-rich ^{107}ru nucleus. *Physics Review C*, 65:014307, 2001.

[33] B. Pfeiffer, G. L. Lhersonneau, P. Dendooven, A. Honkanen, M. Huhta, I. Klöckl, M. Oinonen, H. Penttilä, J. R. Persson, K. Keräjärvi, J. C. Wang, K.-L. Kratz, and J. Äystö. β-decay of ^{111}tc to ^{111}ru. *The European Physical Journal A*, 2:17–19, 1998.

[34] J. Kurpeta, W. Urban, Ch. Droste, A. Płochocki, S. G. Rohoziński, T. Rząca-Urban, T. Morek, L. Próchniak, K. Starosta, J. Äystö, H. Penttilä, J. L Durell, A. G. Smith, G. Lhersonneau, and I. Ahmad. Low-spin structure of ^{113}ru and ^{113}rh. *The European Physical Journal A*, 33:307–316, 2007.

[35] J. Stachel, N. Kaffrell, N. Trautmann, K. Brodén, G. Skarnemark, and D. Eriksen. The collective structure of ^{106,108}ru. *Zeitschrift für Physkik A*, 316:105–119, 1984.

[36] G. Mamane, E. Cheifetz, E. Dafni, A. Zemel, and J. B. Wilhelmy. Lifetime measurements of excited levels in prompt fission products of ^{252}cf. *Nuclear Physics A*, 454:213–225, 1986.

[37] L. van Dommelen. Quantum mechanics for engineers. `http://www.eng.fsu.edu/~dommelen/quantum/style_a/index.html`, 2013. Accessed: 9-28-16.

[38] N. B. Gove and M. J. Martin. Log-f tables for beta decay. *Atomic Data and Nuclear Data Tables*, 10:205–219, 1971.

[39] J. B. Kortright. X-ray data bookley. `http://xdb.lbl.gov/Section1/Sec_1-3.html`. Accessed: 12-2-16.

[40] J. M. Blatt and V. F. Weisskopf. *Theoretical Nuclear Physics*. John Wiley & Sons, Inc., New York, 1952.

[41] D. J. Morrissey, B. M. Sherrill, M. Steiner, A. Stolz, and I. Wiedenhoever. Commissioning the a1900 projectile fragment separator. *Nuclear Instruments and Methods in Physics Research B*, 204:90–96, 2003.

[42] J. I. Prisciandaro, A. C. Morton, and P. F. Mantica. Beta counting system for fast fragmentation beams. *Nuclear Instruments and Methods in Physics Research A*, 505:140–143, 2003.

[43] R. Kumar, F. G. Molina, S. Pietri, E. Casarejos, A. Algora, J. Benlliure, P. Doornebal, J. Gerl, M. Gorska, I. Kojouharov, Zs. Podolyák, W. Prokopowicz, P. H. Regan, B. Rubio, H. Schaffner, S. Tashenov, and H. J. Wollersheim. Testing of a dssd detector for the stopped rising project. *Nuclear Instruments and Methods in Physics Research A*, 598:754–758, 2009.

[44] C. B. Hinke, M. Böhmer, P. Boutachkov, T. Faestermann, H. Geissel, J. Gerl, R. Gernhäuser, M. Górska, A. Gottardo, H. Grawe, J. L. Gręboszl, R. Krücken, N. Kurz, Z. Liu, L. Maier, F. Nowacki, S. Pietri, Zs. Podolyák, K. Sieja, K. Steiger, K. Straub, H. Weick, H. J. Wollersheim, P. J. Wood, N. Al-Dahan, N. Alkhomashi, A. Ataç, A. Blazhev, N. F. Braun, T. Čeliković, T. Davinson, I. Dillmann, C. Domingo-Pardo, P. C. Doornenbal, G. de France, G. F. Farrelly, F. Farinon, N. Goel, T. C. Habermann, R. Hoischen, R. Janik, M. Karny, A. Kaşkaş, I. M. Kojouharov, Th. Kröll, Y. Litvinoc, S. Myalski, F. Nebel, S. Nishimura, C. Nociforo, J. Nyber, A. R. Parikh, A. Procházka, P. H. Regan, C. Rigollet, H. Schaffner, C. Scheidenberger, S. Schwertel, P. A. Söderström, S. J. Steer, A. Stolz, and P. Strmeň. Superallowed gamow-teller decay of the doubly magic nucleus ^{100}sn. *Nature*, 486:341–354, 2012.

[45] Yu. Ts. Oganessian, F. Sh. Abdullin, J. Alexander, J. Binder, R. A. Boll, S. N. Dmitriev, J. Ezold, K. Felker, J. M.. Gostic, R. K.. Grzywacz, J. H. Hamilton, R. A. Henderson, M. G. Itkis, K. Miernik, D. Miller, J. K. Moody, A. N. Polyakov, A. V. Ramayya, J. B. Roberto, M. A. Ryabinin, K. P. Rykaczewski, R. N. Sagaidak, D. A. Shaughnessy, Shirokovsky. I. V., M. V. Shumeiko, M. A. Stoyer, N. J. Stoyer, C. G. Subbotin, A. M. Sukhov, Yu. S. Tsyganov, V. K.. Utyonkov, A. A. Voinov, and G. K. Vostokin. Production and decay of the heaviest nuclei ^{293,294}117 and ^{294}118. *Physical Review Letters*, 109:162501, 2012.

[46] F. Rotaru, F. Negoita, S. Grévy, J. Mrazek, S. Lukyanov, F. Nowacki, A. Poves, O. Sorlin, C. Borcea, R. Borcea, A. Buta, N. Cáceres, S. Calinescu, R. Chevrier, Zs. Dombrádi, J. M. Daugas, D. Lebhertz, Y. Penionzhkevich, C. Petrone, D. Sohler, M. Stanoiu, and J. C. Thomas. Unveiling the intruder defomed 0_2^+ state in ^{34}si. *Physical Review Letters*, 109:092503, 2012.

[47] P. A. Ellison, K. E. Gregorich, J. S. Berryman, D. L. Bleuel, R. M. Clark, I. Dragojecić, J. Dvorak, P. Fallon, C. Fineman-Sotomayor, J. M. Gates, O. R. Gothe, I. Y. Lee, W. D. Loveland, J. P. McLaughlin, S. Paschalis, M. Petri, J. Qian, L. Stavsetra, M. Wiedeking, and H. Nitshe. New superheavy element isotopes: 242pu(^{4}8ca,5n)^{2}85114. *Physical Review Letters*, 105:182701, 2010.

[48] T. Sumikama, K. Yoshinaga, H. Wantanabe, S. Nishimura, Y. Miyashita, K. Yamaguchi, K. Sugimoto, J. Chiba, Z. Li, H. Baba, J. S. Berryman, N. Blasi, A. Bracco, F. Camera, P. Doornenbal, S. Go, T. Hasimoto, S. Haykawa, C. Hinke, E. Ideguchi, T. Isobe, Y. Ito, D. G. Jenkinds, Y. Kawada, N. Kobayashi, Y. Kondo, R. Krücken, S. Kubono, G. Lorusso, T. Nakano, M. Kuranta-Nishimura, A. Odahara, H. J. Ong, S. Ota, Zs. Podolyák, H. Sakurai, H. Scheit, K. Steiger, D. Steppenbeck, S. Takano, A. Takashima, K. Tajiri, T. Ternaishi, Y. Wakabayashi, P. M. Walker, O. Wieland, and H. Yamaguchi. Structural evolution in the neutron-rich nuclei ^{106}zr and ^{108}zr. *Physical Review Letters*, 106:202501, 2011.

[49] S. Nishimura. Beta-gamma spectroscopy at ribf. *Progress of Theoretical and Experimental Physics*, 2012:03C006, 2012.

[50] W. F. Mueller, J. A. Church, T. Glasmacher, D. Gutknecht, G. Hackman, P. G. Hansen, K. L. Hu, Z. Miller, and P. Quirin. Thirty-two-fold segmented germanium detectors to identify γ-rays from intermediate-energy exotic beams. *Nuclear Instruments and Methods in Physics Research A*, 466:492–498, 2001.

[51] G. Duchêne, F. A. Beck, P. J. Twin, G. de France, D. Curien, L. Han, M. A. Beausang, C. W. Bentley, P. J. Nolan, and J. Simpson. The clover: a new generation of composite ge detectors. *Nuclear Instrumentation and Methods in Physics Research A*, 432:90–110, 1999.

[52] PhDs Co. Phds gamma ray imaging detectors. `http://www.phdsco.com`. Accessed: 9-28-16.

[53] C. J. Prokop, S. N. Liddick, B. L. Abromeit, A. T. Chemey, N. R. Larson, S. Suchyta, and J. R. Tompkins. Digital data acquisition system implementation at the national superconducting cyclotron laboratory. *Nuclear Instruments and Methods in Physics Research A*, 741:163–168, 2014.

[54] XIA LLC. Dgf pixie-16; 16-channel 100/250/500mhz digital gamma finder in pxi format. `http://www.xia.com/DGF_Pixie-16.html`. Accessed: 5-18-16.

[55] H. Tan, M. Momayezi, A. Fallu-Labruyere, Y. X. Chu, and W. K. Warburton. A fast digital filter algorithm for gamma-ray spectrscopy with double-exponential decaying scintillators. *IEEE Transactions on Nuclear Science*, 51:1541–1545, 2004.

[56] E. L. Hull, E. G. Jackson, C. J. Lister, and R. H. Pehl. Charge-trap correction and radiation damage in orthogonal-strip planar germanium detectors. *Nuclear Instruments and Methods in Physics Research A*, 762:125–129, 2014.

[57] S. Gros, N. J. Hammond, C. J. Lister, P. Chowdhury, S. M. Fischer, and S. J. Freeman. Performance tests of large area position-sensitive planar germanium detectors with conventional

and amorphous contacts. *Nuclear Instruments and Methods in Physics Research A*, 602:467–476, 2009.

[58] M. Sawicka, J. M. Daugas, H. Grawe, S. Ćwiok, D. L. Balabanski, R. Béraud, C. Bingham, C. Borcea, M. La Commara, G. de France, G. Georgiev, M. Górska, R. Grzywacz, M. Hass, M. Hellström, Z. Janas, M. Lewitowicz, H. Mach, I. Matea, G. Neyens, C. O'Leary, F. de Oliveira Santos, R. D. Page, M. Pfützner, Zs. Podolyák, K. Rykaczewski, M. Stanoiu, and J. Żylicz. Isomeric decay of ^{67}fe-evidence for deformation. *The European Physical Journal A*, 16:51–54, 2003.

[59] LISE Group at NSCL/MSU. Exotic beam production with fragment separators. `http://lise.nscl.msu.edu/lise.html`. Accessed: 11-21-16.

[60] L. Mihailescu, K. Vetter, M. Burks, D. Chivers, M. Cunningham, D. Gunter, and K. E. Nelson. Methods for increasing the efficiency of compton imagers. *IEEE Nuclear Science Symposium*, pages URL–CONF–217922, 2006.

[61] E. G. Jackson, E. L. Hull, C. J. Lister, and R. H. Pehl. Ameliorating neutron damage in orthogonal-strip planar germanium detectors. *Nuclear Instruments and Methods in Physics Research A*, 774:34–41, 2015.

[62] D. Weisshaar. Segmented germanium array service level description. `http://www.nscl.msu.edu/_files/documents/sega_sld_2007.pdf`. Accessed: 11-11-16.

[63] I. Reusen, A. Andreyev, J. Andrzejewski, N. Bijnens, S. Franchoo, M. Huyse, Yu. Kudryavtsev, K. Kruglov, W. F. Mueller, A. Piechaczek, R. Raabe, K. Rykaczewski, J. Szerypo, P. Van Duppen, L. Vermeeren, J. Wauters, and Wöhr. β-decay study of ^{54,55}ni produced by an element-selective laser ion source. *Physical Review C*, 59:2416–2421, 1999.

[64] B. Blank. Studies with one- and two-proton drip line nuclei. *The European Physical Journal A*, 15:121–124, 2002.

[65] G. F. Knoll. *Radiation Detection and Measurement*. John Wiley & Sons, Inc., New Jersey, 2010.

[66] D. Pauwels, O. Ivanov, N. Bree, J. Büscher, T. E. Cocolios, M. Huyse, Yu. Kudryavtsev, R. Raabe, M. Sawicka, J. Van de Walle, P. Van Duppen, A. Korgul, I. Stefanescu, A. A. Hecht, N. Hoteling, A. Wöhr, W. B. Walters, R. Broda, B. Fornal, W. Krolas, T. Pawlat, J. Wrzesinski, M. P. Carpenter, R. V. F. Janssens, T. Lauritsen, D. Seweryniak, S. Zhu, J. R. Stone, and X. Wang. Structure of ^{65,67}co studied through the β decay of ^{65,67}fe and a deep-inelastic reaction. *Physical Review C*, 79:044309, 2009.

[67] S. N. Liddick, I. G. Darby, and R. K. Grzywacz. Algorithms for pulse shape analysis using silicon detectors. *Nuclear Instruments and Methods in Physics Research A*, 669:70–78, 2012.

[68] S. Suchyta, S. N. Liddick, Y. Tsunoda, T. Otsuka, M. B. Bennett, A. Chemey, M. Honma, N. Larson, C. J. Prokop, S. J. Quinn, N. Shimizu, A. Simon, A. Spyrou, V. Tripathi, Y. Utsuno, and J. M. VonMoss. Shape coexistence in ^{68}ni. *Physical Review C*, 89:021301(R), 2014.

[69] J. Rissanen, J. Kurpeta, V. V. Elomaa, T. Eronen, J. Hakala, A. Jokinen, A. Kankainen, I. D. Moore, H. Penttilä, A. Płochocki, A Saastamoinen, W. Urban, C. Weber, and J. Äystö. Structure of ^{115}ag studied by β^- decays of ^{115}pd and ^{115}pd^m. *Physical Review C*, 86:034337, 2012.

[70] Youbao Wang, P. Dendooven, J. Huikari, A. Jokinen, V. S. Kolhinen, G. Lhersonneau, A. Nieminen, S. Nummela, H. Penttilä, K. Peräjärvi, S. Rinta-Antila, J. Szerypo, J. C. Wang, and J. Äystö. Beta decay of neutron-rich ^{116}rh and the low-lying level structure of even-even ^{116}pd. *Physical Review C*, 63:024309, 2000.

[71] J. Rissanen, J. Kurpeta, V. V. Elomaa, T. Eronen, J. Hakala, A. Jokinen, I. D. Moore, P. Karvonen, A. Płochocki, L. Próchniak, H. Penttilä, S. Rahaman, A Saastamoinen, J. Szerypo, W. Urban, C. Weber, and J. Äystö. Decay study of ^{114}tc with a penning trap. *Physical Review C*, 83:011301(R), 2011.

[72] A. Jokinen, J. C. Wang, J. Äystö, P. Dendooven, S. Nummela, J. Huikari, V. Kolhinen, A. Nieminen, K. Peräjärvi, and S. Rinta-Antila. Beta decay of neutron-rich ^{118}rh and the lowest excited states in ^{118}pd. *The European Physical Journal A*, 9:9–12, 2000.

[73] WANG You-Bao, P. Dendooven, J. Huikari, A. Jokinen, V. S. Kolhinen, G. Lhersonneau, A. Nieminen, S. Nummela, H. Penttilä, K. Peräjärvi, S. Rinta-Antila, J. Szerypo, J. C. Wang, and J. Äystö. New levels in ^{118}pd observed in the βdecay of very neutron-rich ^{118}rh isotope. *Chinese Physics Letters*, 23:808–811, 2006.

[74] J. Kurpeta, W. Urban, A. Płochocki, J. Rissanen, J. C. Wang, V. V. Elomaa, J. Hakala, A. Jokinen, A. Kankainen, P. Karvonen, I. D. Moore, H. Penttilä, S. Rhaman, A. Sasstamoinen, T. Sonoda, J. Szerypo, C. Weber, and Äystö J. Excited states in ^{115}pd populated in the β^- decay of ^{115}rh. *Physical Review C*, 82:027306, 2010.

[75] C. W. Beausang, C. J. Barton, M. A. Caprio, R. F. Casten, J. R. Cooper, R. Krücken, Benyuan Liu, J. R. Novak, Z. Wang, M. Wilhelm, A. N. Wilson, N. V. Zamfir, and A. Zilges. The yrast ball array. *Nuclear Instrumentation and Methods in Physics Research A*, 452:431–439, 2000.

[76] NIST. X-ray transition energies database. `http://physics.nist.gov/cgi-bin/XrayTrans/search.pl?element=Ru&trans=All&lower=&upper=&units=eV`. Accessed: 12-1-16.

[77] NIST. Tables of x-ray mass attenuation coefficients and mass energy-absorption coefficients from 1 kev to 20 mev for elements z=1 to 92 and 48 additional substances of dosimetric interest. `http://www.nist.gov/pml/data/xraycoef/index.cfm`. Accessed: 8-31-16.

[78] NIST. Stopping-power and range tables for electrons, protons, and helium ions. `http://www.nist.gov/pml/data/star/index.cfm`. Accessed: 8-31-16.

[79] T. Kilbédi, T. W. Burrows, M. B. Trzhaskovskay, P. M. Davidson, and C. W. Nestor Jr. Bricc v2.3s. `http://bricc.anu.edu.au`. Accessed: 9-1-16.

[80] A. L. McCarthy and T. W. Conlon. Energies and half-loves of isomeric transitions in sn^{115} and cd^{109}. *Physical Review*, 147:881–883, 1966.

[81] E. Ivanov, Alevra. A., D. Plostinaru, N. Martalogu, and R. Dumitrescu. An isomeric state of sn^{115} excited by the in^{115} (p,n) reaction. *Nuclear Physics*, 54:177–192, 1964.

[82] G. Audi and A. H. Wapstra. The 1993 atomic mass evaluation. *Nuclear Physics A*, 565:1–65, 1993.

[83] V. Koponen, J. Äystö, J. Honkanen, P. Jauho, H. Penttilä, J. Suhonen, P. Taskinen, K. Rykaczewski, J. Żylicz, and C. N. Davids. Gamow-teller decay of ^{118}pd and of neighbouring even isotopes of palladium. *Zeitschrift für Physkik A*, 333:339–348, 1989.

[84] Z. Janas, J. Äystö, K. Eskola, P. P. Jauho, A. Jokinen, J. Kownacki, M. Leino, J. M. Parmonen, H. Penttilä, J. Szerypo, and J. Żylicz. Gamow-teller decay of ^{118}pd and of the new isotope ^{120}ps. *Nuclear Physics A*, 552:340–352, 1993.

[85] A. Van Poelgeest, J. Bron, W. H. A. Hesselink, K. Allaart, J. J. A. Zalmstra, M. J. Uitzinger, and H. Verheul. Neutron excitations in even mass sn nuclei. *Nuclear Physics A*, 346:70–92, 1980.

[86] J. A. Pinston, W. Urban, Ch. Droste, T. Rząca-Urban, J. Genevey, G. Simpson, J. L. Durell, A. G. Smith, B. J. Varley, and I. Ahmad. Triaxiality in ^{105}mo and ^{107}mo from the low to intermediate spin region. *Physical Review C*, 74:064304, 2006.

[87] H. Penttilä, J. Äystö, K. Eskola, Z. Janas, P. P. Jauho, A. Jokinen, M. E. Leino, J. M. Parmonen, and P. Taskinen. First observation of the beta decay of ^{117}pd and the discovery of a new isotope ^{119}pd. *Zeitschrift für Physik A*, 338:291–294, 1991.

[88] A. Jokinen, J. Äystö, P. P. Jauho, M. Leino, J. M. Parmonen, H. Penttilä, K. Eskola, and Z. Janas. Beta decay of ^{114}ru and q_β systematics for n-rich ru isotopes. *Nuclear Physics A*, 549:420–430, 1992.

[89] J. Äystö, P. P. Jauho, Z. Janas, A. Jokinen, J. M. Parmonen, H. Penttilä, P. Taskinen, R. Béraud, R. Duffait, A. Emsallem, J. Meyer, M. Meyer, N. Redon, M. E. Leino, K. Eskola, and P. Dendooven. Collective structure of the neutron-rich nuclei ^{110}ru and ^{112}ru. *Nuclear Physics A*, 515:365–380, 1990.

[90] J. Kurpeta, G. Lhersonneau, A. Płochocki, J. C. Wang, P. Dendooven, A. Honkanen, M. Huhta, M. Oinonen, H. Penttilä, K. Peräjäarvi, J. R. Persson, and Äystö J. Decay of the neutron-rich isotope ^{113}ru to ^{113}rh. *The European Physical Journal A*, 13:449–460, 2002.